

Investigation of the $pp \rightarrow K^+n\Sigma^+$
reaction at the magnetic spectrometer
ANKE-COSY

Inaugural-Dissertation
zur
Erlangung des Doktorgrades
der Mathematisch-Naturwissenschaftlichen Fakultät
der Universität zu Köln

vorgelegt von
Yury Valdau
aus Sosnowy Bor (Rußland)

Forschungszentrum Jülich

2009

Berichterstatter: Prof. Dr. H. Ströher
Prof. Dr. A. Zilges

Tag der mündlichen Prüfung: 20 Oktober 2009

Contents

1	The physics case	9
1.1	Introduction	9
1.2	Experimental data on K^+ production in pp collisions	11
1.2.1	Inclusive K^+ production data	11
1.2.2	Bubble chamber data	13
1.2.3	The $pp \rightarrow K^+p\Lambda$ reaction	13
1.2.4	The $pp \rightarrow K^+p\Sigma^0$ reaction	17
1.2.5	The $pp \rightarrow K^+n\Sigma^+$ reaction	19
1.2.6	Other hyperon production channels	22
1.3	Theoretical models for the different K^+ production channels	23
1.3.1	Meson exchange model	24
1.3.2	Resonance model	25
2	Experimental setup	27
2.1	The ANKE magnetic spectrometer	27
2.2	Detection systems	30
2.2.1	Positive side detection system	30
2.2.2	Forward detection system	31
2.2.3	Other detection systems not used in analysis	32
2.3	Electronics, online triggers and data acquisition system	33
2.4	Experimental conditions during data taking	34
3	Data analysis	37
3.1	Detector positions	37
3.2	Experimental methods	40
3.2.1	Time of flight	40
3.2.2	Delayed veto technique	42
3.2.3	Vertical angle cut	44
3.2.4	Track selection and neighbouring counter analysis	45
3.2.5	Momentum reconstruction	46
3.2.6	Time calibrations	47

3.3	Particle identification	49
3.3.1	\mathbf{K}^+ identification	49
3.3.2	Identification of protons in the Fd correlated with \mathbf{K}^+	51
3.3.3	Identification of the particle in the Sd correlated with \mathbf{K}^+	54
3.4	Efficiencies	55
3.4.1	Efficiencies of the MWPCs	56
3.4.2	Efficiencies of the range telescopes	56
3.5	Normalisation	58
3.5.1	Proton-proton elastic scattering	59
3.5.2	The Schottky method	60
4	Extraction of the cross sections	63
4.1	Phenomenological models used in the analysis	63
4.2	Inclusive \mathbf{K}^+ spectra	65
4.3	Analysis of the $\mathbf{K}^+\mathbf{p}$ correlation events	69
4.4	Analysis of the $\mathbf{K}^+\pi^+$ correlation events	74
4.5	Extracted total cross sections	77
5	Conclusions	84
6	Outlook	85
A	Summary of measurements at different experimental facilities	87

Zusammenfassung

Die vorliegende Doktorarbeit beschreibt Messungen der $pp \rightarrow K^+n\Sigma^+$ -Reaktion in Schwellennähe. Die Motivation für diese Arbeit liegt im Wesentlichen im Fehlen von Daten zur Σ^+ -Hyperon Produktion in pp Kollisionen und insbesondere in neuen Messungen der $pp \rightarrow K^+n\Sigma^+$ Reaktion durch die COSY11 Kollaboration. In diesem mit einem Neutronendetektor durchgeführten Experiment wurde ein überraschend hoher Σ^+ Wirkungsquerschnitt, der nur schwierig mit Isospin-Überlegungen in Einklang zu bringen ist, gefunden.

Das in dieser Doktorarbeit beschriebene Experiment wurde mit dem ANKE Detektor am COSY bei vier Energien nahe der Schwelle durchgeführt. Es beruht auf der fast untergrundfreien K^+ -Identifikation über den Nachweis verzögerter K^+ -Zerfallsprodukte sowie dem Umstand, dass unterhalb der $pp \rightarrow K^+n\Lambda\pi^+$ Schwelle nur der $\Sigma^+ \rightarrow n\pi^+$ Zerfall zur $K^+\pi^+$ Produktion beiträgt. Deshalb ermöglicht der Nachweis von $K^+\pi^+$ -Paaren eine eindeutige Identifikation der $pp \rightarrow K^+n\Sigma^+$ Reaktion ohne Neutronendetektor.

Die Analyse von drei simultan gemessenen Spektren wurde durchgeführt, um nach Hinweisen auf einen möglicherweise hohen Σ^+ - Wirkungsquerschnitt zu suchen. Alle bei den Experimentenergien erlaubten K^+ -Produktionskanäle tragen zu inklusiven K^+ - sowie K^+p -Korrelationspektren bei. In den inklusiven K^+ - Verteilungen sind die Beiträge der verschiedenen Produktionskanäle aufsummiert und können nur durch theoretische Modelle unterschieden werden. In den K^+p -Korrelationspektren werden nicht nur Signale von primär erzeugte Protonen, sondern auch durch Protonen aus Hyperonzerfällen verzeichnet. Demnach tragen Ereignisse aus $\Sigma^+ \rightarrow p\pi^0$ Zerfällen zur fehlenden K^+p Masse bei. Die $K^+\pi^+$ -Korrelationen lassen die Identifikation der Σ^+ Reaktionskanäle und eine Abschätzung des totalen Wirkungsquerschnittes zu. Diese Methode wurde erfolgreich auf existierende ANKE-Daten von August 2003 angewendet und führte zu einer Publikation in einem referierten Journal. Die Analyse der experimentellen Daten von September 2007 führt zu folgenden Ergebnissen:

- Die totalen $pp \rightarrow K^+n\Sigma^+$ Wirkungsquerschnitte sind bei den vier Experimentenergien um zwei Größenordnungen kleiner als die durch COSY11 veröffentlichten.
- Die totalen Λ - und Σ^0 -Wirkungsquerschnitte wurden aus K^+p invariantfehlender-Masse Spektren extrahiert und sind im Einklang mit dem Weltdatensatz, wenn man von dem Datenpunkt für Σ^0 bei niedrigster Energie absieht, der mit technischen Problemen behaftet ist.
- Der inklusive doppelt differentielle Wirkungsquerschnitt wurde aus K^+ -Daten extrahiert und wird durch ein verbessertes Model, welches die totalen Wirkungsquerschnitte aus K^+p - und $K^+\pi^+$ - Analysen berücksichtigt, beschrieben.

Die in dieser Doktorarbeit dargestellten neuen experimentellen Ergebnisse vervollständigen und verbessern die Datenbasis im Bereich der Produktion von leichten Hyperonen und erlauben so die Überprüfung weiterer theoretischer Modelle. Der natürliche nächste Schritt wäre eine Ausweitung dieser Studien auf differentielle Observablen.

Abstract

This thesis describes measurements of the $pp \rightarrow K^+n\Sigma^+$ reaction near threshold. The work was largely motivated by the lack of data for Σ^+ hyperon production in pp collisions and, in particular, by recent measurements of $pp \rightarrow K^+n\Sigma^+$ by the COSY11 collaboration. The experiment performed by this group using a neutron detector reported surprisingly high Σ^+ cross sections that are hard to reconcile with isospin considerations.

The experiment discussed in the thesis has been performed at the ANKE-COSY facility at four close-to-threshold energies. It relies on the almost background-free K^+ identification using the delayed-veto technique and the fact that below the threshold for $pp \rightarrow K^+n\Lambda\pi^+$ there is no source of the $K^+\pi^+$ correlations other than the $\Sigma^+ \rightarrow n\pi^+$ decay. Thus, the detection of $K^+\pi^+$ pairs allows one to identify the $pp \rightarrow K^+n\Sigma^+$ reaction without the need for a neutron detector.

The analysis of three simultaneously measured spectra has been carried out, searching for any signal from a possible high Σ^+ cross section. All the K^+ production channels allowed at the energy of the experiment contribute to the K^+ inclusive and K^+p correlation spectra. In the K^+ inclusive distributions, signals from the different production channels are summed and can only be isolated using theoretical models. In the K^+p correlation spectra, there are not only signals from the direct reaction protons but also protons from hyperon decays can be observed. Thus, the signal from $\Sigma^+ \rightarrow p\pi^0$ decay contributes to the K^+p missing mass. The study of the $K^+\pi^+$ correlations allows one to identify the Σ^+ reaction channels and to estimate the total production cross section. This method has been successfully applied to existing ANKE data collected in August 2003 and resulted in a publication in a refereed journal. Analysis of experimental data collected in September 2007 yielded following results:

- The $pp \rightarrow K^+n\Sigma^+$ total cross sections measured at four energies are two orders of magnitude smaller than those reported by COSY11.

- The Λ and Σ^0 total cross sections extracted from K^+p missing mass spectra are found to be in agreement with the world data, except for lowest energy data point for Σ^0 , where there were technical problems.
- The inclusive double differential cross sections extracted from the K^+ data are described by a refined model that uses total cross sections as obtained from the K^+p and $K^+\pi^+$ analyses.

The new experimental results presented in the thesis complete and significantly improve the database for light hyperon production, thus allowing one to test further theoretical models. The natural next step would be to extend these studies towards differential observables.

Chapter 1

The physics case

Several times in the evolution of physics people have believed that the smallest building blocks of nature have been discovered. Nowadays it is accepted that these building blocks are the quarks (q) that are confined in the mesons ($q\bar{q}$) and baryons (qqq) and that interact between each other through the exchange of gluons (g). The gluons are field bosons in the Quantum Chromo Dynamics (QCD), the theory of strong interactions. Within the framework of QCD the quarks have spin-half (fermions) and carry colour charge (“red”, “green” and “blue”) whereas the gluons have integer spins. Currently it is believed that there are six types of quarks with non-integral values of electric charge ($2/3$ for u, c and t and $-1/3$ for the d, s and b) and that these form the basis of all the types of particle. The presence of the s , c , t or b quark in the particle define the flavour quantum number.

In a framework of standard model, the proton and neutron, which are the elements of nature that we see around us, consist of two combinations of u and d quarks (proton = uud , neutron = udd). Thus, the production of particles with additional types of quark (strange quark s for example) in the final state particles may shed light on the structure of the nucleons and the dynamics of the strong interactions.

Strangeness production in proton-proton collisions is the subject of the present thesis.

1.1 Introduction

Since the first observation of K mesons in a Wilson cloud chamber in 1944 [1], strange particles have attracted significant attention of the particle physics community. The first investigations of all varieties of strange particles, called V particles due to their characteristic trace in the cloud chamber,

have been carried out using cosmic rays [3]. Due to their relatively small production cross sections, even under excellent experimental conditions the accumulation of information about any type of the strange particles took a lot of time.

Even before studies with particle accelerators had become available, the strangeness quantum number was introduced by Gell-Mann and Nishijima [2] in 1955 for the classification of a variety of particles known at that time. The basic principles of particle classification used up to now were then already developed. More detailed investigations of strangeness production became possible only after the development of more powerful accelerators.

Strangeness is a quark flavor which is produced, either from the vacuum, or from the quark-antiquark sea in the nucleons. The studies of strangeness production therefore deepen our understanding of the internal structure of the baryons. The easiest way to produce an $s\bar{s}$ pair via an NN collision is the $NN \rightarrow K^+N\Lambda$ reaction, which has a threshold at a proton beam energy of $T_p = 1.58$ GeV. The $K^+N\Lambda$ final state is also interesting due to the presence of the two baryons N and Λ , the interaction of which can be studied to test the validity of the $SU(3)$ flavour symmetry [4]. Furthermore, there are indications that excited states of the nucleons, for example the $S_{11}(1650)$, which later decay to the hyperon and kaon [5,6], have a significant influence on strangeness production.

Strangeness is conserved in the strong interaction and, since there are no baryons with positive strangeness, the low energy K^+ -nucleon total cross section is small. As a consequence, K^+ mesons produced in the interaction have long mean free paths in the nuclear matter. Thus, studies of subthreshold strangeness production ($T_N < 1.58$ GeV) in pA [7] and AA [8] interaction are of special interest. In such cases kaons, which originate from the high density phase of the reaction, are not absorbed. This means that K^+ mesons produced in pA or AA interactions can carry information about the production mechanism, high energy components of the nuclear wave function, and possible cooperative phenomena in the nucleus.

A significant database on strangeness production in pp , pA and AA interactions now exists. Inclusive K^+ production in pA interactions has been extensively studied at CELSIUS [9], SATURNE [10], and ANKE [11] under different kinematical conditions. The ANKE $pA \rightarrow K^+X$ programme has led to the accumulation of a large amount of experimental data on kaon production on different targets and a determination of the strength of the K^+N potential [11]. The analysis of K^+d correlation data shows the first evidence for a cluster production mechanism at subthreshold energies [12].

The production of K^+ , K^- and K^0 mesons in AA -collisions has been studied by KaoS [13] and FOPI [14] at GSI (Darmstadt). In these experiments

kaons are used as a probe of the high density nuclear matter produced in AA collision. It was found that the K^+/K^- ratio is enhanced in heavy-ion collisions as compared to pp collisions [13]. This, and many other experimental results obtained with different beams and targets, have significantly improved our knowledge of the mechanisms of strangeness production and the understanding of matter in different phases.

This thesis presents an investigation of associated strangeness production in proton-proton collisions close to threshold. In Chapter 1.2 existing experimental data and theoretical models for the K^+ production in pp interactions are discussed. In Chapter 2 the COoler-SYnchrotron COSY and the ANKE magnetic spectrometer are described. The experimental techniques and analysis procedures used to obtain the experimental results are explained in Chapter 3. The procedure for extracting total cross sections and additional observables are presented in the Chapter 4. The Conclusions and Outlook are given in Chapters 5 and 6, respectively.

1.2 Experimental data on K^+ production in pp collisions

The total cross section for K^+ production in pp collisions is relatively low, which puts significant requirements onto the quality of the proton beam. The main investigations of the different K^+ production reaction channels have therefore been carried out at modern accelerators, such as SATURNE [15] and COSY [16]. In the close-to-threshold regime ($T_{\text{thr}} = 1.58$ GeV) there are three main K^+ production channels, *viz.* $pp \rightarrow K^+p\Lambda$, $pp \rightarrow K^+p\Sigma^0$, and $pp \rightarrow K^+n\Sigma^+$. The available experimental data on these three channels are discussed in Sec. 1.2.3, 1.2.4, and 1.2.5, respectively. The data on the heavy hyperon channels and four body final states with an additional π show even smaller total cross sections than those of the three body final states with light hyperons [17]. Nevertheless, one of the measurements presented in this thesis was performed slightly above the threshold for $\Lambda\pi$ production, and therefore some details of the four body final states are presented in Sec. 1.2.6.

1.2.1 Inclusive K^+ production data

A number of experiments has been performed that measured inclusive K^+ momentum spectra [18,19,20,15]. The experimental distributions for inclusive data of course contain contributions from all the strangeness production channels that are allowed at that particular energy. The most accurate measurements of the K^+ inclusive spectra were undertaken at the magnetic

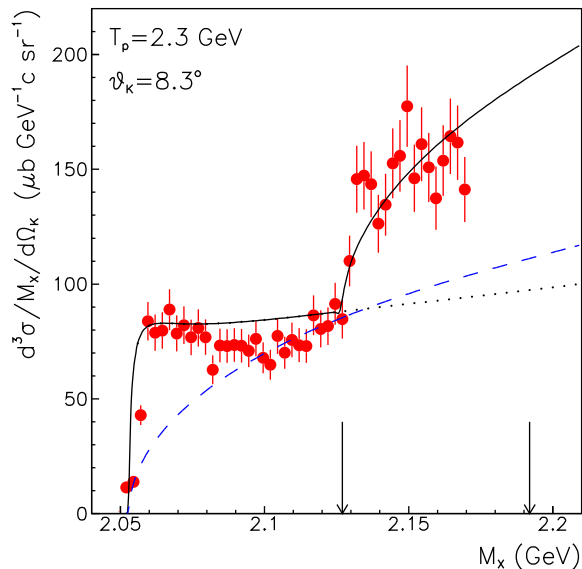


Figure 1.1: The K^+ missing mass spectra measured at 2.3 GeV [15] compared to simulations from Ref. [22]. The K^+ were measured at an emission angle of 8.3° . The figure is taken from Ref. [22].

spectrometer SPES 4 at SATURNE, Saclay [15]. High resolution K^+ momentum spectra studies were performed at 2.3 and 2.7 GeV at several K^+ detection angles in order to investigate the $p\Lambda$ final state interaction (FSI) and search for a strange exotic dibaryon ($S = -1$). Although the exotic dibaryon was not found, the K^+ missing mass spectra led to estimates of the scattering length and effective range parameter of the $p\Lambda$ system [21].

In Ref. [22], the authors performed an analysis of all the available K^+ inclusive momentum spectra, trying to isolate the contributions of the individual hyperons by using the K^+ missing mass spectra. Any K^+ momentum spectrum measured at some fixed laboratory angle can be converted into a missing mass spectrum using the corresponding Jacobian. The thresholds of individual channels can be identified in the missing mass spectra, allowing one to investigate threshold effects. Thus, by analysing measured missing mass spectra on the basis of simple phase space simulations, with the inclusion of a $p\Lambda$ final state interaction in the $K^+p\Lambda$ channel, it was possible to estimate the total cross sections of individual final states contributing to the spectra. However, the inherent uncertainty in such an analysis is relatively large, since the K^+ missing mass spectra are integrated over a very small region of phase space. In addition, the total cross sections of the Σ^+ and

Σ^0 production are superimposed on the much bigger contribution from the $pp \rightarrow K^+p\Lambda$ reaction. This makes the extraction of Σ cross sections very dependent on the models used for the $pp \rightarrow pK^+\Lambda$ reaction. It is therefore hard to draw very firm conclusions about Σ production from such data. A comparison of the simulations with the inclusive K^+ spectra measured at 2.3 GeV is presented in Fig. 1.1.

1.2.2 Bubble chamber data

The bubble chamber experiments that were done at relatively high energies and suffer from low statistics and poor resolution [5, 23]. In most of the measurements only the total cross sections of the well identified three and four body reaction channels have been estimated. A compilation of the total cross sections for the different reaction channels, measured at relatively high energies with bubble chambers, is presented in Ref. [23]. However, some differential observables with low statistics have also been published at relatively high energy (5.13 GeV) [5]. The deviation of the measured differential mass spectra for $pp \rightarrow K^+p\Lambda$ and $pp \rightarrow K^+p\Sigma^0$ from pure phase space was interpreted as indications for strong final state interactions and the significant influence of resonances in the production mechanism.

More detailed investigations of the three lightest hyperon production channels have been carried out using counter techniques at the COSY storage ring.

1.2.3 The $pp \rightarrow K^+p\Lambda$ reaction

The $pp \rightarrow K^+p\Lambda$ reaction is the most investigated of all the different K^+ production channels. Before COSY began operation, only one data point from a bubble chamber experiment was available in the threshold region [24]. The COSY11 [25, 16, 26] and COSY-TOF [27, 6] collaborations performed series of measurements of the total cross section for Λ production at different energies. COSY11 measured close to threshold by reconstructing the Λ in the K^+p missing mass distribution, whereas COSY-TOF performed exclusive measurements of the reaction channel, registering all the particles in the final state. The dependence of the total cross section on the excess energy ε is presented in Fig. 1.2.

The analysis of the available experimental data on the $pp \rightarrow K^+p\Lambda$ reaction using a simple phase space model indicates the presence of a strong $p\Lambda$ final state interaction [29]. The parameters of the $p\Lambda$ final state interaction (FSI) are, however, poorly known [21] due to the absence of high quality $p\Lambda$ scattering data. Values of the singlet (a_s) and triplet (a_t) scattering lengths

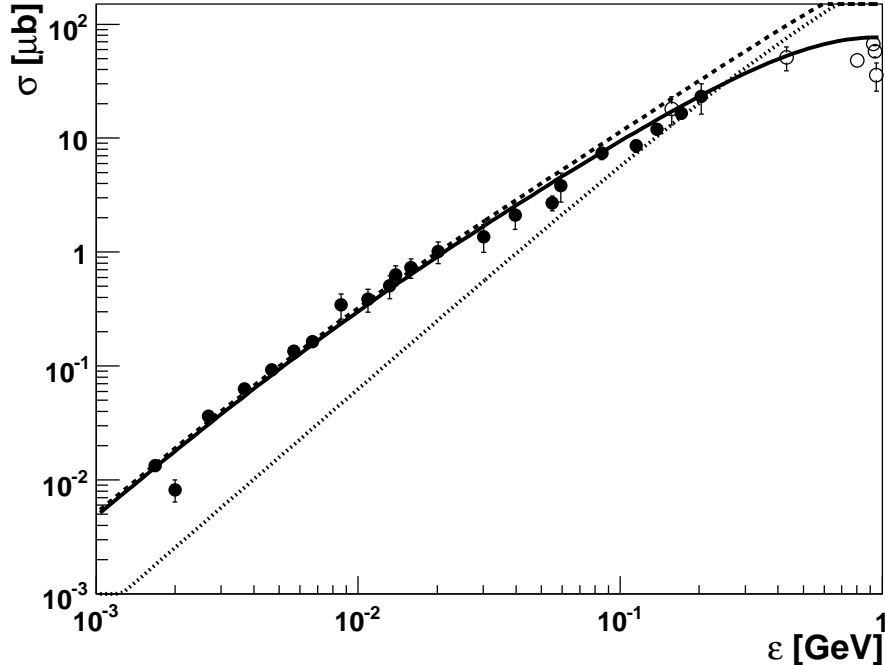


Figure 1.2: The total cross sections of the $pp \rightarrow K^+p\Lambda$ reaction as a function of excess energy. Measurements performed at COSY are shown by closed circles [25, 16, 26, 27, 6, 28]; open circles represent results from other experimental facilities [24, 23]. The parametrisation of the three body $K^+p\Lambda$ phase space with a constant matrix element is shown by the dotted line, the same dependence after correction for the $p\Lambda$ FSI by the dashed line. The three body phase space corrected for the final state interaction and matrix element energy dependence is shown by the solid line [29].

have been determined using the 378 Λp scattering events reported in Ref. [30], leading to the following parameters:

$$a_s = -1.8 \left\{ \begin{array}{l} +2.3 \\ -4.2 \end{array} \right. \text{ fm and } a_t = -1.6 \left\{ \begin{array}{l} +1.1 \\ -0.8 \end{array} \right. \text{ fm.} \quad (1.1)$$

The corresponding effective range parameters vary from 0 to 16 fm. This shows that the parameters of the $p\Lambda$ FSI are not accurately determined by the experimental data and can vary in different analyses.

The authors of Ref. [29] proposed to parameterise the energy dependence of the total cross section in terms of pure three-body phase space with a constant matrix element and strong final state interaction implemented using the

Jost function. In their later analysis [31] this parametrisation was improved by using an energy dependent matrix element. The results of these parametrisations are compared with the experimental data in Fig. 1.2. Using this parametrisation the Λ total production cross section can be determined with a precision of $\sim 10\%$ for excess energies up to 1 GeV.

Very little is known up to now about the production mechanism and most of differential observables have only been presented in terms of PhD theses; for details see Appendix A. Dalitz plots and their corresponding projections measured at 2.75 and 2.85 GeV at COSY-TOF are presented in Refs. [27, 6]. The analysis of Dalitz plots performed in Ref. [6] and continued in Ref. [32] leads to the conclusion that the production of the $K^+p\Lambda$ final state proceeds via different N^* resonances ($N(1650)$, $N(1710)$ and $N(1720)$). Furthermore, it was found in Ref. [32] that the contributions of the different resonances to the production mechanism changes with beam momentum. On the basis of the Dalitz plot analysis it was concluded [6] that close-to-threshold Λ production take place via π exchange and that the $p\Lambda$ final state interaction has a significant influence on all the observed distributions [6]. In Ref. [32] it is suggested that up to the excess energy of 282 MeV the contribution of the higher partial waves is very small, though the measured angular spectra show some anisotropy for all three final particles. The parameters of the partial wave analysis of angular distributions measured by COSY-TOF are collected in Appendix. A.

There is very little information on polarisation observables for the $pp \rightarrow K^+p\Lambda$ reaction in the close-to-threshold regime. From high energy experiments it is known that

- the Λ produced are polarised perpendicular to the production plane and that the polarisation is negative;
- the polarisation increases linearly with the transverse momentum p_T of the Λ hyperon;
- the Λ polarisation is almost independent of the proton beam momentum from 12 to 200 GeV/ c .

The Λ polarisation at 2.75 GeV/ c has been measured as a function of the momentum transfer [27]. In addition there are more measurements of the Λ polarisation performed with the COSY-TOF detector that have been reported in PhD theses [33, 34, 35, 36, 37, 38]. The effect of Λ polarisation is still not explained by theoretical models.

There is only one measurement of the D_{NN} parameter using polarised proton beams of 3.67 and 2.94 GeV/ c performed by the DISTO collaboration [39, 40]. The result of the measurements at 3.67 GeV/ c as a function of

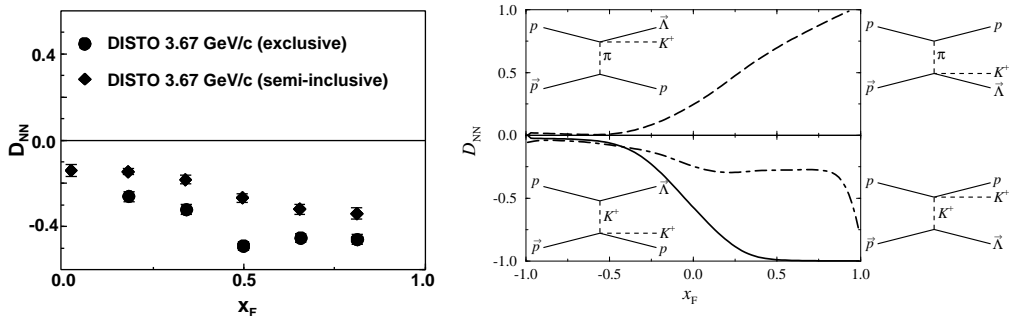


Figure 1.3: Left panel: Values of the polarisation transfer parameter D_{NN} as a function of Feynman x_F measured for the $\bar{p}p \rightarrow K^+ p \bar{\Lambda}$ reaction at 3.67 GeV/c [39]. Results for the exclusive and semi-inclusive analysis discussed in Ref. [39] are presented by circles and diamonds, respectively. Right panel: Theoretical calculations of D_{NN} for the various exclusive Λ production mechanisms. The Feynman diagrams indicate the dominant exchange contribution for the positive versus negative x_F . The D_{NN} calculated with only π exchange is shown by the dashed line, K exchange solid line, combination of both together with the Λp FSI dash-dotted. The figures are from Ref. [39].

the Feynman variable x_F ($x_F = p_{z\Lambda}^*/p_{max\Lambda}^*$ is a Λ longitudinal momenta as a fraction of maximally allowed value) is presented in Fig. 1.3. The sensitivity of D_{NN} to the production mechanism is illustrated in Fig. [39], where the calculations of Ref. [41] are shown. Large and positive values of D_{NN} for $x_F > 0$ would indicate the dominance of π exchange, while negative values would be attributed to the dominance of K^+ exchange. The negative values of D_{NN} measured at two energies by the DISTO collaboration clearly suggest that K^+ exchange is the most important production mechanism for the $pp \rightarrow K^+ p \Lambda$ reaction [39]. This result is, however, in contradiction to the conclusion based on the analysis of the Dalitz plots measured by the COSY-TOF collaboration [6]. Furthermore, measurements of the D_{NN} parameter have been performed at 2.75 and 2.95 GeV/c with the COSY-TOF detector and reported in a PhD thesis [42]. The observed value of D_{NN} is consistent with zero for the full range of x_F , which would be consistent with a dominance of π exchange in the production mechanism.

The $pp \rightarrow K^+ p \Lambda$ reaction has been intensively studied. The total production cross section is known with an accuracy of 10% for excess energies up to 1 GeV. The strength of the $p\Lambda$ final state interaction can be estimated using unpolarised data on the total cross sections and measured K^+ missing

mass spectra. However, additional measurements with polarised beam are needed in order to separate the singlet and triplet components of the FSI. The production mechanism is still not understood; two independent measurements of the D_{NN} parameter contradict each other, and no firm conclusions about dominant exchange mechanism can be drawn. Most of the differential observables, shown in various COSY-TOF PhD theses, deviate from a phase space behaviour.

1.2.4 The $pp \rightarrow K^+ p \Sigma^0$ reaction

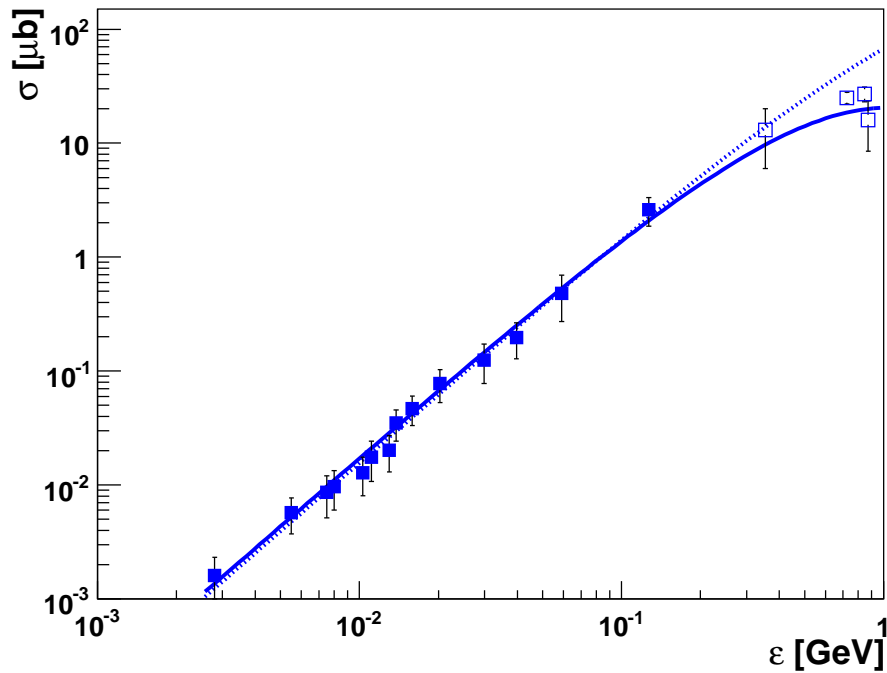


Figure 1.4: Energy dependence of the $pp \rightarrow K^+ p \Sigma^0$ total cross section as a function of excess energy. Measurements performed at COSY are shown by the closed squares [16, 26, 28] while the open squares were obtained at other experimental facilities [24, 23]. The parametrisation of the three body $K^+ p \Sigma^0$ phase space with the constant matrix element is shown by the dotted line; the model corrected for the energy dependent matrix element is shown by the solid line [29].

The second K^+ production channel in the threshold region is the $pp \rightarrow$

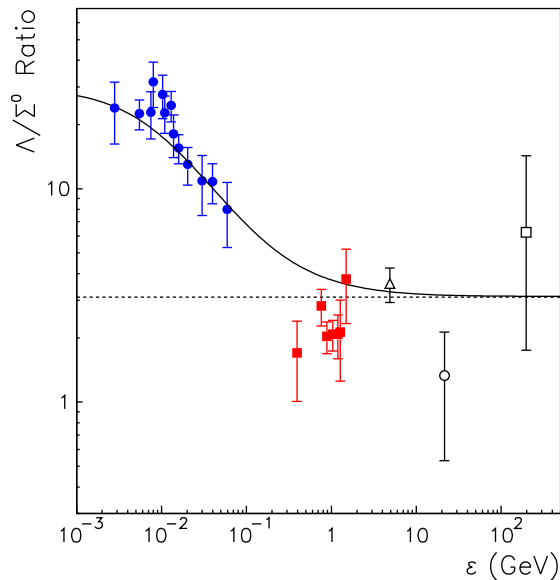


Figure 1.5: The ratio $R(\Lambda/\Sigma^0)$ as a function of excess energy in comparison with the ratio of parameterisations for the corresponding channels from Ref. [31]. The figures is taken from Ref. [31].

$K^+p\Sigma^0$ reaction. This also can be identified directly using K^+p correlations. The energy dependence of the total cross section of Σ^0 production was investigated in COSY energy range in Refs. [26, 16, 28]. An analysis of the experimental data performed in Ref. [31] and shown in Fig. 1.4 suggests that the energy dependence follows a simple phase space approximation with a slowly varying matrix element. There is no indication for any significant final state interaction. There are, in addition, several data points measured with the COSY-TOF spectrometer and presented in PhD theses [27, 33, 35]. Although these generally agree with the common trend, they are not shown in Fig. 1.4 but are given in Table A.11.

There are no data on differential observables for the Σ^0 reaction channel available in the COSY energy range. However, data collected with a bubble chamber at 5.13 GeV indicate the influence of resonances, but no firm conclusion about any $p\Sigma^0$ FSI was made [5].

The ratio $R(\Lambda/\Sigma^0)$ of the Λ and Σ^0 production cross section in the close-to-threshold region was investigated by the COSY11 collaboration [26, 16]. Rather surprisingly it was found that close to threshold this ratio is as large as 28 [16] while at higher energies it is about 3 [23]. This strong variation of the ratio was investigated within several theoretical models [43, 44, 45].

Assuming that Λ and Σ^0 hyperons are produced solely via K exchange, and ignoring final state interactions, the ratio of the total cross sections $\sigma_\Lambda/\sigma_{\Sigma^0}$ is proportional to the ratio of coupling constants $g_{KN\Lambda}^2/g_{KN\Sigma^0}^2$ [44]. Although values of $g_{KN\Lambda}$ and $g_{KN\Sigma^0}$ are not known precisely, the SU(6)-symmetry predicts this ratio to be 27. This number is in fair agreement with the experimental observation [16]. On the other hand, all the models stress the importance of $p\Lambda$ FSI [44, 46] and require π exchange for the description of the experimental data [6]. In contrast, experimental data from DISTO collected with a polarised proton beam [39] support the dominance of the K exchange for the $pp \rightarrow K^+p\Lambda$ production mechanism.

The phenomenological analysis of the Λ/Σ^0 ratio presented in Ref. [31] is able to describe simultaneously the ratio of total cross sections and the energy dependence of the total cross sections. This analysis uses three-body phase space for Λ and Σ^0 hyperons with slowly varying matrix elements and a strong Λp FSI for the description of the ratio. The quality of the description is shown in Fig. 1.5.

1.2.5 The $pp \rightarrow K^+n\Sigma^+$ reaction

Experimental data on the only charged hyperon production channel $pp \rightarrow K^+n\Sigma^+$ are scarce. Due to the presence of the neutron in the final state, identification of the Σ^+ hyperon via a missing mass is only possible if the neutron is detected in coincidence with the K^+ . However, there is a possibility to identify the $K^+n\Sigma^+$ final state using $K^+\pi^+$ coincidences because, below the threshold for $pp \rightarrow K^+n\Lambda\pi^+$, there is no source of $K^+\pi^+$ correlations other than $pp \rightarrow K^+n\Sigma^+$, where the $\Sigma^+ \rightarrow n\pi^+$ decay has a branching ratio (BR) of 48.3% [47]. This method, which relies on the excellent K^+ identification using the delayed veto technique, has been developed for Σ^+ identification at ANKE [28].

The first published measurements of the Σ^+ hyperon production cross section close to threshold were performed by the COSY11 collaboration using a neutron detector [48]. The authors reported extraordinarily high Σ^+ production cross sections at excess energies of 13 and 60 MeV, *i.e.*, $T_p = 1.826$ and 1.958 GeV, respectively, that were almost as high as those for Λ production at these two beam energies [48].

The COSY11 measurements initiated a study of ANKE data to try to find evidence for their surprisingly high Σ^+ production cross sections. A simultaneous analysis of three spectra measured at 2.16 GeV was undertaken [28]. The signal from the Σ^+ hyperon channel was searched in the K^+ inclusive spectra, the K^+p missing mass spectra, and the $K^+\pi^+$ correlation spectra. In the K^+ inclusive double differential cross section, the signal from

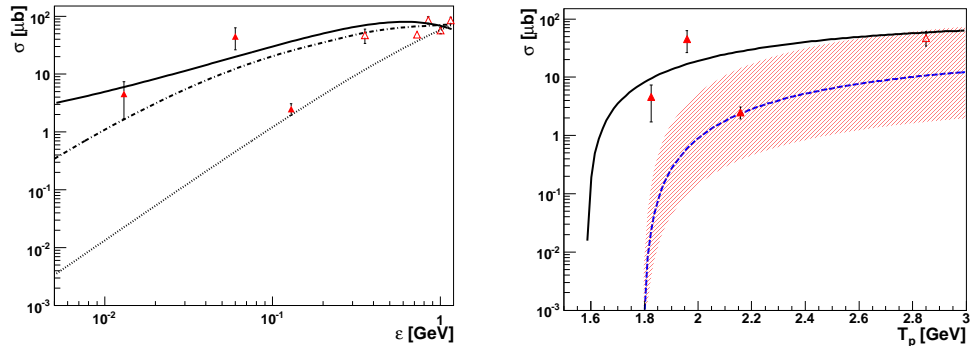


Figure 1.6: The $pp \rightarrow K^+ n \Sigma^+$ total production cross section as a function of excess energy (left panel) and proton beam energy (right panel). The data points from Ref. [48, 28] and Ref. [23] are shown by the closed and open triangles, respectively. In the left panel, numerical calculations of the Σ^+ total cross section from Ref. [49] are shown by the dash-dotted line, the three-body phase space with the constant matrix element and parametrisation for the $pp \rightarrow K^+ n \Sigma^+$ from Ref. [50] are shown by dotted and solid lines, respectively. In the right panel, the parameterisations for the energy dependence of Λ and Σ^0 total cross sections [31] are shown by solid and dashed lines, respectively. The red hatched area in the right panel indicates the range of $\sigma(\Sigma^+)$ allowed by the triangle inequality resulting from isospin invariance (see text).

Σ^+ production should be observed on top of the Λ and Σ^0 contributions, which can be calculated using a model and normalised to the corresponding total cross sections. The Σ^+ hyperon decay has a BR of 52% to $p\pi^0$ [47], so that some contribution from this reaction channel should also be observed in the measured K^+p missing mass spectrum. The $pp \rightarrow K^+ n \Sigma^+$ reaction channel can be clearly identified using $K^+\pi^+$ coincidences that arise due to the $\Sigma^+ \rightarrow n\pi^+$ decay (BR 48.3%). The beam energy of 2.16 GeV is above the $\Lambda\pi^+$ threshold. However, from the literature it is known that the total cross section of the $pp \rightarrow K^+ n \Lambda \pi^+$ reaction at the much higher energy 2.88 GeV is only about 4% of the Σ^+ cross section [17]. Assuming phase space distributions, it is then expected that at 2.16 GeV this contribution should be less than 2%. The $K^+\pi^+$ analysis shows that the Σ^+ and Σ^0 total cross sections are roughly equal at $\epsilon \approx 128$ MeV [28]. Furthermore, the Σ^+ total cross sections reported by COSY11 collaboration at much smaller excess energies are more than an order of magnitude larger than those found at ANKE. Taken at face value, the two sets of measurements can only be con-

sistent if there is a very large threshold anomaly. Two more data points on Σ^+ production obtained with the COSY-TOF detector and reported in PhD theses [37, 38] (See Table A.11) show moderate values of $\sigma(\Sigma^+)$ at $\varepsilon = 96$ and 129 MeV, which might support the existence of a threshold anomaly (see Fig. 1.6). The investigation of a possible threshold anomaly was one of the principal motivations for the measurements [51] which are the basis of the present thesis.

The ratios of the total cross sections $R(\Sigma^+/\Sigma^0) = \sigma(pp \rightarrow K^+n\Sigma^+)/\sigma(pp \rightarrow K^+p\Sigma^0)$ measured close to threshold are 230 ± 70 and 90 ± 40 at 1.826 and 1.958 GeV, respectively [48, 52]. Model independent limits on $R(\Sigma^+/\Sigma^0)$ can be obtained from the isospin relation that link the different Σ production channels, the amplitudes for which satisfy:

$$f(pp \rightarrow K^+n\Sigma^+) + f(pp \rightarrow K^0p\Sigma^+) + \sqrt{2}f(pp \rightarrow K^+p\Sigma^0) = 0 \quad (1.2)$$

This leads to the following triangle inequality between the total cross sections:

$$\begin{aligned} & \left[\sqrt{\sigma(pp \rightarrow K^0p\Sigma^+)} - \sqrt{2\sigma(pp \rightarrow K^+p\Sigma^0)} \right]^2 \leq \sigma(pp \rightarrow K^+n\Sigma^+) \\ & \leq \left[\sqrt{\sigma(pp \rightarrow K^0p\Sigma^+)} + \sqrt{2\sigma(pp \rightarrow K^+p\Sigma^0)} \right]^2 \end{aligned} \quad (1.3)$$

Now at $\varepsilon \approx 129$ MeV ($T_p = 2.16$ GeV), $\sigma(pp \rightarrow K^0p\Sigma^+)$ [53] is nearly equal to $\sigma(pp \rightarrow K^+p\Sigma^0)$ [48] so that the inequality predicts that $R(\Sigma^+/\Sigma^0) < 6$ at this excess energy. The COSY11 results exceed this limit by more than an order of magnitude, though they were obtained closer to threshold where no other $K^0p\Sigma^0$ data have been published.

The COSY11 result on the $pp \rightarrow K^+n\Sigma^+$ total cross section initiated a lot of theoretical activity. In principle, most of the theoretical models for the hyperon production in pp interaction predict not only Λ and Σ^0 cross section but also that for the Σ^+ [44, 46, 41]. However, most of these models were developed before the COSY11 data were published, and they were only tested against the high energy data that were available at that time [23]. Close to threshold most of the models predicted a phase-space-like behaviour, which is not in conflict with our experimental result at $\varepsilon = 129$ MeV [28] but is in striking disagreement with the COSY11 result at $\varepsilon = 13$ and 60 MeV [48].

The meson exchange model of Ref. [44] suggests that the ratio $R(\Sigma^+/\Sigma^0)$ depends on the type of interference between the K^+ and π^+ exchange mechanisms. In the case of destructive interference, supported by the analysis of the available Λ and Σ^0 experimental data, the ratio is $R(\Sigma^+/\Sigma^0) \sim 3$, while in the case of constructive interference it is $\sim 1/3$ [44]. In the resonance model of Ref. [46] it is believed that ρ and η exchanges dominate

Σ production in pp interactions at low energies, though this model slightly underestimates the Σ^+ total cross section at $\varepsilon = 356$ MeV [23].

The $pp \rightarrow K^+n\Sigma^+$ reaction is a very good channel for the investigation of the role of Δ^* isobars that decay into $K^+\Sigma^+$ [54]. Due to charge conservation, N^* resonances cannot contribute to this reaction channel. This is in contrast to Λ and Σ^0 production, where N^* resonances probably play an important role.

The authors of Ref. [49] found that $\Delta^{++}(1620)1/2^-$ formation, excited via ρ exchange, gives the overwhelmingly dominant contribution to Σ^+ production close to threshold. In addition to this previously ignored resonance, a strong $n\Sigma^+$ FSI, with parameters taken from the $p\Lambda$ FSI [31], was included in the calculations. A comparison of their numerical results with the data on the Σ^+ production cross sections in the COSY energy range is presented in Fig. 1.6. The slight underestimation of the two lowest data points is attributed to the interference term between π and ρ exchange, which was not included in the calculation. This model was published before the ANKE data [28] were available.

Another resonance model that describes both scenarios of energy dependence of the total cross section has been published recently [50]. The inclusion of only the $\Delta^{++}(1920)$ and π exchange allows one to describe the high energy data together with the one ANKE point, while the inclusion of an additional $\Delta^{++}(1620)$ resonance allows one to describe the very high close-to-threshold data from COSY11. It is found also that a strong $n\Sigma^+$ FSI would not help to describe the near threshold data within only the $\Delta(1920)$ model [50]. It is concluded that the $\Delta(1620)$ is indispensable for a good reproduction of the COSY11 data [50]. The comparison of the parametrisation from Ref. [50] with the experimental data is also shown in the Fig. 1.6.

In order to resolve the inconsistency between the available experimental data [48, 28] a new experiment has been scheduled and performed at COSY-ANKE [51]. This is the topic of present thesis.

1.2.6 Other hyperon production channels

It is natural to try to separate the remaining hyperon production channels into those with three and four body final states. The hyperons produced in three body final states, such as $pp \rightarrow K^+p\Sigma(1385)$, $pp \rightarrow K^+p\Lambda(1405)$ [56] and $pp \rightarrow K^+pY(1480)$ [55], are of special interest due to their unknown nature and quark structure. But, due to the relatively high masses of these hyperons, the experimental data discussed in this thesis are collected at energies that are well below the thresholds for those hyperon channels. Thus, we shall not go here into the details of these production channels.

The available experimental data on the $pp \rightarrow K^+p\Lambda\pi^0$, $pp \rightarrow K^+n\Lambda\pi^+$ and $pp \rightarrow K^+p\Sigma^0\pi^0$ reactions from Ref. [23] are presented in Fig. 1.7. The total cross sections are an order of magnitude smaller than those for the light hyperons at these energies. Therefore, in the analysis of the experimental data discussed in this thesis, effects from four body reaction channels were not considered.

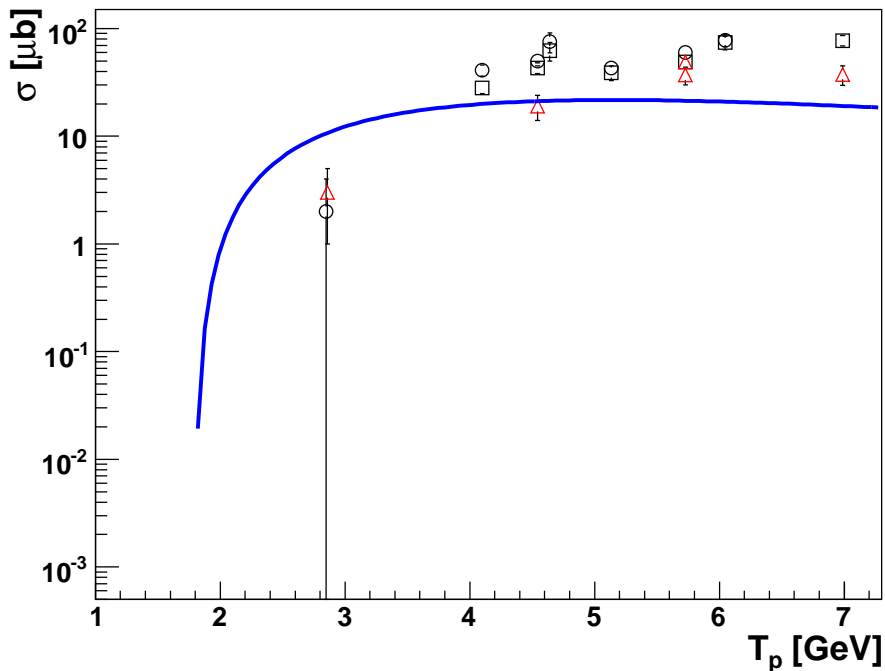


Figure 1.7: The total cross section for $pp \rightarrow K^+p\Lambda\pi^0$ (squares), $pp \rightarrow K^+n\Lambda\pi^+$ (circles), and $pp \rightarrow K^+p\Sigma^0\pi^0$ (triangles) from Ref. [23] as a function of the proton beam momentum. The parametrisation for the $pp \rightarrow K^+p\Sigma^0$ reaction from Ref. [31] is shown by the solid line.

1.3 Theoretical models for the different K^+ production channels

Meson exchange [44] and resonance [46] models are commonly used in the description of hyperon production close to threshold. The Feynman diagrams for the two types of model are presented in Fig. 1.8. Most of the

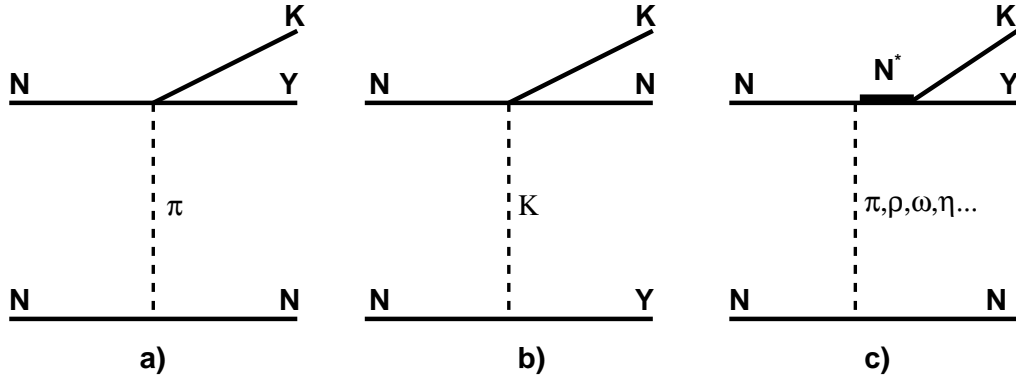


Figure 1.8: The Feynman diagrams used in the meson exchange (a,b) and resonance (c) models.

models try to describe different hyperon production channels using the same set of parameters and formalism. However, there are very few models that predict differential and polarised observables; most of them do not go beyond a calculation of total cross sections.

1.3.1 Meson exchange model

The meson exchange models generally use the exchange of π and K mesons for the total cross section calculations. The corresponding Feynman diagrams are presented in Fig. 1.8a,b. Within this model the total cross section can be calculated using the following equation [57]

$$\sigma = \frac{1}{2^9 \pi^3 q^2 s} \int dt ds_1 \frac{q_K}{\sqrt{s_1}} |M(t, s_1)|^2, \quad (1.4)$$

where q is the momentum of the incident proton in the centre-of-mass (CM) system, s is the square of the CM total energy, t is the square of the four-momentum carried by the pion, s_1 is the square of the centre-of-mass energy in the $p\Lambda$ system, q_K is the kaon momentum in the $K\Lambda$ CM subsystem, and $M(t, s_1)$ is the matrix element of the reaction.

In case of the simple one-pion-exchange model, the absolute square of the matrix element is given by:

$$|M(t, s_1)|^2 = g_{N\Lambda\pi}^2 \frac{t}{(t - \mu^2)^2} F(t) |A_{\pi^0 p \rightarrow \Lambda K}(s_1)|^2, \quad (1.5)$$

where μ is the pion mass, $g_{NN\pi}$ is the $NN\pi$ coupling constant, $A_{\pi^0 p \rightarrow \Lambda K}(s_1)$ is the $\pi^0 p \rightarrow \Lambda K$ reaction amplitude, and $F(t) = (\Lambda_\pi^2 - \mu^2)/(\Lambda_\pi^2 - t)$ is a form factor that depends explicitly on the Λ_π cut-off mass.

The $\pi^0 p \rightarrow \Lambda K$ amplitude is determined by the total cross section:

$$|A_{\pi^0 p \rightarrow \Lambda K}(s_1)|^2 = 2^4 \pi s_1 \frac{q_\pi}{q_K} \sigma_{\pi^0 p \rightarrow \Lambda K}(s_1), \quad (1.6)$$

with q_π and q_K being the pion and K^+ momentum, respectively. By taking the values of $\sigma_{\pi^0 p \rightarrow \Lambda K}(s_1)$ from experimental data, the effects of possible N^* resonances are automatically implemented in the calculation. The $g_{NN\pi}$ coupling constant and Λ_π cut-off mass are parameters of the model, determined using an NN potential (for example Bonn-NN potential [58]) and from data on pion production in pp interactions. By isospin symmetry, $\sigma_{\pi^0 p \rightarrow \Lambda K} = \sigma_{\pi^+ n \rightarrow \Sigma^0 K}$ and this is applied in order to obtain relations between the Λ and Σ^0 channels.

Although the formulae for one pion exchange are simple, most of the meson exchange models used for the description of experimental data exploit π and K exchange simultaneously [41, 44]. For kaon exchange, a formalism similar to that for pion exchange is valid but, due to the poor quality of the $KN \rightarrow KN$ data, the parameters are far more uncertain. In the close-to-threshold regime, the effect of the $p\Lambda$ FSI must be taken into account. The authors of Ref. [44] treat final state interaction effects in a careful way, using the Jülich and Nijmegen YN potentials. Predictions of both models, after implementation of initial state interactions, describe the experimental data on Λ and Σ^0 total cross sections close to threshold reasonably well. It is found that Λ production is dominated by the K exchange, while in Σ^0 production K and π exchanges have comparable strength. The large $R(\Lambda/\Sigma^0)$ ratio, observed experimentally near threshold, cannot be explained purely by FSI effects. It is concluded that only a destructive interference between K and π production mechanisms can lead to the observed Σ^0 production suppression close to threshold.

1.3.2 Resonance model

In resonance models the strangeness is produced via the exchange of different mesons π, η, ω, ρ with an explicit inclusion of baryon resonance excitation. The generic Feynman diagram corresponding to the resonance model is presented in Fig. 1.8c. Reference [46] includes the following ingredients:

- All resonances that are experimentally observed to decay into the hyperon and kaon. For example, in the case of $pp \rightarrow K^+ p\Lambda$, it includes the $N^*(1650)$, $N^*(1710)$ and $N^*(1720)$.

- Kaon exchange is not included in the model.
- Resonances are treated as elementary particles but their widths enter the propagators.
- No final state interaction is included in the model.

The model describes the experimental data for different hyperon channels Λ , Σ^0 and Σ^+ at high energies very well, while in the near-threshold region the description of the Λ total cross section gets worse due to the neglect of $p\Lambda$ FSI.

A similar type of models for the prediction of the total cross section for the $pp \rightarrow K^+n\Sigma^+$ reaction is presented in Ref. [49,50]. But the authors there introduce in addition the previously ignored Δ isobars and FSI in order to obtain a better description of the experimental data.

Chapter 2

Experimental setup

The experiment has been carried out at the COoler-SYncrotron (COSY-Jülich) [59], which provides polarised and unpolarised proton and deuteron beams with momenta up to 3.7 GeV/ c to external and internal target stations. COSY is equipped with electron and stochastic cooling systems that can be used in the energy ranges of 40 – 183 MeV and 830 – 2830 MeV, respectively. Usage of the cooling systems reduces the beam momentum resolution from a typical value of $\Delta p/p = 10^{-3}$ down to $\Delta p/p = 10^{-4}$ with only a moderate loss of beam intensity. A sketch of the COSY layout is presented in Fig. 2.1. A typical unpolarised COSY proton beam intensity is of the order of $\sim 10^{10}$ particles per spill with a revolution frequency of $\sim 10^6$ Hz. The intensity of the polarised proton beam is about a factor five smaller than unpolarised one.

2.1 The ANKE magnetic spectrometer

The ANKE magnetic spectrometer [60] is placed in an internal target position of COSY. It can be equipped with either unpolarised cluster [61], polarised gas [62] or solid strip targets [63], which allow experimentalists to perform studies of elementary and nuclear reactions with polarised and unpolarised proton and deuteron beams up to the maximum momentum available at COSY. The unpolarised cluster target provides areal target densities of the order of $3 - 5 \times 10^{14} \text{ cm}^{-2}$, which lead to typical luminosities of $6 - 8 \times 10^{30} \text{ s}^{-1} \text{ cm}^{-2}$. The polarised gas target makes possible double polarised experiments with luminosities of up to $10^{29} \text{ s}^{-1} \text{ cm}^{-2}$ [64]. The ANKE magnetic spectrometer consists of three dipole magnets (See Fig. 2.2). The D1 and D3 magnets are used, respectively, to direct the COSY beam onto the target from the non-disturbed COSY orbit and to return it back. The

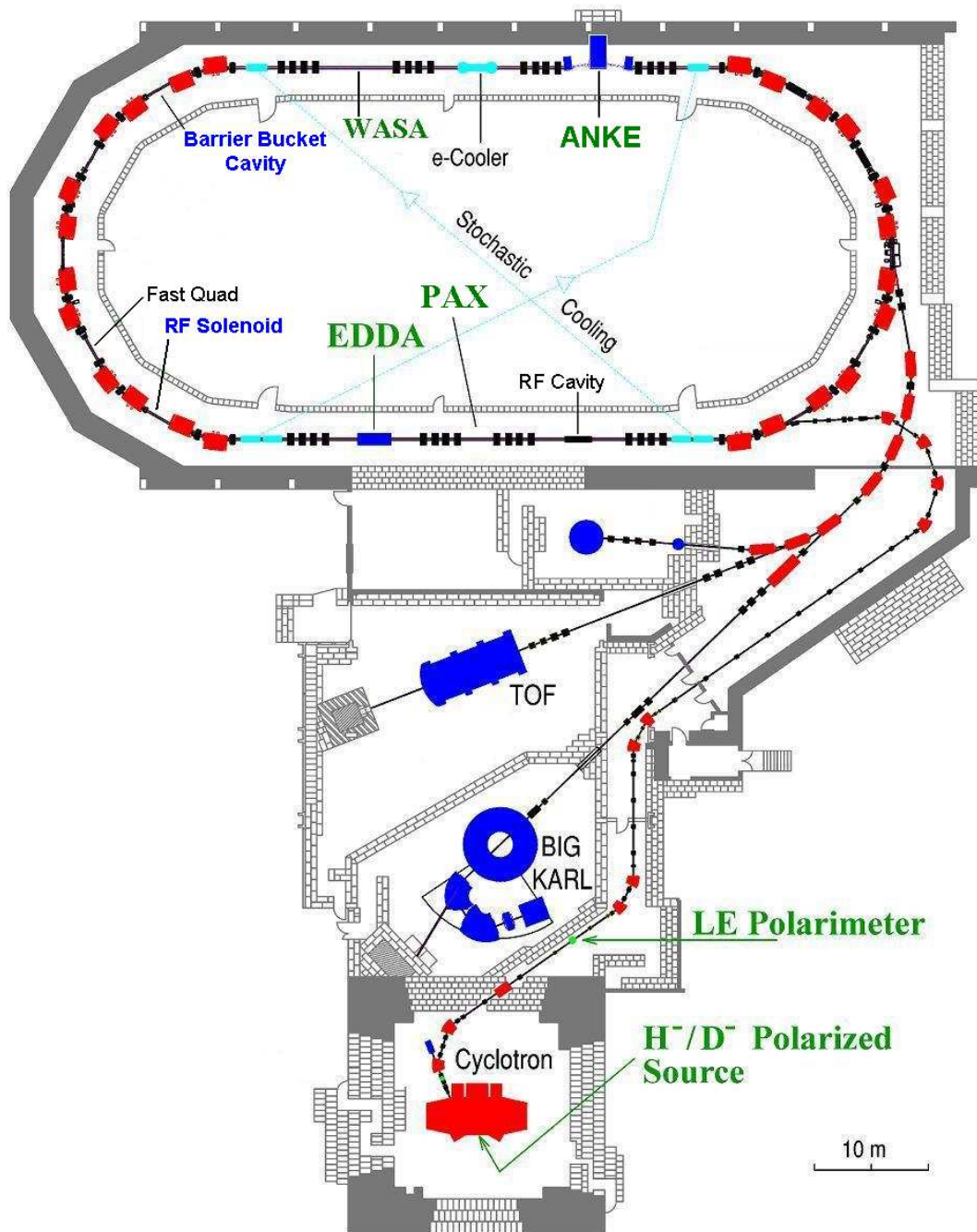


Figure 2.1: The COoler-Synchrotron COSY-Jülich

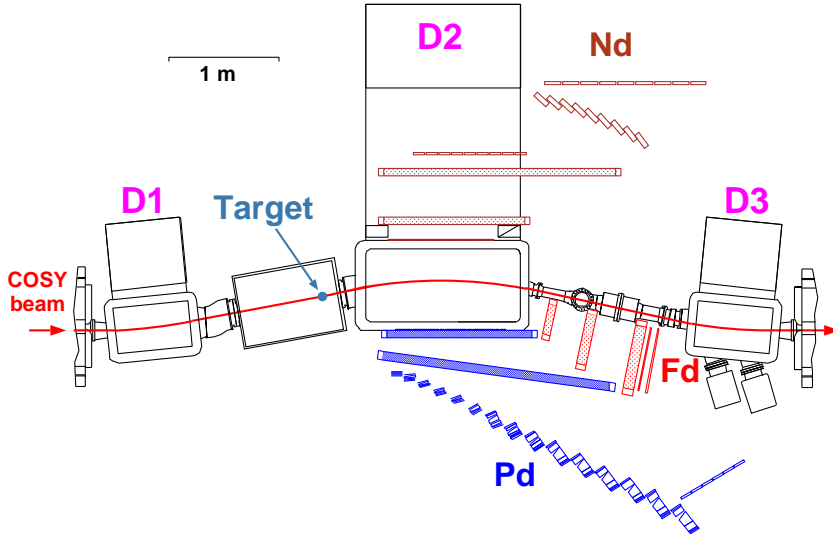


Figure 2.2: The magnetic spectrometer ANKE.

deflection angle of the COSY beam is determined by the beam momentum and field (B) settings in the spectrometer magnet. The D2 magnet has a maximum field of 1.57 T, a maximum deflection angle of 10.6° and a vertical gap of 200 mm. The spectrometer has an angular acceptance $\pm 3 - 5^\circ$ in the vertical and $\pm 10 - 18^\circ$ in the horizontal directions, depending upon the particle momentum. Depending on the conditions of the experiment, the selected field and beam momentum, D2 is movable in the horizontal direction perpendicular to the beam trajectory. The shift of the D2 axis with respect to the COSY axis determines the ANKE deflection angle and is set using a linear drive.

A target chamber is placed in front of the spectrometer magnet. Depending on the experimental requirements, a solid strip target, a spectator detector or a storage-cell for the polarised internal gas target can be installed in the target chamber. The polarised gas target or the cluster-jet target and their catcher systems can be supplied to the target chamber. The typical transverse size of the cluster target used in the present experiment was ≈ 10 mm (FWHM) in the region of the beam-target interaction.

The D2 magnet deflects positively charged particles to the positive and forward detector systems, placed on the right hand side of the beam, and negatively charged particles to the so-called negative detector system. The energy and angle of the spectator proton from the proton-deuteron interaction can be simultaneously measured using a dedicated spectator detector, installed close to the interaction point. It is therefore possible to perform measurements on the quasi-free neutron target [65] and to identify precisely

the coordinates of the interaction point in the case of measurements with an extended storage cell target.

2.2 Detection systems

The positive and forward detector systems, used in presented analysis, are discussed in Sec. 2.2.1 and Sec. 2.2.2, respectively. The ANKE magnetic spectrometer is also equipped with negative and spectator detector systems presented in Sec. 2.2.3.

2.2.1 Positive side detection system

The positive side detection system (Pd) consists of 23 start and 21 stop scintillator counters for time-of-flight measurements and two multi-wire proportional chambers [60]. All the counters in the positive detector are read out by photomultipliers from both sides.

The start signals are provided by plastic scintillator counters mounted on the D2 magnet exit window. In order to reduce multiple scattering effect, which are especially significant for the low momentum particles, start counters have different thicknesses depending on the counter number. Counters 1 and 2 are only 0.5 mm thick, numbers 3, 4, 5 are 1 mm, and numbers 6 to 23 are 2 mm. All start counters have a height of 270 mm and a width of 50 mm and together cover the full geometrical acceptance of the positive detector.

All the ANKE stop counters have dimensions 100×10 mm and a height in the range of 520 – 1000 mm, depending on the counter number. The first 15 stop counters are part of the range telescopes used for measurements of the K^+ decay products. These allow the inclusive identification of low momentum K^+ in the subthreshold solid strip target measurements. The last six stop counters are part of the so-called side-wall detector. They are mounted on the platform and can be placed either in the gap between the fifteen telescope and the forward hodoscope or behind the forward hodoscope for energy loss measurements.

The first side (start) multi-wire proportional chamber (MWPC) is placed close to the ANKE start counters, the second (stop) side multi-wire proportional chamber is connected to the D2 magnet and moves together with D2. Both chambers have a similar structure and size, optimised for the ANKE acceptance. Each of the chambers consists of three planes with two planes of wires inclined by $\pm 23^\circ$ with respect to the vertical direction and one with vertically aligned wires. The two side multi-wire proportional chambers al-

	MWPC1	MWPC2
Gas	70% Ar+ 30% CO ₂	
N_{planes}	3	3
N_{wires}	512	768
wire spacing [mm]	2.54	2.54
size [mm]	350 × 1300	600 × 1960

Table 2.1: Parameters of the Sd MWPC.

low momentum reconstruction with a resolution of the order of $\sim 2\%$ (σ). The parameters of the side chambers are summarised in Tab. 2.1.

The ANKE magnetic spectrometer is equipped with 15 range telescopes for inclusive low momentum K^+ identification. Each of the telescopes is placed in the focal plane of the spectrometer magnet and is suited for the identification of certain kaon momentum. A range telescope consists of a stop counter, Čerenkov (only telescopes 7 – 15) counter, passive degrader made of copper, energy loss counter (ΔE), and veto counter. The thicknesses of the passive degraders are chosen such that the K^+ deposit the maximum amount of energy in the ΔE counter and stop either at the edge of it or in the second degrader. The decay products are then registered in the veto counter. The procedure of the K^+ identification using the delayed veto technique is described in detail in Sec. 3.2.2

2.2.2 Forward detection system

The ANKE forward detection system (Fd) consists of two multi-wire proportional chambers (MWPCs), one drift chamber (DC), and a scintillator hodoscope [66]. It is placed close to the beam pipe and is suited for high momentum heavy (proton and heavier) particle identification in the forward direction. The acceptance of the Fd detector is limited by the size of the thin (0.5 mm) forward window (240×212 mm) made from aluminium.

The counter hodoscope consists of two layers of plastic scintillators (8 and 9 counters) shifted with respect to each other by half the size of a counter. Six counters in the first and second layer of the hodoscope have dimensions of $80 \times 20 \times 360$ mm. Counters number 1 – 2 and 1 – 3 in the first and second layer of the hodoscope have thicknesses 15 mm and variable width of 40 and 60 mm in the first and 40, 50 and 60 mm in the second layer, respectively. Depending on the experimental requirements, the scintillator hodoscope can be equipped with Čerenkov light counters for proton-deuteron separation, or an additional layer of plastic scintillator (typically the side-wall is used) for

energy-loss measurements.

	MWDC1	MWPC2	MWPC3
Gas	80% Ar +20% C_2H_6	85% CF_4 + 15% C_2H_6	
N_{planes}^X	3	2	2
N_{planes}^Y	4	2	2
wire spacing [mm]	10	2.06	2.06
size [mm]	330×320	428×458	548×538

Table 2.2: Parameters of the chambers used in the Forward Detector.

The parameters of the FD chambers used at ANKE are presented in Table 2.2. Each of the FD proportional chambers consists of four wire and two strip planes. The strip planes, used as active cathodes, are combined with either two vertical (X) or two horizontal (Y) wire planes into the one module. Each proportional chamber contains two modules, one with vertical and one with horizontal wire planes. The dimensions of the chambers are optimised for the ANKE acceptance, which is limited by the ANKE D2 forward window. The ANKE forward drift chamber is placed close to the magnet and, together with the third proportional chamber, to a large extent determines the momentum resolution. It consists of seven wire planes with 10 mm spacing combined into two modules. The first module consists of three planes of vertically oriented wires, while the second module contains four planes with wires inclined by 30° . The complete set of the ANKE FD chambers provides $\sim 1\%$ (σ) momentum resolution for protons in the forward detector.

2.2.3 Other detection systems not used in analysis

A so-called negative detector (Nd) is used for the identification of negatively charged particles [67]. It comprises a set of 20 start and 22 stop counters for time-of-flight measurements, two multi-wire proportional chambers for momentum reconstruction and background suppression, and a set of 11 Čerenkov counters for pion background suppression in the high momentum region.

For experiments with a quasi-free neutron target [65] and for measurements with an extended polarised gas target, ANKE can be equipped with a set of silicon vertex telescopes. Each of these consists of two or three silicon strip detectors read out from both sides. The vertex telescopes, together with their electronics, are mounted in the vacuum chamber at distances of

2–3 cm from the interaction point. They provide angle and energy measurements of low momentum protons and deuterons, allowing the determination of the coordinates of the interaction point and the initial quasi-free neutron momentum.

2.3 Electronics, online triggers and data acquisition system

The structure of an individual scintillator readout channel is presented in Fig. 2.3. In order to compensate for the dependence of the time shapers on

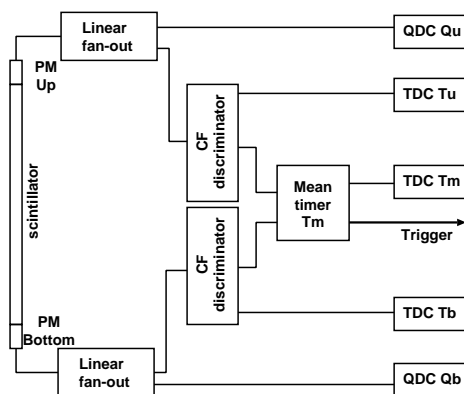


Figure 2.3: Structure of an individual scintillator counter readout channel.

the signal amplitudes, every time signal from the counter is read out through a constant fraction (CF) discriminator system. For the online trigger, fast time signals, mean timers (T_{mean}), independent of the position of the hit in the counter $T_{mean} = (T_{up} + T_{bottom})/2$, are used. A typical time resolution in the mean timer for the ANKE stop counters is on the order of 50 ps (σ). In general, from every counter two amplitudes Q_{up} and Q_{bottom} and three time signals T_{up} , T_{bottom} and T_{mean} are read out.

To select particles in the Sd on the trigger level, dedicated time-of-flight VME based modules are employed. Using one TOF module a common time-of-flight gate (length variable from 3 to 23 ns) between a single stop counter and sixteen adjustable start counters can be set. Thus, kaons in the Sd detector can be selected by time-of-flight already at the trigger level. The start counters for the coincidence with a certain stop counter (start-stop combinations) are chosen on the basis of the simulation to register particles with $\vartheta < 12^\circ$.

For the online K^+ identification using the ANKE range telescopes, a delayed veto trigger is used. In this trigger, cuts on the time difference between T_{mean} measured in the stop and the corresponding veto counter are applied.

In the forward detector, a coincidence trigger between two layers of the hodoscope has been used to reduce the combinatorial background. In this trigger a coincidence between the counter in the first layer and two counters in second layer is requested.

The multi-crate ANKE DAQ supports CAMAC, Fastbus and VME read-out systems [60]. Each individual crate is read out by an INTEL-PC running under UNIX (Net-BSD). Data from individual subsystems are transferred via Fast-Ethernet to the event-builder, a PC which creates events and writes experimental data onto a hard disk. In order to synchronise the readout of the individual sub-systems, each readout system has a synchronisation module developed for this purpose. Individual synchronisation modules are interfaced by a ring-like synchronisation bus. This DAQ was developed by Zentralinstitut für Electronic (ZEL FZ-Jülich) for experiments at COSY and is capable of writing to disk $\sim 50\%$ of events with an input trigger rate of up to 10kHz.

The digitisation of the signals as well as their storage on disk requires some time. Therefore every detection system has a so-called dead-time during which signals from the detectors cannot be accepted. In order to estimate the dead-time correction, scaler signals are used at ANKE. The scaler system is a separate system, which monitors the rate from the beam-target interaction region using signals from stop counters 2 to 5. One can draw a straight line between this group of counters and the target so that the rate in the counters is directly proportional to the luminosity and depends weakly on the background conditions. Counting the number of scaler signals accepted by the DAQ and the total number of hits in the scalers one can estimate the corresponding DAQ dead-time. Coincidences between stop counters 2 – 3, 4 – 5 and 2 – 5 form three different scaler signals which are read out with a frequency of 10 Hz.

2.4 Experimental conditions during data taking

The experiment discussed in this thesis was performed in September 2007 [51]. The main modification in the detector setup before the data taking was the implementation of a new detector support system which is connected

with the D2 magnet. The procedure for determining the detector position using measurements carried out in August 2007 is discussed in Sec. 3.1.

For all five beam energies, the momentum compaction factor was determined and the Schottky spectra have been monitored during the whole data taking. It was therefore possible to determine the luminosity and average beam momentum with some confidence (see Sec. 3.5.2).

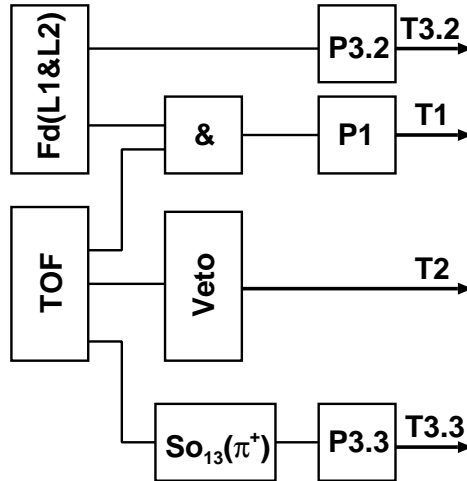


Figure 2.4: Trigger scheme used in the experiment

Momentum GeV/ c	T_p GeV	LA1 mm	α degree	P1	P2	P3.2	P3.3
2.546	1.775	278.9	8.038	4	1	1024	64
2.600	1.826	274.2	7.870	2	1	1024	64
2.700	1.920	263.1	7.577	4	1	1024	64
2.740	1.958	266.1	7.466	4	1	1024	64
2.806	2.020	258.2	7.289	8	1	1024	64

Table 2.3: Summary of experimental conditions selected for measurements with different beam momenta. Trigger pre-scaling factors P1, P2, P3.2 and P3.3 were used in the experiment. The α and LA1 are the deflection angle and linear drive positions, respectively.

In this experiment four different triggers with different pre-scaling factors have been used (Fig. 2.4).

- First trigger (T1) - suited for the selection of K^+p pairs using the

K^+ time-of-flight in the Sd and two-layer coincidence in Fd. It was pre-scaled (P1) during data taking due to the high count rate.

- Second trigger (T2) - suited for the clean K^+ identification using the delayed veto technique for the measurements of K^+ inclusive spectra and $K^+\pi^+$ coincidences.
- Third trigger (T3.2 and T3.3) - a combined normalisation trigger used for the measurements of pp elastic scattering and π^+ production for the relative energy monitoring. Both of these triggers were pre-scaled (pre-scalings P3.2 and P3.3) to reduce the accepted count rate to roughly 10% of the total trigger rate.

Pre-scaling factors (see Table 2.3) were changed from energy to energy in order to reduce the data-acquisition system (DAQ) dead time to below 30%.

Due to the failure in the veto counter readout channel number seven the delayed veto trigger (T2) efficiency for this telescope was significantly reduced. The telescope efficiencies determined for this experimental data are presented in Sec. 3.4.2.

During data taking at 1.826 GeV, due to a mistake in the preparation of the K^+p coincidence trigger (T1), events with the delayed veto trigger (T2) mask were written with the wrong trigger identification number. As a consequence, the efficiency of the trigger T1 and T2 intersect in the data is not known. This effect, which is only present at 1.826 GeV, could only be clarified by further analysis of K^+p coincidence data and it means that the results for Σ^0 production at this energy must be in some doubt.

Chapter 3

Data analysis

The analysis of experimental data implies detector calibration (using detector position information), particle identification, particle correlation analysis, and normalisation. The analysis of the experimental data collected in September 2007 was done using two different codes based on C++. The results of these two analyses are in full agreement.

3.1 Detector positions

Tracking detectors are designed to provide information about a trajectory with a precision better than 1 mm and this defines the momentum resolution. However, for the absolute momentum calibration a good knowledge of the magnetic field and detector positions is required. Therefore, it is very important to determine the detector positions with the utmost accuracy.

The installation of the new detector support system of the ANKE forward and side detectors was completed in August 2007 (Fig. 3.1). From this time onwards the ANKE side stop chamber rotates around an axis that is fixed with respect to the D2 magnet at the low momentum side. The high momentum side of the chamber support is fixed on the Fd platform such that it keeps a constant distance between the second forward MWPC and the stop MWPC in the side detector. The complete forward detector system is mounted on a single platform that is fixed to the COSY beam pipe and rotates around a point fixed on the D2 magnet. A linear drive (LA1), which determines the distance between the COSY beam axis and the centre of ANKE D2 magnet in the X direction, fixes the positions of all the ANKE detectors in a predictable way. This system allows the determination of the detector position for any arbitrary ANKE deflection angle on the basis of measurements done for a single D2 position.

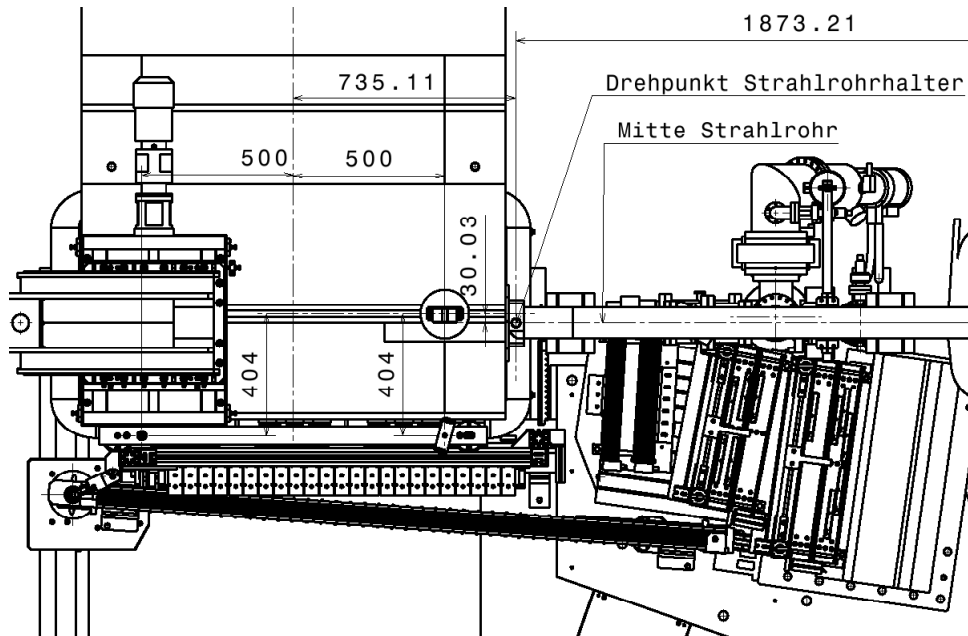


Figure 3.1: Sketch of the ANKE detector system.

Precision measurements of the ANKE detector positions have been done for several settings of the D2 spectrometer magnet. In these measurements the coordinates of ten points on the ANKE detectors have been determined in an arbitrary coordinate system. Each set of measurements contains information on the coordinates of the rod installed at the top of the D2 magnet. The position of the rod with respect to the centre of the ANKE coordinate system, which coincides with the centre of the D2 chamber, is precisely known. Thus, the coordinates of the rod are used to transform the measured detector coordinates into the ANKE coordinate system.

A simple C++ code has been developed that uses a selected set of the measured points to output the detector coordinates for any linear drive position [68].

The analysis of all the data shows the internal consistency of the measurements at different positions of the linear drive. The dimensions of the detectors, as well as the distances between them, remain constant with a precision of roughly ~ 0.1 mm (see Table 3.1). However, the geometrical sizes of the wire chambers extracted from all the measurements differ from the design drawings. This leads to a systematic shift in the detector positions, which has been determined using the calibration reactions.

The position of every ANKE detector element is determined as the co-

Detector	S_{meas} mm	S_{known} mm
Rod	1000.14 ± 0.09	1000
SdMWPC2	2126.67 ± 0.10	2125
FdMWDC1	361.12 ± 0.06	360
FdMWPC2	472.53 ± 0.04	472
FdMWPC3	594.04 ± 0.07	592

Table 3.1: Comparison between the measured and known dimensions of the detectors.

ordinate of the certain point fixed on the detector and the angle between the detector plane and Z axis of the ANKE coordinate system. All sets of measurements can be transformed to the setup for a certain selected linear drive position, the results of such conversion are presented in Table 3.2. The

Detector	X mm	Z mm	α_z degree
SdMWPC2	-766.66 ± 0.06	327.56 ± 0.10	-5.25 ± 0.01
FdMWDC1	-539.65 ± 0.24	979.95 ± 0.21	78.75 ± 0.02
FdMWPC2	-749.18 ± 0.24	1354.46 ± 0.32	70.94 ± 0.02
FdMWPC3	-951.82 ± 0.26	1598.62 ± 0.27	73.86 ± 0.01
FdOrig	-905.41 ± 0.29	1722.41 ± 0.26	73.09 ± 0.01

Table 3.2: Example of ANKE detector coordinates obtained from transformation of all measurements to the same linear drive position (LA1=274.2 mm). FdOrig - coordinate of the point on the Fd hodoscope fixed in the geometrical setup of the detector.

resulting errors of the detector positions in Table 3.2, calculated assuming equal accuracy of the measurements, shows that the transformation from one linear drive coordinate to another is not absolutely linear. Therefore, for the preparation of the setup for certain D2 settings it is better to use measurements done for the closest value of the linear drive.

The results of the calibration of the Fd detector position using proton-proton elastic scattering for different values of LA1 are presented in Table 3.3. A systematic shift in the X coordinate for the first and second chambers has been implemented on the basis of the information about the reconstructed track. The difference between the values of the shifts for different energies is of the order of the measurement uncertainty.

LA1	Δ_{dc1}	Δ_{pc2}	Δ_{pc3}
278.9	0.75	1.37	0
274.2	0.94	1.47	0
266.1	0.59	1.27	0
263.1	0.59	1.27	0
258.2	0.75	1.47	0

Table 3.3: Systematic shift of the chamber positions determined from the experimental data as a function of the linear drive position. All dimensions are in millimetres.

In this way, using the developed procedure it is possible to determine the detector positions for any arbitrary D2 position with a relative precision of ~ 0.2 mm. However, due to the limited knowledge about the dimensions of the detectors, some fine tuning of detector positions must be done using calibration reactions, for example pp elastic scattering in the case of the Fd detector.

3.2 Experimental methods

In this section, the experimental methods of the data analysis used in this thesis are discussed. Particle identification methods used at ANKE are described in greater detail in Refs. [72] and [66] for the Sd and Fd detectors, respectively.

3.2.1 Time of flight

The main criterion for particle identification in the side detector are time-of-flight (TOF) measurements. Typical TOF spectra for individual start-stop combinations for counter number thirteen are presented in Fig. 3.2. Two prominent peaks are seen for almost all the start-stop combinations. The left peak corresponds to the pions coming from the target, its width and position being almost independent of the start counter number; due to their low mass the π^+ are moving close to the speed of light. In contrast to this, the position and width of the proton peak (the right peak in Fig 3.3a) changes, depending on the particle momentum, which increases with counter number.

The TOF spectra, summed over the all the start counters, are shown in Fig. 3.3. The experimental data discussed in this thesis were collected either with a K^+ or a π^+ TOF online trigger so that there is no proton peak in

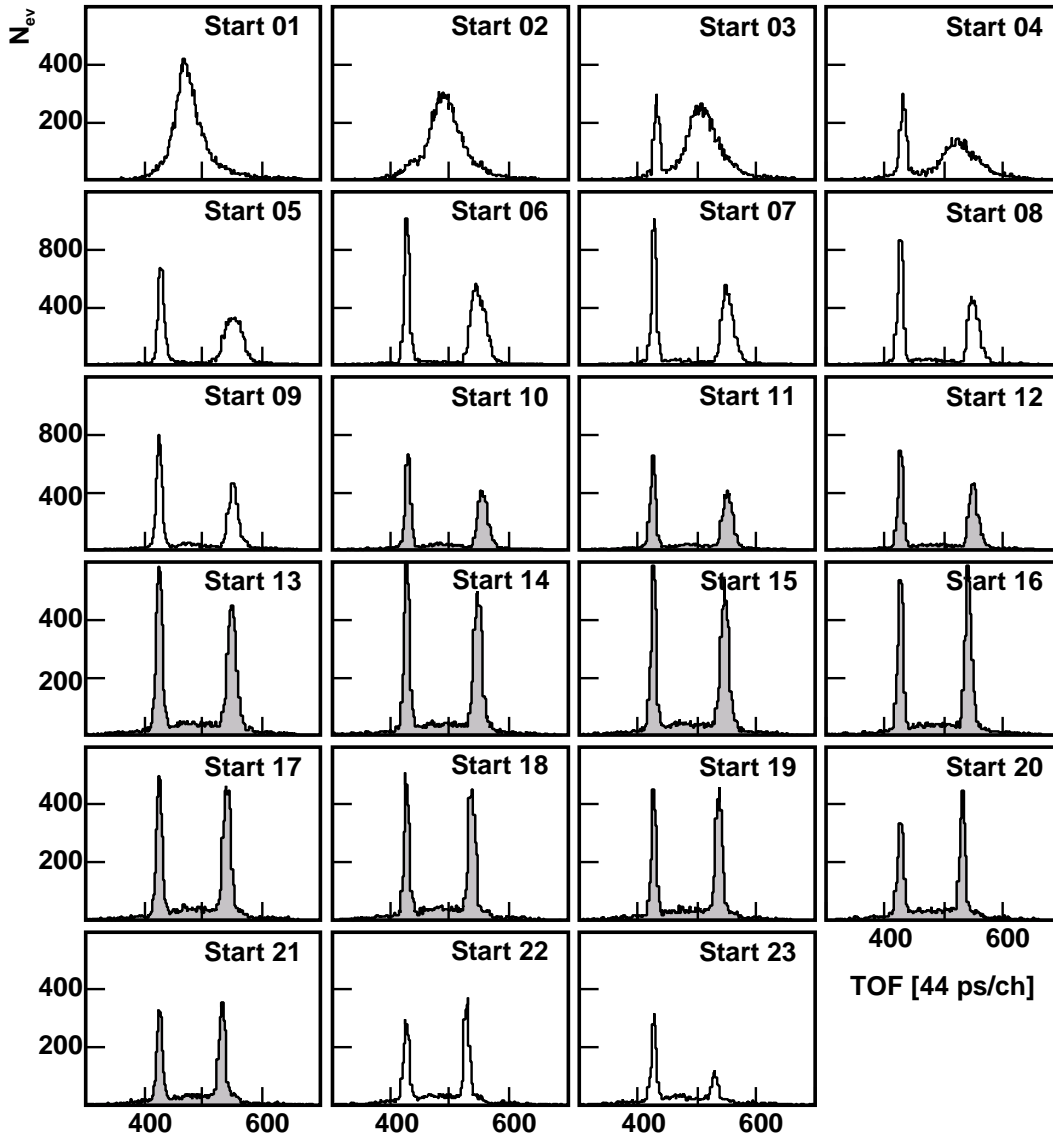


Figure 3.2: Individual time-of-flight spectra between stop counter 13 and all the start counters. Hatched histograms show start-stop combinations included in the online trigger. The data were collected using a carbon target at $T_p = 1.5$ GeV [11].

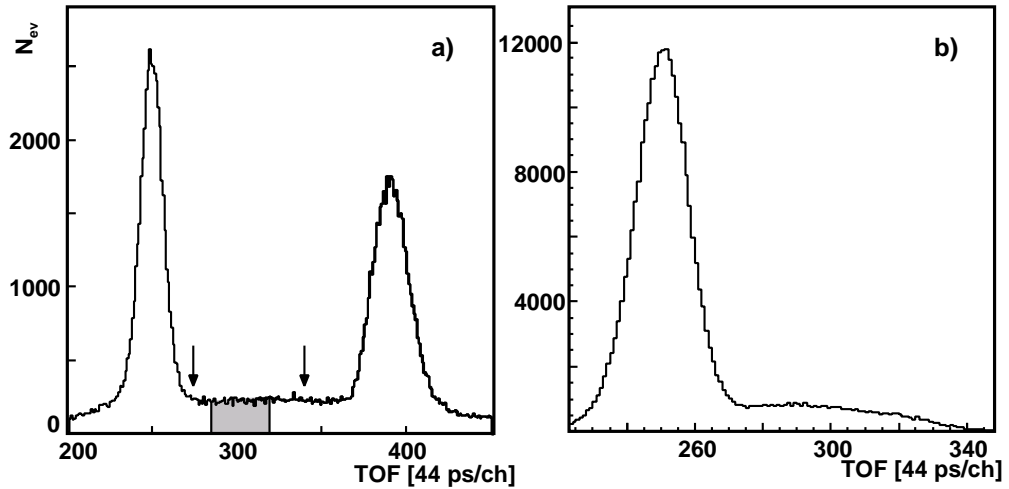


Figure 3.3: Time-of-flight spectra, summed over the all start counters, measured with carbon (a) and proton (b) targets at 1.5 [11] and 1.775 GeV, respectively. The proton peak in the spectra collected on the proton target was cut at the online trigger level.

Fig. 3.3b.

In principle, the time resolution in the ANKE time-of-flight spectra (~ 600 ps) is sufficient to separate K^+ from π^+ and p , but there is a significant background contribution in the region where the signal from kaons should be observed. This background is connected with fast protons from the target that are rescattered on the pole shoes of the D2 magnet or elements of the vacuum chamber. These protons are not focused by the D2 and hence do not have any defined momenta. Therefore, they result in a broad background distribution in the TOF spectra.

3.2.2 Delayed veto technique

One of the main motivations for the construction of the ANKE magnetic spectrometer was the study of subthreshold K^+ production on nuclear targets [63]. The ANKE range telescopes exploit the so-called delayed veto technique for the identification of low momentum K^+ [69]. All the range telescopes are placed in the focal plane of the spectrometer magnet D2. Thus, every telescope registers particles over a relatively small momentum range $\Delta p/p = 7 - 24\%$, which is limited by the width (100 mm) of each telescope and by the field in D2. This system allows one to discriminate between K^+ mesons and other particles by using the differences in energy losses and

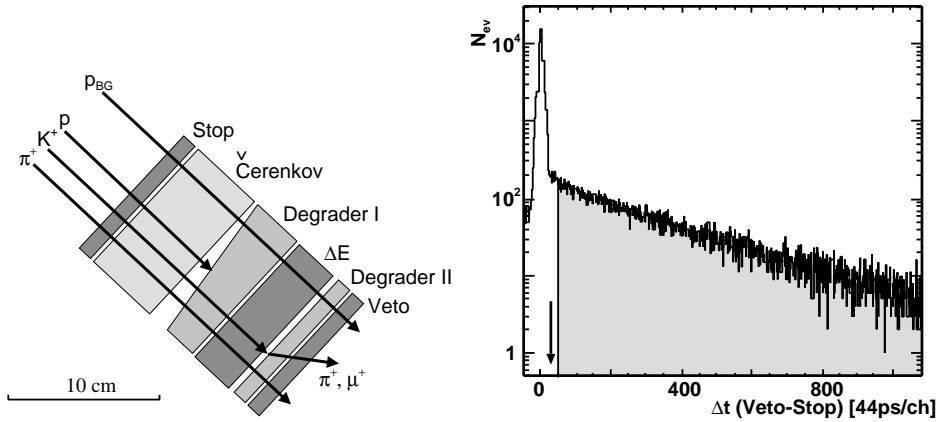


Figure 3.4: Principles of the delayed veto technique. Structure of the ANKE range telescopes (left panel). Time difference between the veto and stop counter number thirteen measured on a carbon target at 2.3 GeV [11] (right panel). The prominent peak from the pion background is seen. The hatched area and arrow indicate the cuts used in the offline and online analysis, respectively.

ranges for different particles.

The structure of the ANKE range telescope is presented in Fig. 3.4. As already described in Sec. 2.2.1, each telescope consists of vertically oriented scintillators and copper degraders. One function of the first degrader is to stop protons originating from the target and to prevent them from entering the ΔE counter. Their further function is to decelerate K^+ mesons such that they deposit maximum energy in the ΔE counter and stop either at the edge of it or in the second degrader. The tapered shape of the degrader takes into account the change in the particle momentum over the individual telescope. Each telescope is placed such that the first degrader is located in the focal plane of the D2 magnet in order to minimise the range spread of the K^+ mesons. Pions from the target pass through the system almost unaffected due to their high speed and result in a small energy loss in all the counters. Kaons, which are stopped in the ΔE counter or in the second degrader, decay via $K^+ \rightarrow \mu^+ \nu_\mu$ (BR 63.54%) or $K^+ \rightarrow \pi^+ \pi^0$ (BR 20.68%) with a lifetime of $\tau = 12.4$ ns [47]. The decay products, μ^+ and π^+ , are emitted isotropically and can be registered in the veto counter giving signals with a characteristic delay with respect to the signals in the stop and energy loss counters.

A typical measured time difference spectrum between veto and stop counters is presented in the Fig. 3.4. Using a dedicated delayed veto module at the online trigger level, an individual cut on the veto-stop time difference for

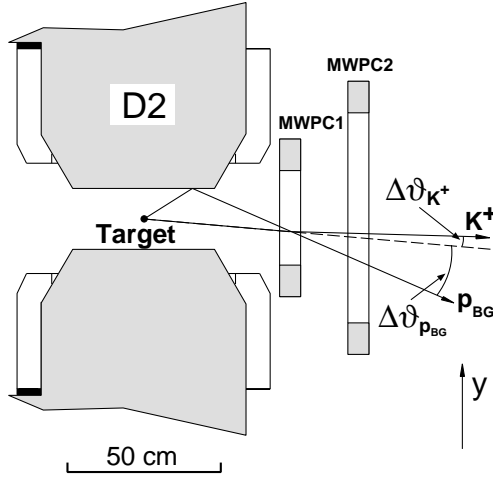


Figure 3.5: Principle of vertical angle cut. Ejectiles from the target (K^+) and scattering background (P_{BG}) in general have different vertical angles ϑ in the spectrometer.

each telescope has been applied for the K^+ identification.

3.2.3 Vertical angle cut

The principle of the vertical angle cut is illustrated in Fig. 3.5. Particles from the target within the angular acceptance pass through the first MWPC at some vertical coordinate y , from which one can expect some certain vertical angle ϑ_{K^+} to be measured by the second MWPC. Since all the particles from the target undergo multiple scattering on the vacuum foil of D2 and in the detector components, this causes some smearing $\Delta\vartheta_{K^+}$ in the vertical angle, measured by the second chamber. In contrast to the target ejectiles, scattered particles p_{BG} in general have a much large difference between the expected angle and the measured one in the second chamber $\Delta\vartheta_{p_{BG}}$. The measured vertical angle distributions for selected K^+ using the delayed veto technique and summed over all the stop counters are shown in the Fig. 3.6a. The prominent peak from the target ejectiles is seen with a small background on the sides of the peak. The moderate background from rescattered particles is connected with the relatively high K^+ production cross sections at energies where these data have been collected.

The K^+ TOF spectra measured with the delayed veto technique are presented in Fig. 3.6b after applying the vertical angle cut. The flat background under the clean K^+ peak is connected with the detection of rescattered par-

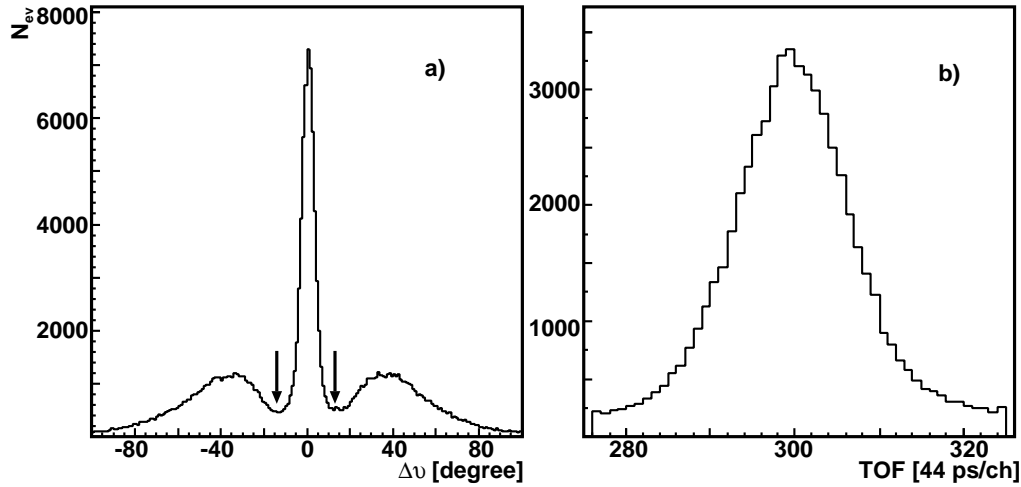


Figure 3.6: Vertical angle (a) and time-of-flight (b) distributions summed over all the stop counters for K^+ mesons, measured at 1.775 GeV on a proton target. Arrows on the vertical angle distribution indicate parameters of the cut used in the further data analysis.

ticles. It was further suppressed using time calibrations, and, in the case of the inclusive K^+ analysis, was subtracted from the time-of-flight spectra measured in individual telescopes.

3.2.4 Track selection and neighbouring counter analysis

Tracks from all the particles were reconstructed using the information from the MWPCs. In addition to the vertical angle cut described in Sec. 3.2.3, a limitation on the vertical coordinate Y of the reconstructed reaction vertex was imposed. For the tracks registered in the forward detector, standard cuts on the coordinates of the track intersection with the forward window were applied [66].

In the data analysis there are many events where two neighbouring counters fired simultaneously and sometimes with only one track in the event. For such cases a dedicated neighbouring counter analysis has been used. In the forward detector analysis the counter closest to the track is assigned to the track. In the analysis of the Sd detector, the number of the start or stop counter associated with the reconstructed track depends on the number of tracks and fired counters in the event:

- In the case where there is only one reconstructed track in the event and two start or stop counter hits, the start counter with the bigger number and stop counter with the smaller number is associated with the track.
- In the case where there is only one track reconstructed in the system, but more than two counters are fired, the counter with the earliest absolute time is associated to the track.
- In the case where there is more than one track and more than two counters fired simultaneously in an event, the counters are associated to the tracks on the basis of the distance of the track from the centre of the counter.

The analysis of neighbouring counters changes the shape of the edges of the individual counter distributions and this is of especial importance for the inclusive data analysis. A similar procedure of the neighbouring analysis has been used for the simulations.

3.2.5 Momentum reconstruction

The kinematical parameters of the particles have been determined using information about tracks detected in the chambers. In a first approximation for the tracks, box field and polynomial methods have been used for the particles detected in side and forward detectors, respectively.

In the box field method, the trajectory of the particle is described by the Lorentz force in the magnetic field of the magnet and is assumed to be a straight line after the particle has left the magnet. Under these assumptions, the magnetic field of the magnet can be described using two parameters, *viz* l_{eff} and w_{eff} . The value of l_{eff} can be calculated from the parameters of the experiment, *viz* the magnetic field B , the momentum of the beam p and the deflection angle α , using the simple formula $l_{\text{eff}} = 6.6712 p \sin(\alpha)/B$. The second parameter w_{eff} depends only very weakly on the beam momentum and its value is fixed using a calibration reaction. The box field method provides momentum resolution of the order of $\sim 2\%$ (σ).

For a fast analysis in the forward detector, the polynomial method has been used. In this method all three components of the particle momentum \vec{p} are approximated by a third order polynomial with four parameters $(\tan(\theta_{xz}), \tan(\theta_{yz}), x_w, y_w)$, where x_w and y_w are the coordinates of the track on the D2 exit window, and $\tan(\theta_{xz})$ and $\tan(\theta_{yz})$ are the projections of the particle angle on the XZ and YZ planes. In this approximation the three

components of the momentum are parameterised as

$$p_i = \sum_{k,l,m,n=0}^3 C_{k,l,m,n} x_w^k y_w^l \tan^m(\theta_{xz}) \tan^n(\theta_{yz}). \quad (3.1)$$

The coefficients $C_{k,l,m,n}$ of the method are determined using GEANT simulations. The momentum resolution of the polynomial method for the forward particle is of the order of $\sim 1\%$ (σ).

For the selected events the Runge-Kutta method has been used. In this method the differential equation $d\vec{p}/dt = q[\vec{p} \times \vec{B}]$ for the particle moving in the magnetic field is solved numerically using the Runge-Kutta algorithm [70]. The magnetic field of the spectrometer magnet D2, measured using the floating-wire technique [71], and the energy loss corrections are used in every step in this procedure. Thus, the trajectory length and time of flight from the target to every detector for every track has been calculated together with the coordinates of the hits on all the active detectors. This method provides the best precision of track reconstruction and was used, not only for the final data analysis, but also for the calibrations of the detector positions and time.

3.2.6 Time calibrations

In order to reduce the number of free parameters in the correlation analysis with several particles, it is necessary to calibrate the time measured in each system with respect to the information from one of the counters.

The principles of the Fd detector calibration are illustrated in Fig. 3.7. Using tracks registered in certain pair of counters, it is possible to calculate

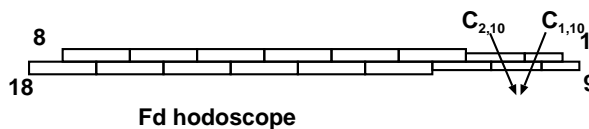


Figure 3.7: Principles of the Fd hodoscope calibration.

the parameters $C_{i,j}$, the difference between time signals from the same track in two fired counters, for all the Fd counters. Thus, by selecting one counter as a “base-counter”, it is possible to calibrate time from all the counters in the Fd detector with respect to it.

In order to improve the particle identification in the side detector and reduce number of free parameters in the correlation analysis, a method of time calibration for the events in the Sd detector has been developed. It

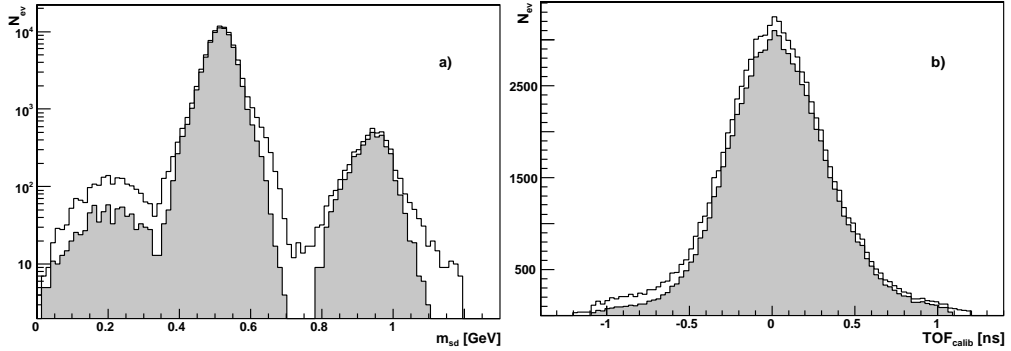


Figure 3.8: Principles of the time calibration. The invariant mass of the particle whose track was (a) detected in the Sd before and after (hatched histogram) applying cuts on the calibrated time-of-flight and vertical coordinate of the track. The calibrated time-of-flight distribution (b) before and after (hatched histogram) cutting on the vertical coordinate of the track. The data were collected at 1.920 GeV on the proton target with delayed veto trigger.

relies on the precise knowledge of a particle trajectory provided by the Runge-Kutta method used in the analysis of the data. The analysis is based on the assumption that the internal delays for the T_m of all the counters do not change during the measurements. The principles of the time calibration can be presented by the equation:

$$T_i^{So} - T_j^{Sa} + C_i^{So} - C_j^{Sa} = \tau_i^{So} - \tau_j^{Sa}, \quad (3.2)$$

where T_i^{So} and T_j^{Sa} are the times measured by the start and stop counters, τ_i^{So} and τ_j^{Sa} are the time necessary for a certain particle to fly to the particular detector, calculated using the trajectory reconstructed with the Runge-Kutta method. Thus, by solving system of $23 + 21 = 44$ linear equations, the parameters C_i^{So} and C_j^{Sa} could be determined.

The advantages of this calibration method with respect to others used at ANKE are:

- There is no need for a dedicated calibration run to determine the parameters (one run with a π^+ trigger is sufficient).
- The parameters of the calibration depend weakly on the type of the particle used for the calibration.
- A single system can be calibrated independent of the others.

- Using the calibrated time-of-flight between the start and stop counters and the information about the length of the trajectories between the counters in Sd detector, the mass of the registered particle can be calculated (See Fig. 3.8a).

In Fig. 3.8a the invariant mass of the particle whose track was detected in the Sd is presented on a logarithmic scale before and after applying all the cuts (hatched histogram). Three clean peaks from pions, kaons and protons are seen after applying all the cuts. Using the calibrated time in the counters, additional criteria can be introduced for particle identification in the Sd. These are the calibrated time difference between the start and stop counters $td_{\text{calib}} = T_i - \tau_i$ and the calibrated time-of-flight $TOF_{\text{calib}} = td_{\text{calib}}^{S_o} - td_{\text{calib}}^{S_a}$. In Fig. 3.8 a calibrated time-of-flight distribution is shown for the K^+ identified using the delayed veto. The same distribution after applying the additional (3σ) cut on the vertex of reconstructed track is shown by the hatched histogram. Thus, the cut on the vertical coordinate of the track, together with cut on the TOF_{calib} , allows one to reduce further the rescattering background in the data collected with the delayed veto trigger.

The calibrated time in the Sd and Fd detectors simplifies the analysis of the particle correlations and reduces the number of the free parameters (See Sec. 3.3).

3.3 Particle identification

Only information from the counters has been used for the particle identification in the online trigger. In the offline analysis, in addition to the more selective cuts in the counter distributions, information about the tracks of the particles have also been used.

Standard cuts on the tracks discussed in Sec. 3.2.4 have been used for particle identification in the Fd detector. The identification of particles in the Sd detector is based on the time-of-flight and vertical angle cuts (Sec. 3.2.1 and 3.2.3). For clean K^+ identification, the delayed veto analysis was used (Sec. 3.2.2) in addition to the time calibration discussed in Sec. 3.2.6.

3.3.1 K^+ identification

Taken together, time-of-flight measurements and track information from a single particle are insufficient to identify K^+ mesons on top of the rescattering background. Either an additional correlating particle in one of the detectors would have to be demanded or the delayed veto technique must be used [72]. In this latter case, the kaon momentum spectra can only be measured for

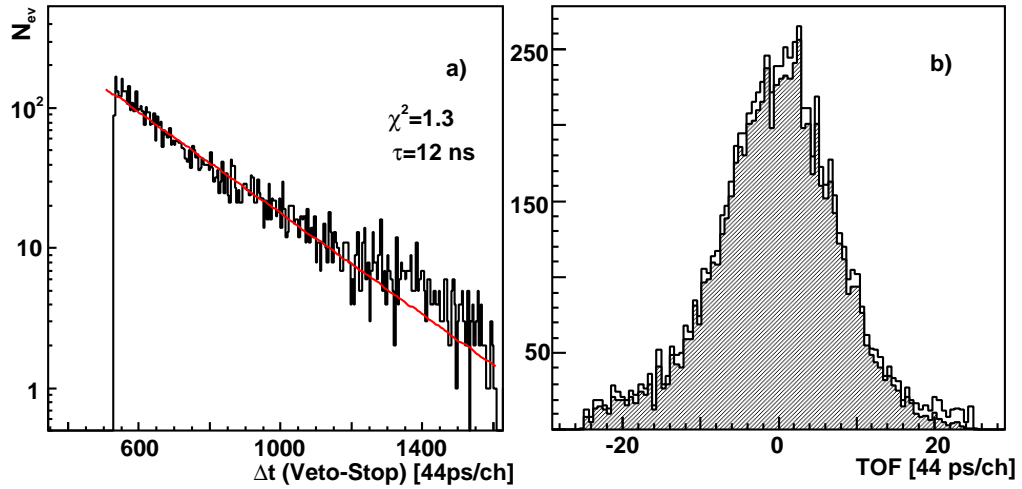


Figure 3.9: Time difference between the veto and stop counter (a) and time-of-flight spectra (b) for telescope number thirteen measured with a proton target at 1.775 GeV and 1.920 GeV, respectively. The fit of the delayed veto distribution with an exponential ($\chi^2/\text{ndf} = 1.3$) is shown by the solid line. The hatched area in the TOF spectrum (a) indicates the K^+ identified using the time calibration. The distributions are shifted arbitrarily.

momenta up to the 620 MeV/ c (for the maximal field $B = 1.57$ T in D2), which is a limit imposed by the number of available ANKE range telescopes. The details of the delayed veto technique are described in Sec. 3.2.2.

The distribution of the time difference measured between stop number thirteen and the corresponding veto counter is presented in Fig. 3.9a. Since the experimental data were collected with the veto trigger, there is no peak from the background particles, but a clear signal of the K^+ decay products with $\tau \sim 12.4$ ns is seen.

In addition to the time-of-flight, delayed veto and vertical angle criteria, the time calibration was used for further background suppression. In Fig. 3.9b the time-of-flight spectra measured with the delayed veto for telescope number thirteen are shown before and after applying cuts on the measured calibrated time-of-flight. The resulting distribution is almost unchanged, which implies that the efficiency of the time calibration is of the order of 98%.

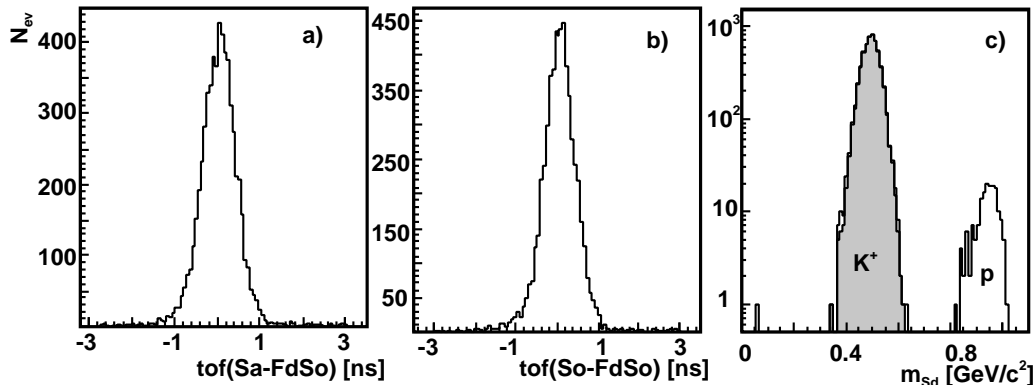


Figure 3.10: Identification of K^+p pairs in the delayed veto data at 2.7 GeV/c. The time difference between calibrated and measured, using trajectory time in Sa (a) and So (b) detectors and calibrated time in Fd detector. Mass of the particle whose track registered in the Sd detector (c). Hatched area shows the selected K^+p events.

3.3.2 Identification of protons in the Fd correlated with K^+

Calibrated time signals from Sd and Fd detector systems have been used to study K^+p coincidences (See Sec. 3.2.6). For the identification of the protons correlated with K^+ , cuts on the difference between the calibrated time differences measured in the Sd detector and the calibrated time difference for the proton in the Fd have been applied in addition to the cuts on the reconstructed Y coordinate of the track in Sd and Fd.

In Fig. 3.10 the difference between the calibrated time difference for the K^+ in Sa (a) and the calibrated time difference for the proton in Fd is shown; the same distribution for the So counter is shown in (b). A clear peak from the genuine K^+p correlations is seen. The mass of the particle whose track is registered in the side detector before and after (hatched histogram) applying all the cuts on the K^+p correlations is shown in Fig. 3.10c.

Cuts on the calibrated time differences measured in the forward and side detectors almost do not change the number of K^+p correlations in the delayed veto spectra. The typical K^+p missing mass spectra with the delayed veto and with all the cuts is presented in the Fig. 3.11b. The efficiency of the cuts, calculated as ratio of number of Λ and Σ^0 events before and after cuts on the calibrated time differences, is greater than 95%.

The identification of the K^+p pairs using only the time calibration in the side and forward detectors is shown in Fig. 3.12. Using all the criteria

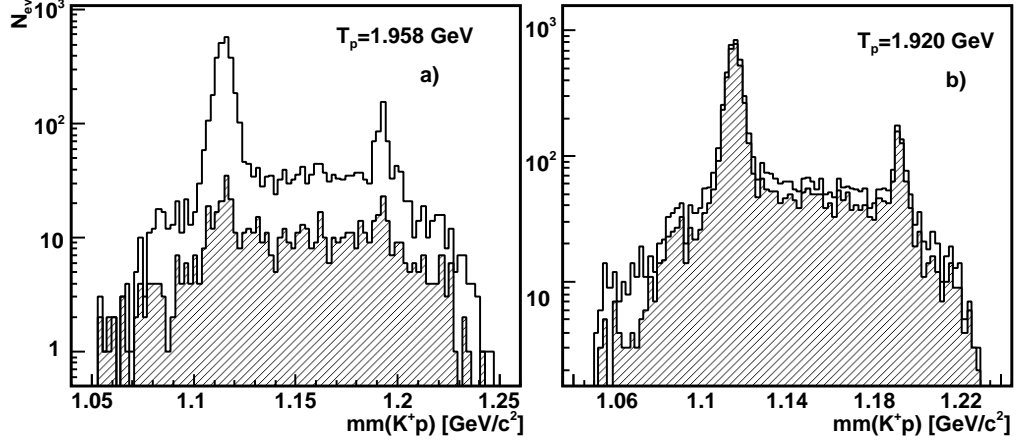


Figure 3.11: The K^+p missing mass spectra measured at 1.958 and 1.920 GeV (solid black lines). The hatched area in (a) indicates the K^+p missing mass evaluated for the detected protons with the 3σ cut on the reconstructed vertical coordinate of the proton. The K^+p missing mass spectra before and after (hatched histogram) applying cuts on the calibrated time-of-flight between Sd and Fd is shown in (b).

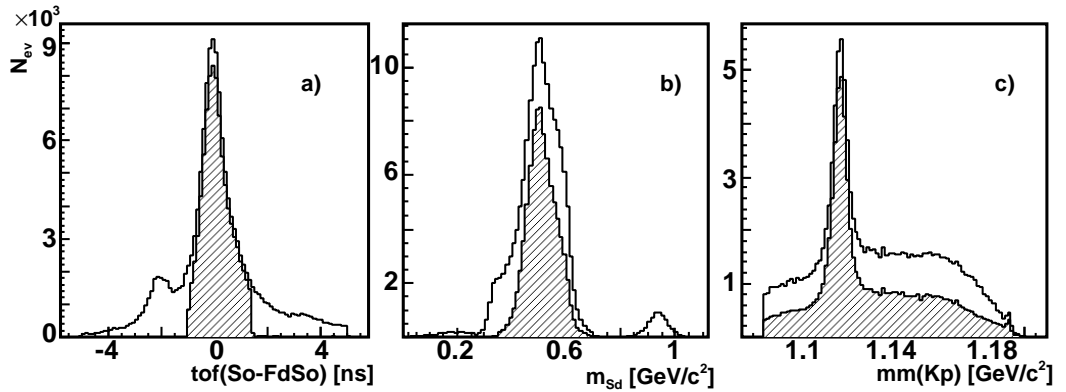


Figure 3.12: Identification of K^+p pairs without use of the delayed veto technique at 2.6 GeV/c. The difference between calibrated time and that estimated using the trajectories to the stop and forward detector is shown in (a). That calculated using track and calibrated time information and the mass of the particle detected in Sd detector is shown in (b). The measured K^+p missing mass spectra is in panel (c). The hatched areas in all the figures represent the events selected for the later analysis.

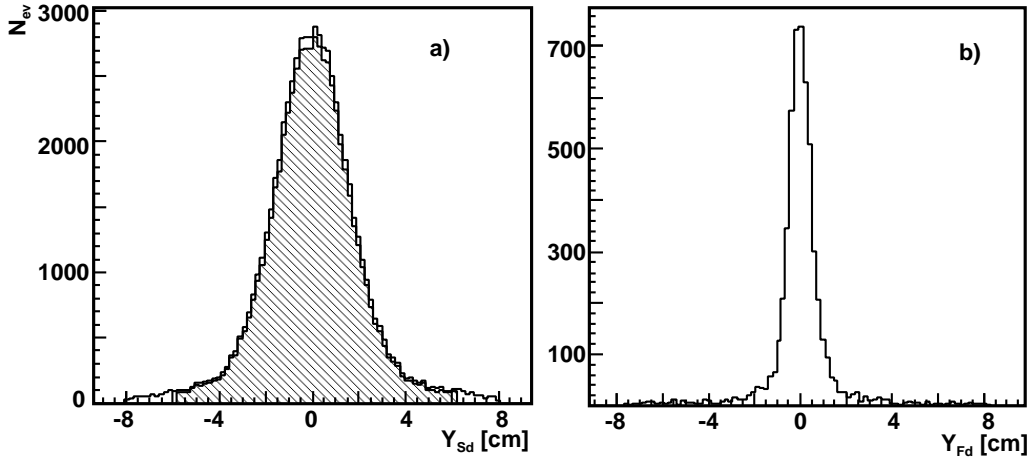


Figure 3.13: Vertical coordinate of the K^+ (a) and p (b) tracks reconstructed in the side and forward detectors respectively. The 3σ cut on the Y coordinate of the side track is shown by the hatched area. The data were collected at 1.920 GeV.

described above and applying 3σ cuts on the measured calibrated time differences, it is possible to reduce significantly the amount of background in the K^+p missing mass spectra. The measured K^+p missing mass spectra before and after applying all the cuts (hatched histogram) is shown in Fig 3.12c. Thus, it is in principle possible to identify hyperon production reactions using only information about times and tracks in the Sd and Fd detectors. The method thus developed has been used for the determination of the efficiency of the range telescopes described in Sec. 3.4.2.

The reconstructed Y coordinates of the K^+ and p tracks in Sd and Fd, respectively, are presented in Fig. 3.13. The protons in the K^+p pair can originate, not only from the reaction vertex, but also from the decays $\Lambda \rightarrow p\pi^-$ (BR 64%), $\Sigma \rightarrow \Lambda\gamma \rightarrow p\pi^-\gamma$ (BR 64%), and $\Sigma^+ \rightarrow p\pi^0$ (BR 52%) hyperons. Since the lifetime of the hyperons is significant (of the order of 1×10^{-10} s), these decay protons do not originate from a point-like vertex. This means that it is not possible to make cuts on the vertex of the proton track in the Fd detector. On the other hand, the ~ 0.52 cm (σ) resolution in the vertical coordinate reconstruction using the Fd detector allows one to remove 15 – 20% of the protons from the hyperon in the K^+p correlation by using a simple 3σ cut (See Fig. 3.11a) This criterion can be used for the analysis of differential observables in the hyperon reactions.

Since it is not possible to remove completely the contributions from the hyperon decay protons from the K^+p missing mass spectra, these were mod-

elled using phase space (See Sec. 4.3). Whereas a cut on Y coordinate of the p track in Fd was not applied, a 3σ cut on the vertical coordinate of the K^+ track has been introduced (Fig. 3.13 and Fig. 3.11b).

3.3.3 Identification of the particle in the Sd correlated with K^+

At the energies where measurements were performed, there is no other source of $K^+\pi^+$ correlations other than the $pp \rightarrow K^+n\Sigma^+$ reaction. Furthermore, there is no observable (such as a missing or invariant mass) where a signal from the reaction of interest can be identified without performing additional calculations. Therefore, in order to develop and cross check the methods for two-particle identification in the side detector, K^+p correlations have been used.

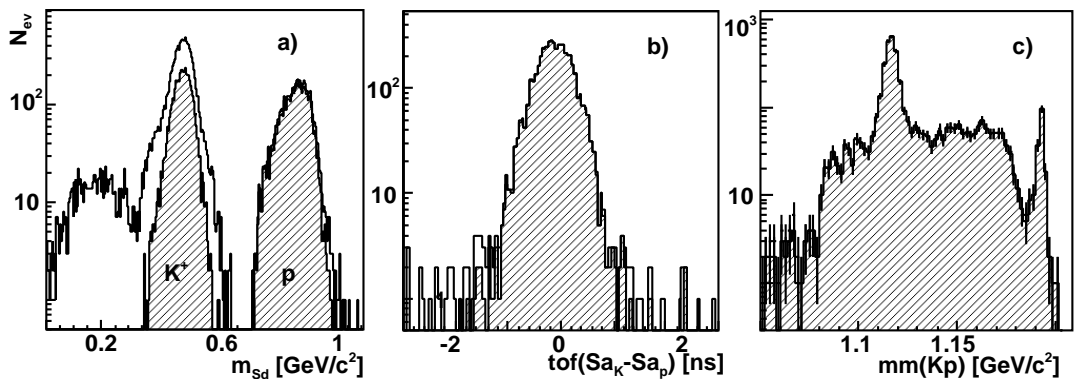


Figure 3.14: Identification of K^+p pairs in the Sd detector. (a) Calculated masses of all the particles detected in the Sd detector on a logarithmic scale. (b) The difference between the calibrated and estimated times, using trajectory length to the start counters, for two particles detected in the Sd. (c) The measured K^+p missing mass spectra. The hatched areas in all the figures represent events selected for later analysis. The experimental data were collected at 1.826 GeV.

For the identification of the two tracks in the side detector, information about each particle in the detector was analysed separately. The type of particle registered was determined using the mass reconstructed from the calibrated time and trajectory of the track. The masses of all the particles whose tracks were registered in the Sd detector is shown in Fig. 3.14. Three pronounced peaks are clearly seen coming from the π^+ , K^+ and p . In addition to the cuts on the mass of the particle selecting K^+ and p , an additional cut

on the calibrated time-of-flight between the proton and kaon in the Sa and So counters has been applied Fig. 3.14b. The efficiencies of these criteria were found by determining the number of Λ events in the final and initial K^+p missing mass spectra (See Fig. 3.14c). Using this method it is possible to identify genuine double track events in the Sd with an efficiency better than 95%.

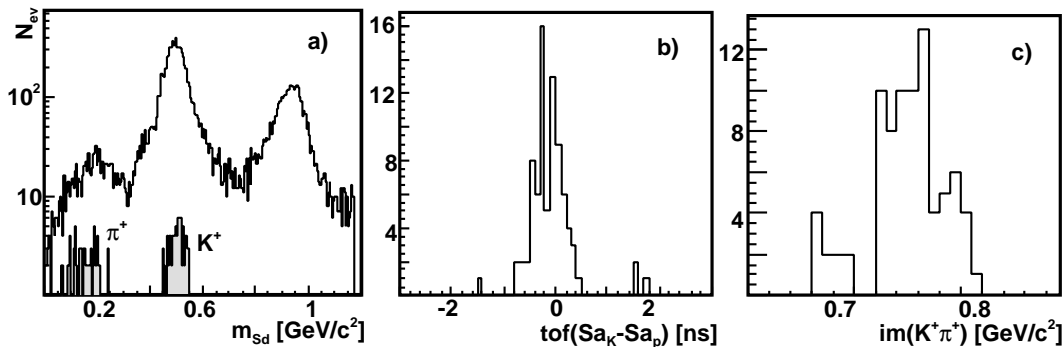


Figure 3.15: Identification of $K^+\pi^+$ pairs in the Sd detector. (a) Calculated mass of all the particles detected in the Sd detector on a logarithmic scale; the hatched area represents the events selected for later analysis. (b) Difference between the calibrated time and that estimated using the trajectories to the start counters for two particles detected in the Sd. (c) Measured $K^+\pi^+$ invariant mass spectra after making all the selections. The data were collected at 2.02 GeV.

The selection of the $K^+\pi^+$ pairs is shown in Fig. 3.15. The same cuts have been applied on the double time difference (Fig. 3.15b) as for the protons. The resulting invariant mass of the K^+ and π^+ is shown in Fig. 3.15c. The time calibration for the K^+ and π^+ tracks in Sd reduces the coincidence background significantly, which is of special importance for processes with low statistics, such as the $pp \rightarrow K^+n\Sigma^+$ reaction. It is in principle not possible to identify double tracks for events in the Sd where the same counter is hit because the information about the time of one of the particles will be lost already on the trigger level and events can be misidentified as random coincidences. The final number of the $K^+\pi^+$ events was therefore corrected for this effect using simulations (See Sec. 4.4).

3.4 Efficiencies

In order to extract total cross sections, the efficiencies of all the detection systems must be taken into account. Those of the scintillator counters were

of the order of 100% except for the thin start counters 1 – 3, which were excluded from the final analysis.

3.4.1 Efficiencies of the MWPCs

The efficiencies of the side MWPCs depend on the type and momentum of the particle. The chamber inefficiencies in the side detector were determined by the ratio of the number of particles of a certain type with a track traced to the counter to the total number of particles selected using only counter information. The efficiency of the side chambers depend on the stop counter number and vary in the range of 90 – 98% and 80 – 90% for the K^+ and π^+ , respectively.

The efficiencies of the chambers in the forward detector were determined using track information (See Ref [66]). In this analysis, each plane is divided into 20×20 squares and the efficiency in each square estimated using a track reconstructed without the information from this plane. In the final analysis, the efficiency for every track was determined using the efficiency map for all the planes previously calculated.

3.4.2 Efficiencies of the range telescopes

The efficiency of the range telescopes is limited by the principles of the method where the K^+ mesons are stopped in the second degrader and the decay products are registered in the veto counter. The stopped K^+ decay products are isotropically distributed in the laboratory system so that the efficiency is limited geometrically to $\approx 33\%$. Due to the relatively high background, it is very difficult to determine the telescope efficiency without the detection of an additional particle in one of the other systems.

An analysis of the K^+p coincidences detected in the Sd and Fd using dedicated trigger T_1 has been done in order to determine the telescope efficiency. The time calibration described in Sec. 3.2.6 was used for background suppression. In order to obtain sufficient statistics for this analysis, all the energies with the same pre-scaling factors in the K^+p coincidence trigger (T_1) have been summed. The resulting summed missing mass spectra and TOF spectra measured in telescope five, are presented in Fig. 3.16. The time-of-flight spectra measured for each telescope have been fitted with a Gaussian and a first order polynomial (See Fig. 3.16b). This approximation of background contribution in individual spectra is accurate to within $\sim 5\%$ and is the largest uncertainty in the determination of the telescope efficiency.

Unfortunately, the available statistics are not sufficient to determine the angular dependence of the telescope efficiency and so it is not possible to

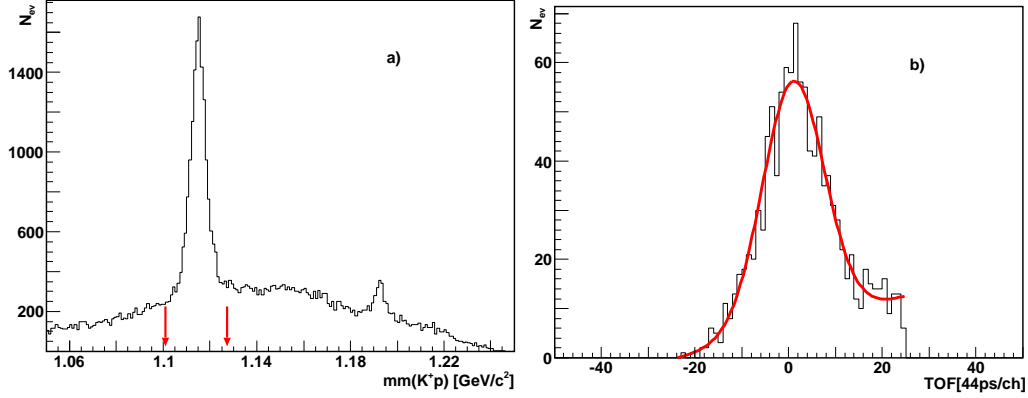


Figure 3.16: Telescope efficiency determination. (a) K^+p missing mass spectra integrated over $\vartheta_{K^+} < 12$ and $\vartheta_p < 8$, summed over three energies (1.775, 1.920 and 1.958 GeV). The arrows show the cuts on the missing mass applied for better K^+ selection. (b) Time-of-flight spectra measured in telescope number five fitted with a Gaussian and a first order polynomial.

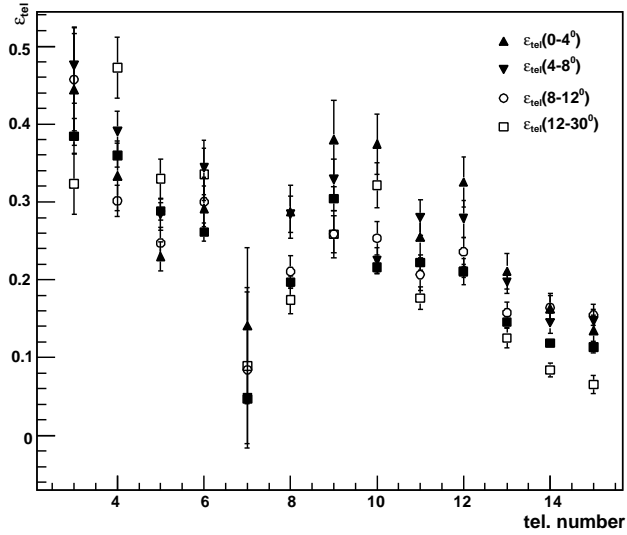


Figure 3.17: Telescope efficiencies determined using different cuts on the K^+ angle. Up triangles, down triangles, open circles and open squares corresponds to telescope efficiencies integrated over the angular ranges $0 - 4^\circ$, $4 - 8^\circ$, $8 - 12^\circ$ and $12 - 30^\circ$, respectively. All the numbers agree within error bars.

correct the angular spectra measured with delayed veto for this effect. In Fig. 3.17 the telescope efficiencies determined for the different angular cuts are presented. Within the statistical errors the numbers are in fair agreement. It is therefore concluded that the angular dependence of the telescope efficiency is weak and, for the later analysis, the efficiency integrated over $\vartheta_{K^+} < 12^\circ$ was used. The resulting telescope efficiencies given in Table. 3.4 as a function of counter number are compared to the standard values from Ref. [11]. The efficiency for telescope number seven deviates strongly from

p_{K^+} MeV/c	$\varepsilon_{\text{Sep07}}$	$\Delta_{\varepsilon_{\text{Sep07}}}$	$\varepsilon_{1.57T}$	$\Delta_{\varepsilon_{1.57T}}$
1	0.10	0.035	0.10	0.035
2	0.202	0.055	0.202	0.055
3	0.365	0.015	0.265	0.055
4	0.350	0.011	0.294	0.055
5	0.279	0.009	0.293	0.060
6	0.255	0.009	0.223	0.035
7	0.049	0.002	0.033	0.005
8	0.197	0.006	0.183	0.017
9	0.204	0.004	0.179	0.018
10	0.192	0.003	0.176	0.016
11	0.172	0.003	0.162	0.012
12	0.167	0.002	0.169	0.013
13	0.113	0.002	0.107	0.012
14	0.103	0.002	0.088	0.009
15	0.103	0.002	0.097	0.010

Table 3.4: Telescope efficiencies used in the analysis compared to the numbers given in Ref. [11]. The efficiencies were determined for the ANKE spectrometer with maximum magnetic field $B \approx 1.57$ T. In addition to the statistical errors shown, there is an additional 5% systematic error due the background subtraction procedure in the analysis.

that used in the previous experiments due to an inefficiency in the delayed veto trigger, which was overlooked during data taking.

3.5 Normalisation

In order to determine the absolute normalisation and hence a cross section, a luminosity L_{tot} has to be determined. In this work the normalisation

has been established using pp elastic scattering detected in the forward detector using a dedicated trigger. The luminosity integrated over time is given by the formula:

$$L_{\text{tot}} = N_{\text{tot}} \left/ \int_{\Omega_{\text{det}}} \frac{d\sigma}{d\Omega} d\Omega \right., \quad (3.3)$$

where N_{tot} is the number of events detected in the ANKE forward detector, $d\Omega_{\text{det}}$ the solid angle restricted by the detector acceptance, and $d\sigma/d\Omega$ the differential cross section of the reaction used for the normalisation. As a cross check, the luminosity has been determined for several runs using the Schottky method.

3.5.1 Proton-proton elastic scattering

Only standard cuts on the track in Fd were needed to identify pp elastic scattering. The ANKE forward detector has 100% acceptance for this reaction in the restricted angular range $\vartheta = 5 - 10^\circ$ and $|\phi| < 15^\circ$. The current solution of the biggest phase-shift database SAID has been used for the normalisation [73]. The precision of the cross sections obtained in this way in the energy range of interest is of the order of $\sim 5\%$.

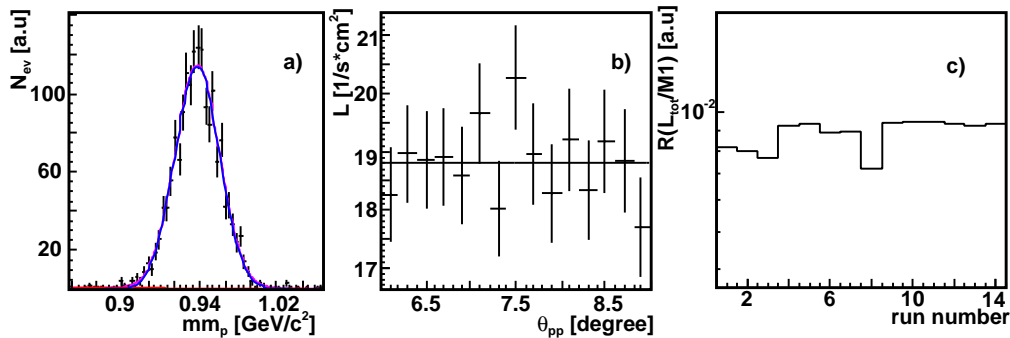


Figure 3.18: Luminosity determination. (a) Proton missing-mass spectra integrated over the angular bin $6.6 - 6.8^\circ$ measured at $2.546 \text{ GeV}/c$. (b) Angular dependence of the luminosity determined for the run 12720. (c) Ratio of the total luminosity to the rate of monitor number one shown on a logarithmic scale. Only runs selected for further analysis are shown.

A proton missing-mass spectrum corrected for the efficiencies measured at $2.806 \text{ GeV}/c$ is presented in Fig. 3.18. The clear peak from pp elastic events with moderate background was fitted with a Gaussian plus a straight line. The angular dependence of the luminosity extracted from the data fitted by

the straight line is presented in Fig. 3.18b. In order to estimate systematic error of the normalisation, the error of the individual bins L_{tot} in the spectra was adjusted to give a $\chi^2 \sim 1$. This results in additional 3% error in the luminosity determination.

The luminosity was determined on a run-by-run basis and cross checked using the side monitors. The stability of the DAQ and the dependence of the luminosity determination on the run number is presented in Fig. 3.18c as a ratio of determined luminosity to the number of registered scaler signals. Runs with strong deviation from the average value were excluded from the final analysis, since data taking conditions were unstable in these runs.

The analysis of the pp elastic events registered in forward detector results in a luminosity determination with a precision of $\sim 7\%$.

3.5.2 The Schottky method

Simultaneous measurement of the Schottky spectra and beam current can result in measurements of the absolute luminosity of a stored uncooled beam [74]. The average density of the target region that interacted with the beam can be written as:

$$N_{\text{av}} = \frac{1 + \gamma}{\gamma} \frac{1}{\eta} \frac{1}{dE/dx} \frac{T_0}{m} \frac{df}{f_0^2 dt}, \quad (3.4)$$

where γ is the Lorentz factor of the beam particle, dE/dx is the stopping power of the proton (taken from Ref. [75]), m the proton mass, T_0 the kinetic energy of the beam, f_0 the revolution frequency of the machine, df/dt the change of the machine frequency during one cycle due to the beam-target electromagnetic interaction, and η the so-called frequency slip factor.

The η parameter can be determined using measurements of the momentum compaction factor $\alpha = 1/\gamma^2 - \eta$. The α is constant for a given lattice settings and can be measured by changing the magnetic field in the bending magnets by a few parts per thousand and using

$$\frac{\Delta f}{f} = \alpha \frac{\Delta B}{B}. \quad (3.5)$$

The df/dt is measured using the Schottky spectrum that is stored ten times per cycle. An example of one Schottky spectrum measured at 1.826 GeV is presented in Fig. 3.19a. Measurements of the beam current are done using a precision beam current transformer (BCT), calibrated with an accuracy of 0.01 %. The BCT current was continuously recorded by the ANKE DAQ.

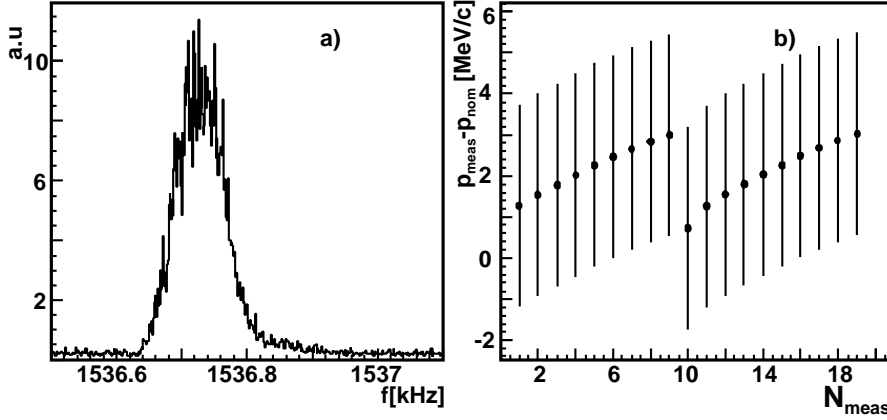


Figure 3.19: (a) Schottky spectrum measured at 2.6 GeV/c. (b) Difference between measured and nominal beam momentum measured at 2.6 GeV/c. The error bars shows precision in knowledge of the COSY trajectory length.

Monitoring the frequency shift and the average beam current, the luminosity integrated over the cycle can be determined. In addition to measurement uncertainties (frequency shift and BCT measurements), systematic errors due to the η parameter determination and residual gas effects have to be taken into account in the analysis. The principal limitation of the method is connected with the frequency slip parameter η , which depends on the beam energy and cannot be determined with good precision for proton beam energies between 1 and 1.6 GeV [74].

Careful monitoring of the Schottky spectra not only allows the absolute luminosity determination with a precision of the order of $\sim 7\%$, but also permits one to control momentum changes of the uncooled beam during the cycle. This is especially important for the close-to-threshold measurements, since the total cross section can change significantly with a small change of the excess energy. One can determine the beam momentum in the experiment by using the knowledge about the COSY beam trajectory and monitoring the beam frequency with the Schottky spectra, .

The length of the COSY beam trajectory [76] L_{cosy} depends on the ANKE deflection angle α_{anke} and can be written as:

$$L_{\text{cosy}} = 183.473 + (5214(1/\cos(\alpha_{\text{anke}}) - 1) - 1549.2(\tan(\alpha_{\text{anke}})/\alpha_{\text{anke}} - 1))/1000. \quad (3.6)$$

The relativistic speed β in this case can be determined as

$$\beta = L_{\text{cosy}} F 1000/c, \quad (3.7)$$

where F is the frequency of the beam determined from the Schottky spec-

tra and c is the speed of light. The beam momentum, $p = m\beta c/\sqrt{1 - \beta^2}$, can therefore be controlled for every cycle. The uncertainty in the momentum determination is dominated by the ~ 1.8 cm precision in the trajectory length. The difference between the nominal beam momentum 2.6 GeV/ c and that calculated from the Schottky spectra is shown in the Fig. 3.19b. This analysis of the Schottky spectra leads to the uncertainty in the excess energy determination discussed in Sec. 4.5.

Chapter 4

Extraction of the cross sections

In order to obtain values of the cross sections, the numbers of identified events have to be corrected for the luminosity, detector efficiencies, and acceptances. The particle identification and efficiency corrections have been described in Sec. 3.3 and Sec. 3.4. The GEANT4 [77] simulation package, which uses the same geometrical setup of detectors as the analysis software, has been used for the acceptance calculation [78]. The total and differential acceptances were estimated within several phenomenological models (see Sec. 4.1) and compared with the experimental data. The total cross sections obtained are discussed in Sec. 4.5.

4.1 Phenomenological models used in the analysis

Several phenomenological models have been considered for the analysis of the experimental data. The world data on the energy dependence of the Σ^0 hyperon total production cross section seem to follow phase space [31] with a constant matrix element. Therefore simple three-body phase space has been used for the description of the experimental data and total acceptance determination. Data on the Σ^+ hyperon production are very scarce and, by analogy with the Σ^0 case, a simple phase space has also been used here as well.

Several models have been considered for the $pp \rightarrow K^+ p \Lambda$ reaction:

1. Model 0: simple three-body phase space.
2. Model 1: model 0 corrected for the $p\Lambda$ FSI taken from Ref. [29].

Reaction	T_{thr} GeV	Hyperon GeV/ c^2	BR(K^+p) %	BR($K^+\pi^+$) %
$pp \rightarrow K^+p\Lambda$	1.582	$\Lambda(1.116)$	63.9	—
$pp \rightarrow K^+p\Sigma^0$	1.794	$\Sigma^0(1.193)$	63.9	—
$pp \rightarrow K^+n\Sigma^+$	1.789	$\Sigma^+(1.189)$	51.57	48.31

Table 4.1: Parameters of the reaction channels used in the analysis [47].

3. Model 2: model 1 but assuming that the production goes via the $N^*(1650)$ resonance with parameters taken from Ref. [6].
4. Model 3: model 2 corrected for the kaon angular spectra, determined using data measured with the COSY-TOF spectrometer (See Table 4.2).
5. Model 4: model 2 corrected for the proton angular spectra, determined using data measured with the COSY-TOF spectrometer (See Table 4.2).
6. Model 5: model 2 corrected for the proton and kaon angular spectra, determined using data measured with the COSY-TOF spectrometer (See Table 4.2).

The $p\Lambda$ FSI is parameterised using the Jost function approach:

$$|A_{\Lambda p}| = \frac{q^2 + \alpha^2}{q^2 + \beta^2}, \quad (4.1)$$

where the momentum q is given by

$$q = \frac{\lambda^{1/2}(S_{\Lambda p}, m_{\Lambda}^2, m_p^2)}{2\sqrt{S_{\Lambda p}}}, \quad (4.2)$$

where $\lambda(x, y, z) = (x - y - z)^2 - 4yz$, $S_{\Lambda p}$ is the square of the total energy in Λp system, and α and β the parameters of the final state interaction, taken from Ref. [29]. All the parameters of the models used in the analysis of the Λ production reaction are presented in Table 4.2.

Following the analysis in Ref. [33], the proton and kaon angular spectra used for the models were parameterised as

$$\frac{d\sigma}{d\Omega}(\vartheta) = a_0 P_0(\cos \vartheta) + a_2 P_2(\cos \vartheta) + a_4 P_4(\cos \vartheta) + a_6 P_6(\cos \vartheta), \quad (4.3)$$

where the values of the a_n are given in Table 4.2, and the P_n are Legendre polynomials. The parameters were determined using polynomial fits to the

T_p GeV	a_0^P	a_2^P	a_4^P	a_6^P	a_0^K	a_2^K	a_4^K	α MeV/c	β MeV/c
1.775	0.40	0.16	0	0	0.43	0.21	0	-72.3	212.7
1.826	0.62	0.20	0	0	0.66	0.42	0		
1.920	0.85	0.46	0.08	0	0.85	0.38	0.02		
1.958	0.92	0.69	0.24	0	0.93	0.30	0.07		
2.020	1.16	1.10	0.46	0.05	1.15	0.40	0.11		

Table 4.2: Parameters of the Λ hyperon production models used in the analysis. The a_n are the parameters of the partial wave analysis of the proton and kaon angular cross sections in CM system used in the analysis. The α and β are the parameters of the $p\Lambda$ FSI taken from Ref. [29].

angular spectra measured in COSY-TOF experiments at different energies. For the details of their determination see Sec. A. All the six models of Λ production were only used for the analysis of the inclusive spectra. It was found that the inclusion of the K^+ angular spectra into the analysis changes the momentum spectra in an unacceptable way and contradicts all other experimental data. Therefore, only models 0, 1, 4 and 5 have been used for the estimation of the Λ total cross section.

4.2 Inclusive K^+ spectra

The only possibility to measure K^+ inclusive spectra at ANKE is through the use of the delayed veto technique (see Sec. 3.2.2). In this case the double differential cross section for K^+ production can be evaluated for every momentum bin using:

$$\frac{d^2\sigma_{K^+}}{d\Omega dp}(T_p) = \frac{N_{K^+}}{\Delta p \Delta \Omega} \frac{1}{L_{K^+} \varepsilon_{K^+}}, \quad (4.4)$$

where N_{K^+} is the number of identified K^+ events in a certain telescope, Δp and $\Delta \Omega$ are the momentum and solid angle integration regions, L_{K^+} the luminosity, and ε_{K^+} the efficiency of K^+ identification, which is calculated using:

$$\varepsilon_{K^+} = \varepsilon_{\text{telescope}} \times \varepsilon_{\text{scint}} \times \varepsilon_{\text{MWPC}} \times \varepsilon_{\text{accep}}. \quad (4.5)$$

The telescope $\varepsilon_{\text{telescope}}$, scintillator counters $\varepsilon_{\text{scint}}$ and multi-wire proportional chamber $\varepsilon_{\text{MWPC}}$ efficiencies are described in details in Sec. 3.4. In the data analysis the same set (see Table 3.4) of telescope efficiencies has always been used; thus it is assumed that a telescope efficiency does not depend

on the ϑ_{K^+} integration region. The acceptance correction factor $\varepsilon_{\text{accep}}$ for the inclusive spectra has been estimated using a GEANT4 based simulation package [78]. The probability of K^+ decay in the flight between the start and stop counters was included into the common acceptance correction factor. The same start-stop combinations and neighbouring analysis procedures have been used for the analysis of experimental data and simulations (See Sec. 3.2.4).

Double differential cross section for inclusive K^+ production, integrated over $\vartheta < 4^\circ$, measured at five energies are compared to simulations carried out within six models in Fig. 4.1. The sum of three-body phase space distributions normalised to the total cross sections of Λ , Σ^0 and Σ^+ production (Model 0), and assuming that $\sigma_{\Sigma^0} = \sigma_{\Sigma^+}$, clearly overestimates experimental data. The implementation of the $p\Lambda$ final state interaction from Ref. [29] or the resonance $N^*(1650)$ (Model 1 and Model 2, respectively) gives almost identical results, which are in better agreement with the experimental data. Model 4, which gives better agreement between calculations and experimental data, was used for the analysis of the angular dependence of the K^+ production double differential cross sections. Calculations within Models 3 and 5, which have an anisotropic K^+ angular spectra, show a strong dip in the K^+ momentum spectra. This has never been observed in any ANKE experimental data and so these models were omitted from the later analysis. It should be noted in this respect that the COSY-TOF angular distributions are global ones that do not take the ANKE K^+ momentum cuts into account.

Double differential cross sections measured at five energies and integrated over different $\Delta\vartheta_{K^+}$ are presented in Fig. 4.2. The experimental data are compared to the calculations using simple phase space for the Σ channels and different models for the Λ (see Sec. 4.1). Model 4 has been used for the simulation of Λ contribution to the K^+ inclusive spectra, except calculation for 1.775 and 1.826 GeV, where Model 1 has been used. The simulations are normalised to the total cross sections extracted from the K^+p correlation data discussed in Sec. 4.3. The contributions of the individual reaction channels are shown by lines of different colours. The black line represents the contribution of Λ production, the magenta line Σ^0 production on top of the Λ , and the thick blue line is the sum of all the production channels normalised to the total cross sections from Sec. 4.5. The experimental data and simulations for all the energies and all the $\Delta\vartheta_K$ are in mutual agreement.

The double differential cross sections integrated over different $\Delta\vartheta_{K^+}$ can be transformed into differential cross sections integrated over the ANKE

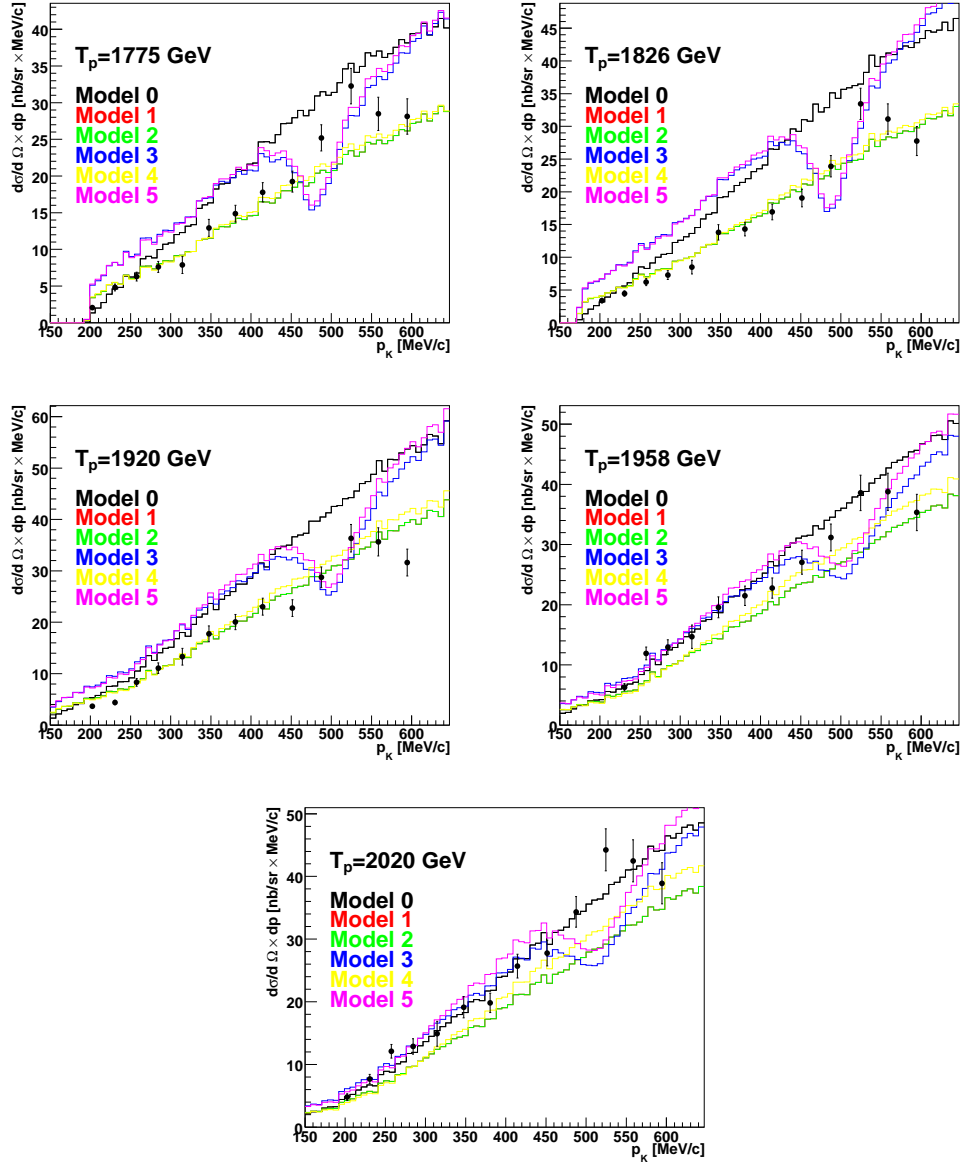


Figure 4.1: The K^+ double differential cross sections measured at five energies and integrated over kaon angles $\vartheta < 4^\circ$ in comparison to the predictions of six different models. The error bars do not include systematic uncertainty due to normalisation.

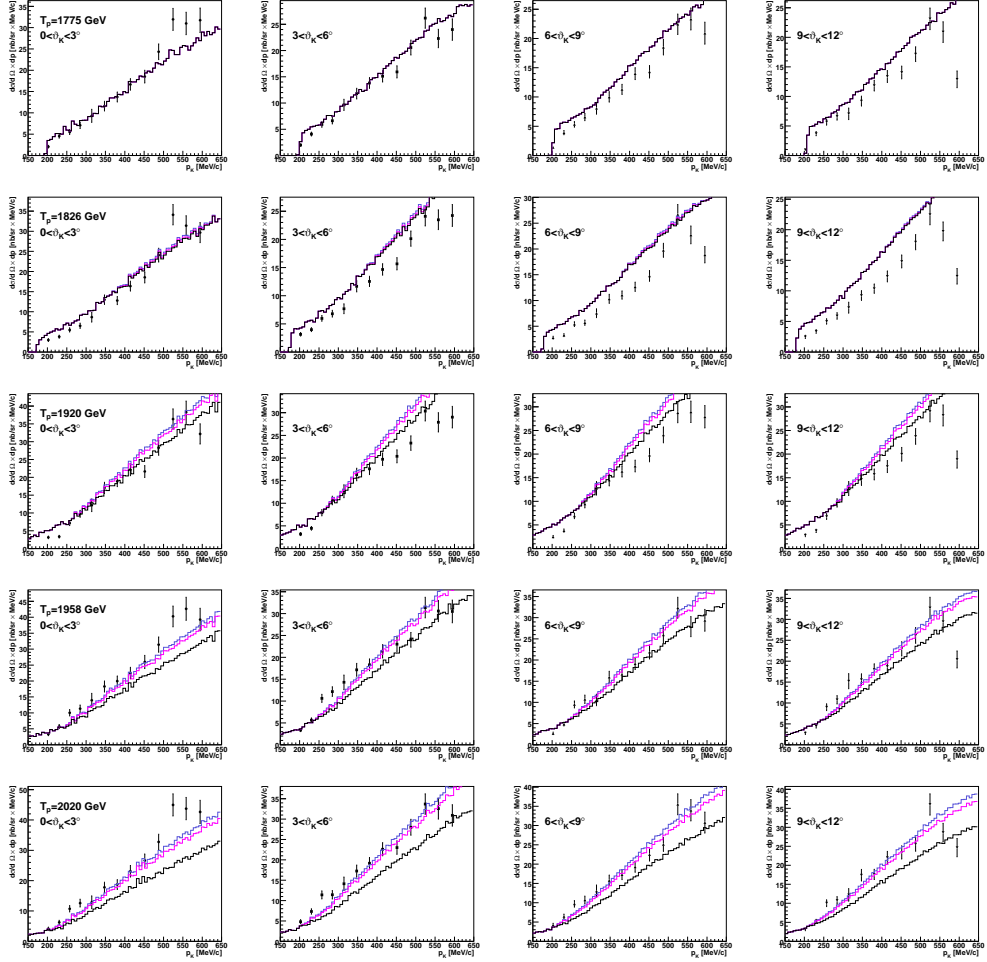


Figure 4.2: Inclusive K^+ production double differential cross sections measured at five different energies and integrated over different $\Delta\vartheta_K$ in comparison to the calculations. The black lines show the contribution from the Λ reaction channel calculated within Model 4, the magenta lines show the contribution from Σ^0 reaction channel on the top of Λ , and the sums of all three Λ , Σ^0 and Σ^+ reaction channels are shown by the thick blue lines. The error bars do not include systematic uncertainties from the normalisation to pp elastic data.

momentum range using Eq. (4.6):

$$\left. \frac{d\sigma}{d\Omega} \right|_{p_i \pm 10 \text{ MeV}/c} = \sum_{i=3}^{15} \frac{N_{K^+}^i}{\Delta\Omega L_{K^+} \varepsilon_{K^+}^i}. \quad (4.6)$$

The inclusive differential cross sections measured within the ANKE momentum range are presented in Fig. 4.3 and compared there to simulations. Any small residual differences between the data and models is probably due to the angular dependence of the telescope efficiency, which could not be taken into account due to having insufficient statistics (see Sec. 3.4.2).

Measured inclusive double differential cross sections are well described by simulations normalised to the total cross sections extracted from the correlation analysis discussed in Secs. 4.3 and 4.4.

4.3 Analysis of the K^+p correlation events

The K^+p missing mass spectra measured in the Fd detector have been used for the extraction of the total cross sections of the Λ and Σ^0 production channels. The number of the Λ and Σ^0 events N_{ev} in the spectra was estimated using fits of the simulations to these missing mass spectra. The total cross section was estimated as follows:

$$\sigma_{\text{total}} = \frac{N_{\text{ev}}}{L_{\text{total}} \varepsilon_{\text{summ}}}, \quad (4.7)$$

where L_{total} is the total luminosity, $\varepsilon_{\text{summ}}$ the efficiency which includes all the detector efficiencies, total acceptance calculated within a certain model, the in-flight K^+ decay correction, and branching ratio for the Σ^+ total cross section estimation.

Four different models (0, 1, 4, 5) have been considered for the simulations of the missing mass spectra for K^+p correlation events. The details of the phenomenological models used are discussed in Sec. 4.1. Included in the simulations are the decays of the hyperons $\Lambda \rightarrow p\pi^-$, $\Sigma^0 \rightarrow \Lambda\gamma \rightarrow p\pi^-\gamma$ and $\Sigma^+ \rightarrow p\pi^0$, assuming simple phase space and the corresponding branching ratios. The parameters of the models and branching ratios for the different reaction channels are listed in Tables 4.1 and 4.2.

The K^+p missing mass spectra measured in the Fd and integrated over $\vartheta_K < 12^\circ$ and $\vartheta_P < 8^\circ$ are shown in Fig. 4.4. The experimental data were fitted using simulations for all the channels. Individual contributions from the Λ , Σ^0 , and Σ^+ decay protons, normalised to the numbers from Table 4.3 with corresponding branching ratios, are shown by the blue, magenta and

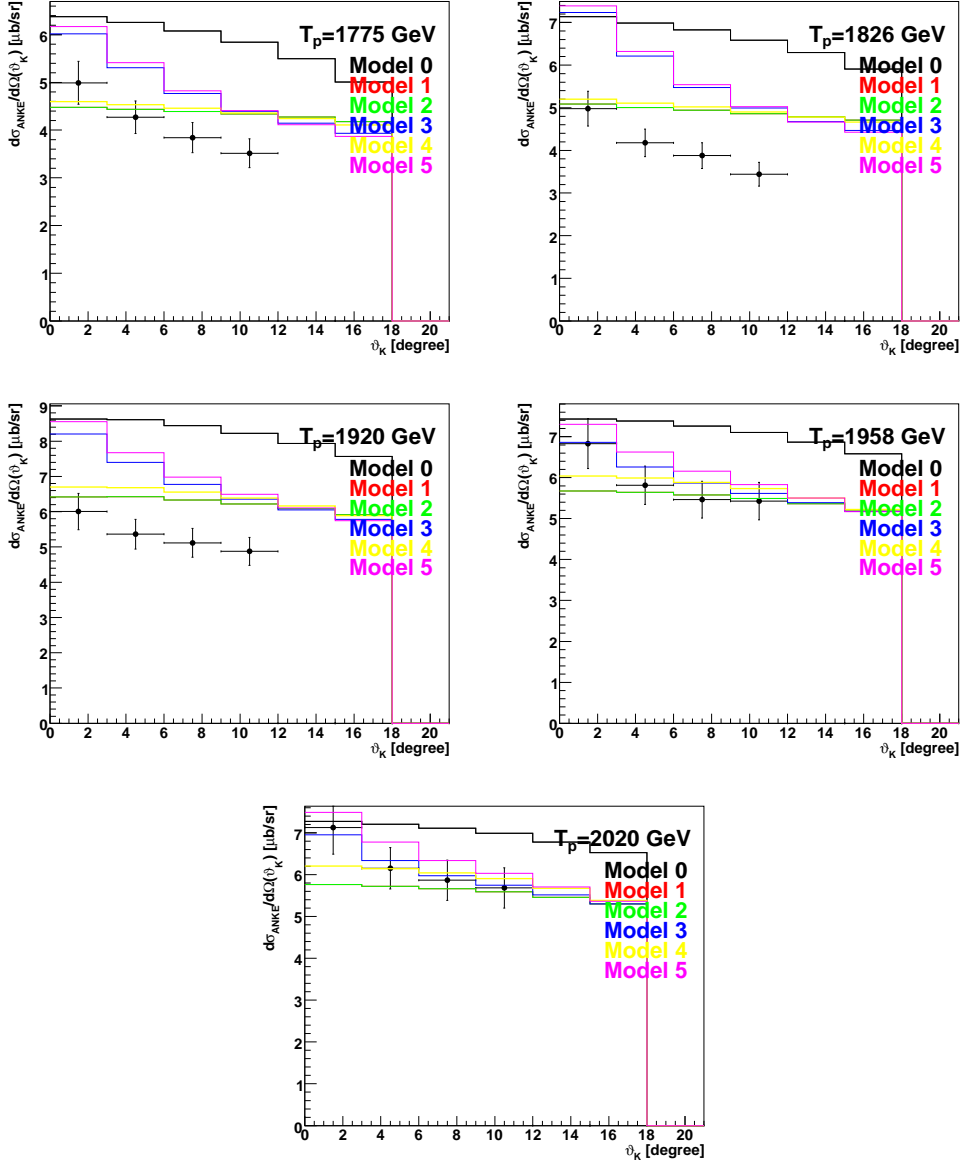


Figure 4.3: The K^+ angular spectra measured within the ANKE acceptance in comparison to different models. The error bars do not include systematic uncertainties due to normalisation.

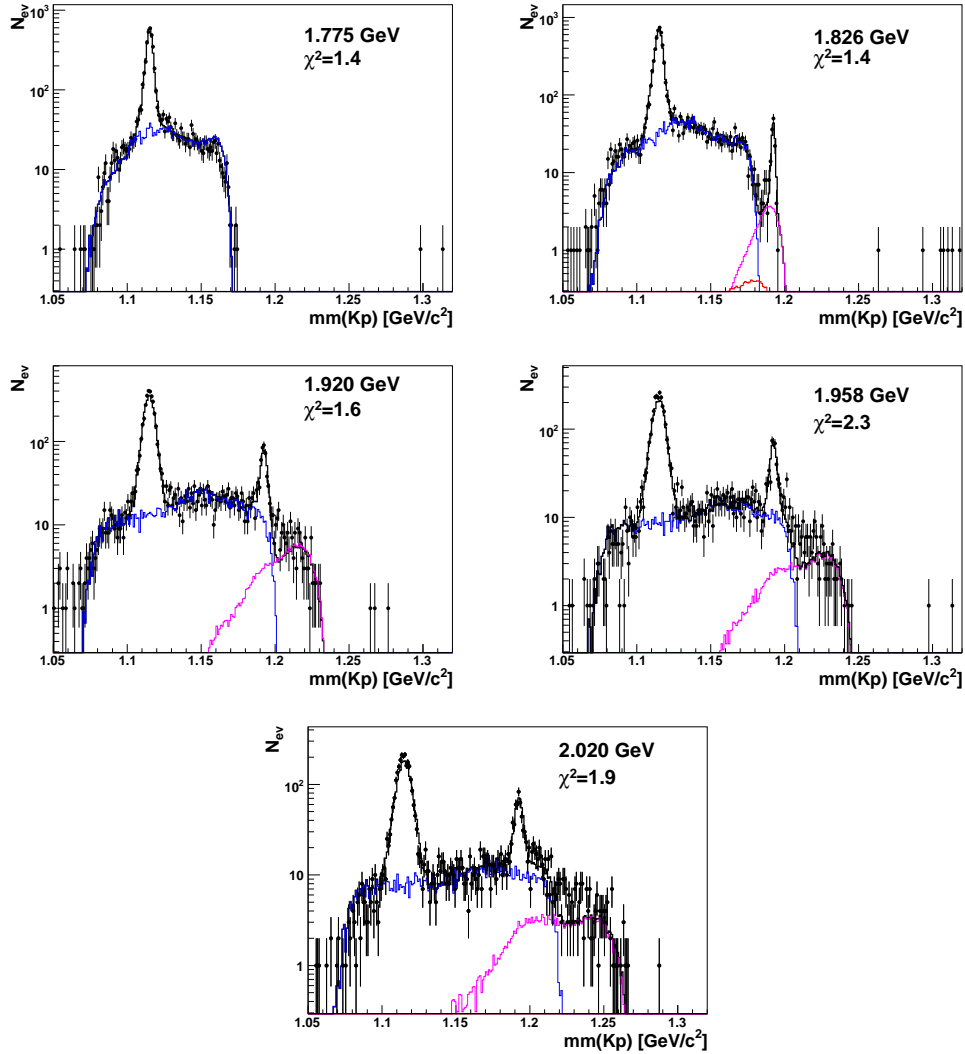


Figure 4.4: The K^+p missing mass spectra measured in the Fd detector at five different energies in comparison to simulations. The missing mass spectra are integrated over angles $\vartheta_K < 12^\circ$ and $\vartheta_p < 8^\circ$. Contributions from the Λ , Σ^0 and Σ^+ decays to the K^+p missing mass spectra, normalised to the number of events from Tab. 4.3, are shown by the blue, magenta and red lines, respectively.

T_p GeV	Model	χ_{Hyp}^2	χ_{Σ}^2	N_{ev}^{Λ}	$N_{\text{ev}}^{\Sigma^0}$	$N_{\text{ev}}^{\Sigma^+}$
1.775	0	3.06	0.00	2870 ± 40	0 ± 0	0 ± 0
	1	1.42	0.00	2969 ± 50	0 ± 0	0 ± 0
	4	1.46	0.00	2968 ± 37	0 ± 0	0 ± 0
	5	1.20	0.00	2982 ± 44	0 ± 0	0 ± 0
1.826	0	1.96	1.77	4355 ± 52	105 ± 9	-35 ± 25
	1	1.41	1.37	4396 ± 56	107 ± 9	32 ± 25
	4	1.38	1.35	4399 ± 54	107 ± 8	24 ± 25
	5	1.80	1.61	4362 ± 55	111 ± 9	99 ± 25
1.920	0	1.72	1.88	2992 ± 44	330 ± 16	-22 ± 20
	1	1.78	1.93	2980 ± 44	336 ± 16	-25 ± 20
	4	1.62	1.74	3006 ± 40	327 ± 16	-19 ± 20
	5	2.05	2.25	2938 ± 45	352 ± 16	-33 ± 20
1.958	0	2.18	2.06	2064 ± 35	297 ± 16	13 ± 19
	1	2.17	2.05	2061 ± 37	301 ± 16	11 ± 19
	4	2.29	2.06	2058 ± 35	291 ± 15	18 ± 19
	5	2.27	2.24	2034 ± 35	316 ± 15	4 ± 19
2.020	0	1.90	1.76	1945 ± 36	396 ± 19	22 ± 20
	1	1.92	1.78	1939 ± 36	400 ± 19	21 ± 20
	4	1.91	1.71	1954 ± 36	387 ± 18	27 ± 20
	5	2.07	1.94	1907 ± 36	414 ± 18	20 ± 20

Table 4.3: Number of identified events N_{ev} for the Λ , Σ^0 and Σ^+ production channels and parameters of the fit of the K^+p missing mass spectra measured in the Fd. The kaon and proton angles are integrated over 12° and 8° , respectively. The χ_{Hyp}^2 quoted is the value from the fit of the measured K^+p missing mass spectra by simulations of only the Λ and Σ^0 channels. The χ_{Σ}^2 is value from the fit of the experimental spectra by simulations in the region of Σ^+ contribution assuming that the Λ and Σ^0 contributions are fixed and varying only that of the Σ^+ .

red lines, respectively. The fitting of the missing mass spectra was done in two stages. In the first step the numbers of Λ and Σ^0 events were fixed, dominantly by the two clear peaks. In the second step, only the number of Σ^+ events in the spectra was fitted, minimising χ^2_{Σ} in the region of the Σ^+ contribution to the spectra. The results of the fits of the K^+p missing mass spectra are presented in Table 4.3.

The numbers of Λ and Σ^0 events are very well fixed by the peaks observed in the missing mass spectra at all the energies and they are almost independent of the model selected. In contrast to this, the Σ^+ contribution overlaps with those from other hyperon decays and cannot be isolated in some part of the spectra, especially at the lower energies. Therefore, the number of Σ^+ events extracted from the spectra depends on the models used for the Λ and Σ^0 and even go to the negative values for some energies (see Tab. 4.3). It is therefore not possible to calculate the systematic error of the Σ^+ total cross section using the number of events extracted from the K^+p missing mass spectra.

For the final analysis of the experimental data measured at $T_p = 1.775$ and 1.826 model 1 has been used for the Λ production channel, while for other energies model 4 has been employed. The final numbers of events extracted from the spectra and the corresponding values of χ^2 for the description of the full spectra are presented in Table 4.4.

T_p GeV	χ^2_{tot}	N_{ev}^{Λ}	$N_{\text{ev}}^{\Sigma^0}$	$N_{\text{ev}}^{\Sigma^+}$
1.775	1.42	2969 ± 50	0 ± 0	0 ± 0
1.826	1.40	4396 ± 56	107 ± 9	32 ± 25
1.920	1.61	3006 ± 40	327 ± 16	-19 ± 20
1.958	2.29	2058 ± 35	291 ± 15	18 ± 19
2.020	1.90	1954 ± 36	387 ± 18	27 ± 20

Table 4.4: Numbers of identified N_{ev} for the Λ , Σ^0 and Σ^+ production channels and the parameters of the fit of K^+p missing mass spectra by the simulations. The kaon and proton angles are integrated over 12° and 8° respectively.

The total acceptance for all the reaction channels was calculated in order to extract the total cross sections. For the Λ channel the total acceptance within four different models has been estimated and the resulting total cross sections for both Λ and Σ^0 production are presented in Table 4.5.

The values of the total cross sections for Λ production change significantly, depending on the model selected. This effect is especially important at high energies, where ANKE covers only a small part of the total phase space.

T_p GeV	Λ						Σ^0		
	σ_{WD}	σ_{M0}	σ_{M1}	σ_{M4}	σ_{M5}	Δ_{stat}	σ_{WD}	σ_{M0}	Δ_{stat}
	μb					%	μb		%
1.775	5.7	5.8	6.1	4.7	3.7	1.4	0.000	0.000	0.0
1.826	7.9	8.0	9.2	7.4	5.5	1.2	0.020	0.004	8.3
1.920	12.2	20.1	26.1	16.1	15.3	1.5	0.300	0.238	4.9
1.958	14.1	24.9	32.6	16.9	15.7	1.7	0.498	0.512	5.3
2.020	17.1	33.7	43.9	18.0	16.5	1.9	0.915	1.296	4.7

Table 4.5: Total cross sections for Λ and Σ^0 production evaluated within different models.

However, at $T_p = 1.775$ and 1.826 GeV the acceptance is sufficiently large to reconstruct the Λ total cross section with a precision of $\sim 10 - 15\%$, which is comparable to the data obtained in other experiments.

Due to the much smaller excess energies for the Σ^0 production channel, the total acceptance is of the order of $\sim 1\%$ so that the values obtained for the Σ^0 total total cross sections are more reliable. However, the Σ^0 total cross section at 1.826 GeV is much lower than the world data, probably due to an inefficiency in the K^+p correlation trigger at this particular energy (see Sec. 2.4).

The analysis of the K^+p correlation missing mass spectra allows one to estimate the total cross sections for the Λ and Σ^0 reaction channels within the models considered. Unfortunately, due to the overlap of the contributions from the decays of different hyperons, it is not possible to estimate with great confidence the total cross section of Σ^+ production using K^+p correlation data. Nevertheless, the analysis of the measured missing mass spectra completely excludes the possibility that the Σ^+ total cross section is as high as that reported in Ref. [48].

4.4 Analysis of the $K^+\pi^+$ correlation events

The obvious way to study the $pp \rightarrow K^+n\Sigma^+$ reaction is by measuring the K^+n missing mass and identifying the Σ^+ peak [48]. This is not possible at ANKE since there is no neutron detector installed. However, below the threshold for the $pp \rightarrow nK^+\Lambda\pi^+$ reaction (1.975 GeV) there is no other source of $K^+\pi^+$ correlations other than the $pp \rightarrow K^+n\Sigma^+$ reaction. From bubble-chamber experiments [17] it is known that the $pp \rightarrow nK^+\Lambda\pi^+$ reaction total cross section is relatively small at the much higher energy of

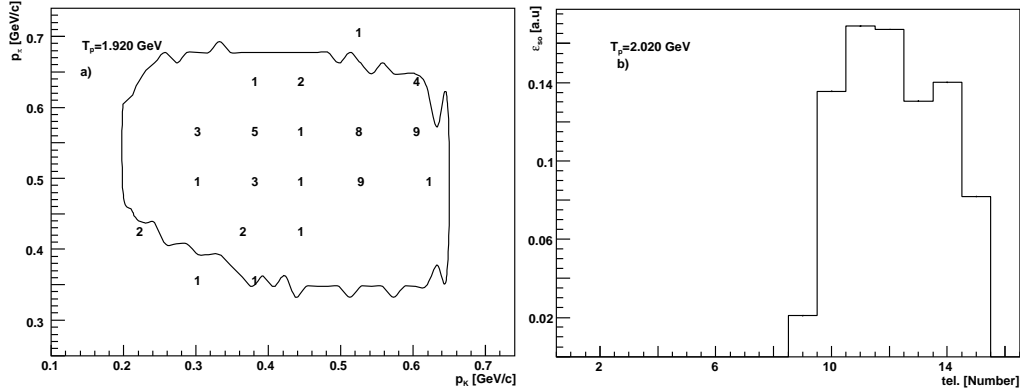


Figure 4.5: a) Two-dimensional $K^+\pi^+$ momentum distribution measured at 1.826 GeV in comparison to simulations. b) Analysis inefficiencies for tracks detected in the same stop counter calculated for $T_p = 2.020$ GeV.

2.88 GeV (see Sec. 1.2.6). Our studies of the $K^+\pi^+$ correlations performed at 2.16 GeV [28] confirm that the cross section for $\Lambda\pi^0$ production is low. Furthermore, the π^+ momentum spectra from the reaction with $\Lambda\pi^+$ in the final state and that from the $\Sigma^+ \rightarrow n\pi^+$ decay are very different and can be easily separated using simple kinematical constraints. Thus, the detection of K^+ and π^+ in coincidence in the final state allows one to identify the Σ^+ reaction channel without the use of a sophisticated neutron detection system.

Independent of the beam energy, the numbers of $K^+\pi^+$ coincidences detected at ANKE are relatively small. After applying all the selection criteria described in Sec. 3.3.3, a contribution from accidental coincidences is still seen in the spectra. The K^+ and π^+ momentum and invariant mass spectra collected at 1.775 GeV, after applying all the selection criteria are shown in the upper panel of Fig. 4.6. Data collected below the threshold of the reaction and simulations have been used to subtract this background from the final momentum and invariant mass spectra.

The two-dimensional kinematically allowed regions of K^+ and π^+ momenta have been determined using simulations. A comparison of the two-dimensional $K^+\pi^+$ momentum spectra detected at $T_p = 1.920$ GeV spectra with simulations is shown in Fig. 4.5a.

The distribution of background events was evaluated by applying two-dimensional cuts, determined for the selected energy, to the data collected at $T_p = 1.775$ GeV. After the normalisation to the ratio of the luminosities, the background distributions were subtracted from the corresponding K^+ and π^+ momentum and invariant mass spectra.

Even in principle it is not possible to measure the time when the K^+

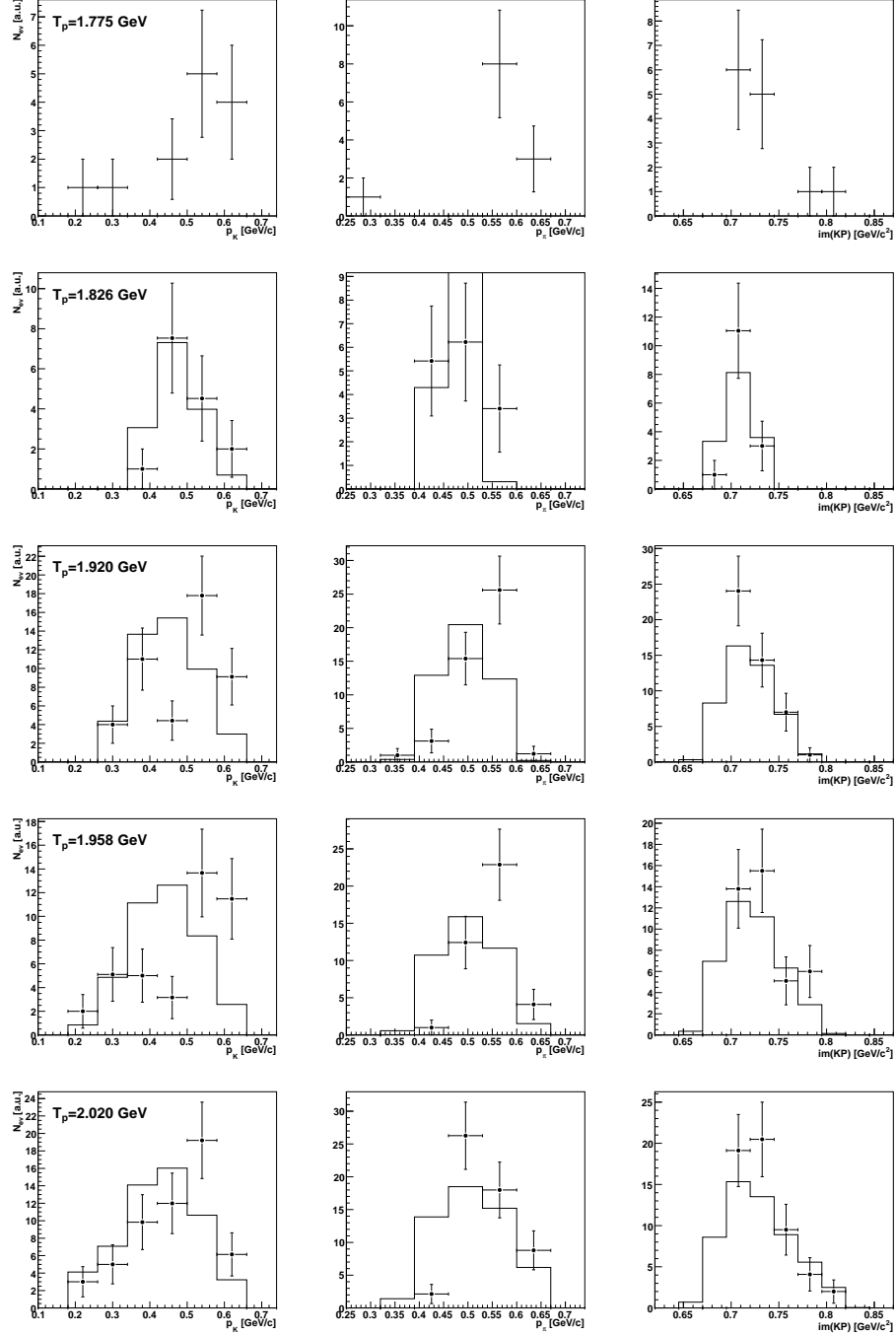


Figure 4.6: Experimental K^+ and π^+ momentum and invariant mass distributions measured at five energies and integrated over $\vartheta_K < 12^\circ$. The data collected above Σ^+ threshold compared to simulations.

T_p GeV	$N_{\text{ev}}^{\text{tot}}$	$N_{\text{ev}}^{\text{final}}$	ε_{S_o}
1.826	15.0	15.1 ± 3.9	0.18
1.920	46.4	38.6 ± 7.4	0.11
1.958	40.4	32.8 ± 6.9	0.12
2.020	55.2	47.3 ± 7.9	0.09

Table 4.6: Numbers of $K^+\pi^+$ events before $N_{\text{ev}}^{\text{tot}}$ and after $N_{\text{ev}}^{\text{final}}$ background subtraction and efficiency correction. ε_{S_o} is the integral inefficiency of the $K^+\pi^+$ analysis due to the detection of particles in the same counter.

and π^+ are detected in the same counters (for details see Sec 3.3.3). Due to the relatively small excess energies where the measurements have been performed, the numbers of such events is significant. Simulations have been used to correct for this effect in the final K^+ and π^+ momentum spectra (see Fig. 4.5b). The K^+ and π^+ momentum and invariant mass spectra, corrected for the detector efficiencies and with background subtracted, are shown in Fig. 4.6. Experimental data and simulations agree within the error bars. The analysis inefficiency as well as the extracted numbers of events are presented in Table 4.6.

4.5 Extracted total cross sections

At all the energies the total cross sections extracted from the K^+p and $K^+\pi^+$ correlation analysis are consistent with the inclusive double differential cross sections (See Sec. 4.2). The values are presented in Table 4.7.

The Λ total cross sections are in a good agreement with the experimental data of other experiments. A sophisticated model has been constructed for the extraction of the total cross section (see Sec. 4.1). The input parameters of the model are not published and therefore not widely available. The model dependence leads to the large systematic error of the total cross section. Comparison of the extracted total cross section with the parametrisation from Ref. [31] is presented in Fig. 4.7.

The Σ^0 total cross sections, except data point at 1.826 GeV, are in agreement with the experimental data of other experiments (see Fig. 4.7). Due to the interplay of the acceptances, the technical problem discussed in Sec. 2.4 would not influence the Λ total cross section but could change Σ^0 total cross section significantly. The value of the Σ^0 total cross section at this energy, as well as the differential observables, might be better extracted from a study of the experimental data collected without the use of the delayed veto.

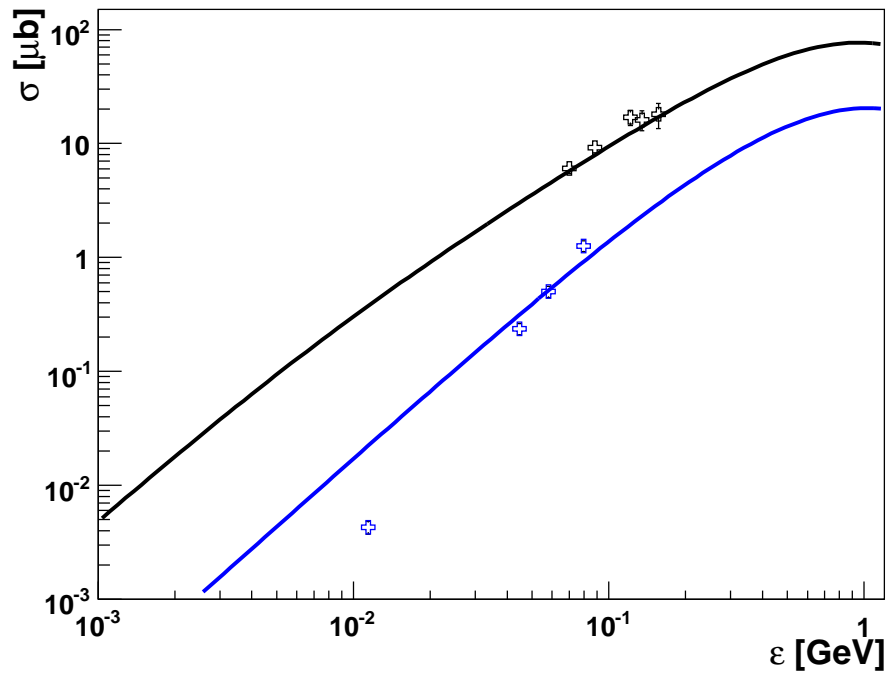


Figure 4.7: The Λ and Σ^0 total cross sections from this work as a function of excess energy in comparison with the parametrisation from Ref. [31].

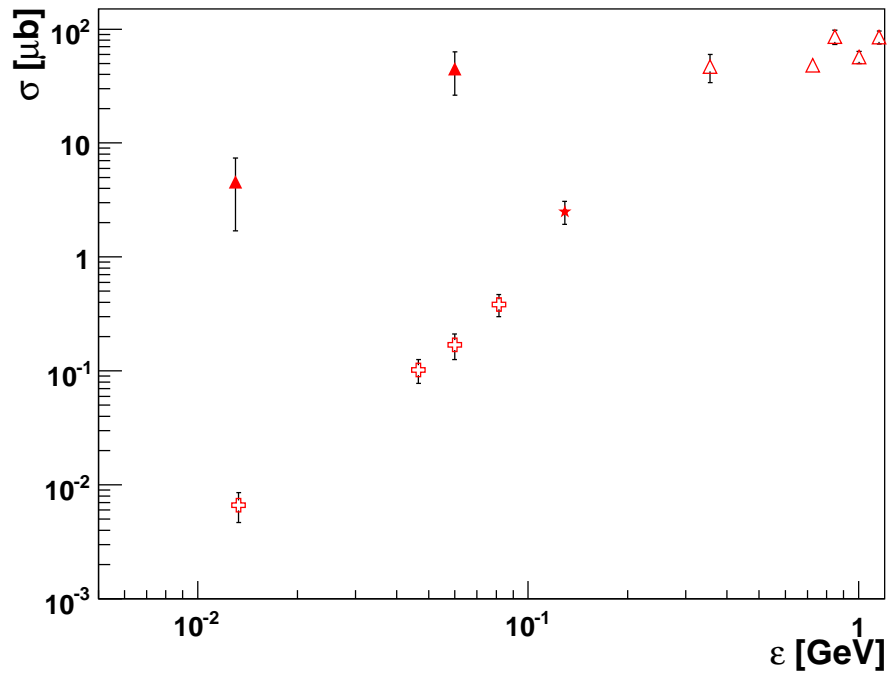


Figure 4.8: The $pp \rightarrow K^+n\Sigma^+$ total cross section as a function of excess energy. The data on the Σ^+ total cross section from this work are shown by open crosses. The data points from Refs. [48, 23] and Ref. [28] are shown by triangles and star, respectively.

Hyperon	T_p GeV	ε MeV	σ μb	$\Delta_{\text{sys}}^{\text{Model}}$ %	$\Delta_{\text{sys}}^{\text{Exp}}$ %	Δ_{stat} %	Δ_{syst} %
Λ	1.775	70 ± 1	6.1	15	9	2	18
	1.826	88 ± 1	9.2	15	9	1	18
	1.920	122 ± 1	16.9	20	9	1	21
	1.958	135 ± 1	16.1	20	9	2	21
	2.020	157 ± 1	18.0	30	9	2	31
Σ^0	1.826	11 ± 1	0.004	10	9	8	14
	1.920	45 ± 1	0.238	10	9	5	14
	1.958	58 ± 1	0.512	10	9	5	14
	2.020	80 ± 1	1.296	10	9	5	14
Σ^+	1.826	13 ± 1	0.007	10	9	26	14
	1.920	47 ± 1	0.102	10	9	19	14
	1.958	60 ± 1	0.169	10	9	21	14
	2.020	82 ± 1	0.383	10	9	17	14

Table 4.7: Total cross sections for hyperon production measured in this experiment.

The world data on the total cross section for the $pp \rightarrow K^+n\Sigma^+$ reaction are shown in Fig. 4.8. The total cross section for the Σ^+ production, determined at four energies by detecting the K^+ and the π^+ from the Σ^+ hyperon decay, are presented in Fig. 4.8 by open crosses. The values of the total cross sections measured at 1.826 and 1.958 GeV are two orders of magnitude smaller than those reported in Ref. [48] at the same energies measured using a neutron detector. The Σ^+ total cross section is systematically lower than the Σ^0 total cross section measured at the same energy (see Tab. 4.7). The ratio of Σ^+ total cross sections, determined in this work, to the Σ^0 cross sections extracted, for the same excess energy, from the parametrisation of the world data from Ref. [31] stays constant 0.3 ± 0.1 over the whole excess energy range.

Comparisons of the Σ^+ total cross section to the predictions of different theoretical models are presented in Fig. 4.9. The resulting total cross sections follow phase space normalised to one of the points. The earlier ANKE experimental point [28] lies about 3σ above this energy dependence. In order to check the reasons for this, a reanalysis of the experimental data using time calibration technique that was applied in the current experiment would have to be done.

The Σ^+ total cross sections measured at ANKE do not follow any of the theoretical lines in the Fig. 4.9. Thus, the role of the $\Delta(1620)$ resonance [49],

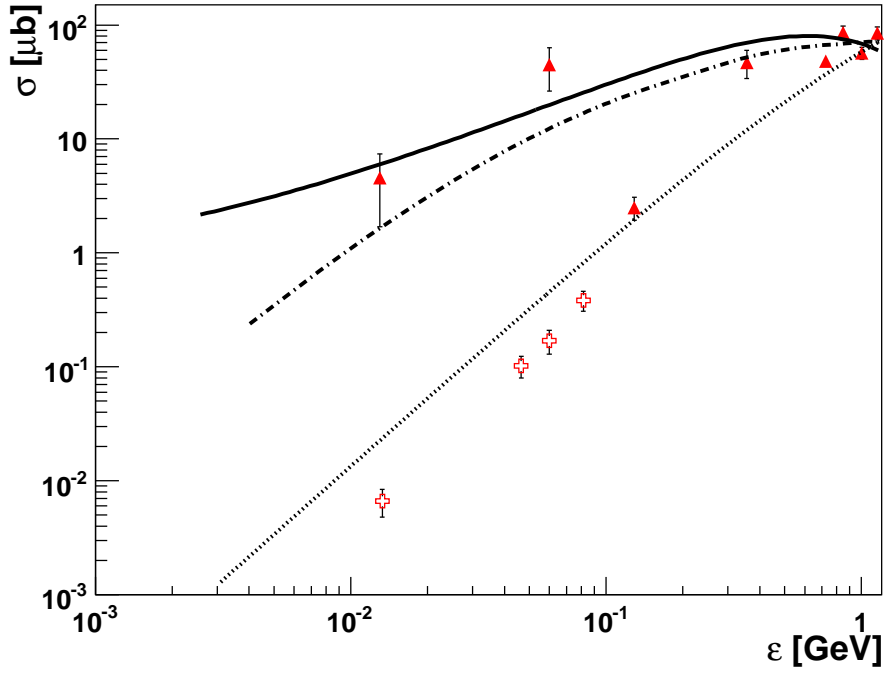


Figure 4.9: The Σ^+ total cross sections as a function of excess energy. The data on the Σ^+ total cross section from this work (open crosses), from Refs. [48, 23] (red triangles) and from Ref. [28] (star). The dotted line is the parametrisation for the three-body $K^+n\Sigma^+$ phase space with constant matrix element normalised to the new data ($M = 0.18 * 10^7$). The solid line is the parametrisation for the three-body phase space with a strong $n\Sigma^+$ FSI and energy dependent matrix element from Ref. [50]. The dashed-dotted line represents the numerical calculations from Ref. [49].

which was used to describe the surprisingly high values of the cross sections from Ref. [48], must have been grossly overestimated. There is also no indication for the strong attractive $n\Sigma^+$ FSI suggested in Ref. [50].

The K^+ inclusive and K^+p missing mass spectra measured at 1.826 and 1.958 GeV are compared in Fig. 4.10 to simulations where the Σ^+ contribution has been normalised to the total cross sections from Ref. [48]. The ANKE experimental data are overestimated by more than an orders of magnitude!

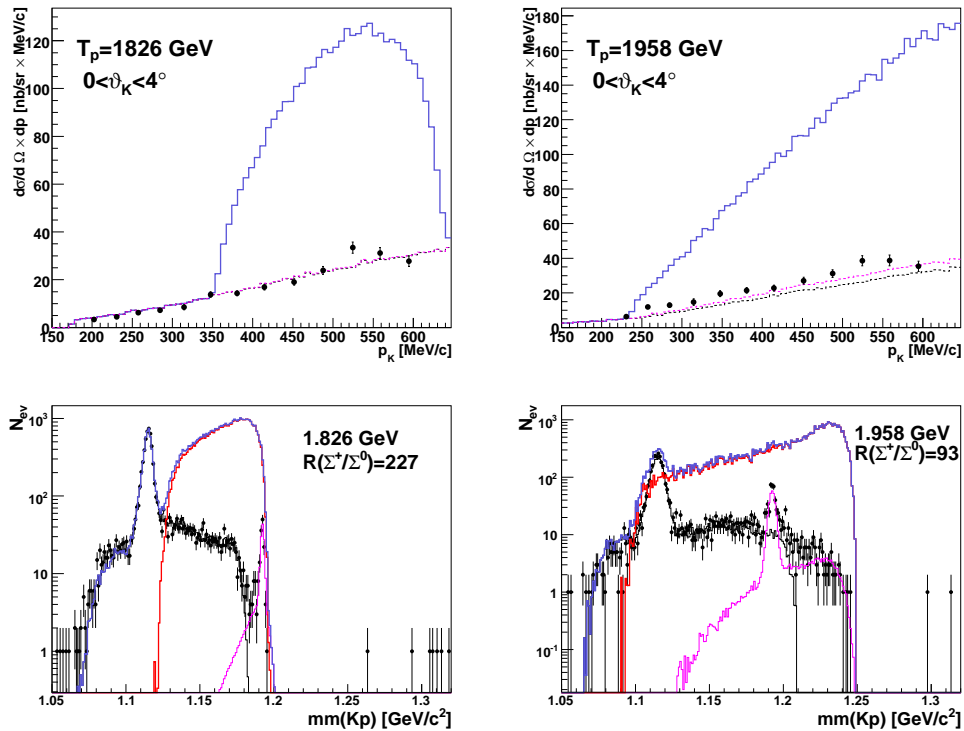


Figure 4.10: The K^+ double differential cross sections (upper panels) integrated over the $\vartheta < 4^\circ$ and K^+p missing mass spectra integrated over $\vartheta_K < 12^\circ$ and $\vartheta_p < 8^\circ$ measured in Fd at 1.826 and 1.958 GeV compared with simulations where the Σ^+ contribution has been normalised to the total cross sections from Ref. [48]. Individual contributions from the Λ , Σ^0 , Σ^+ and sum of all the channels are shown by the black, magenta, red and blue lines, respectively.

The excess energies for the various channels are calculated using the nominal beam momentum values. Uncertainties in the excess energies of the order of 1 MeV were obtained by analysing the Schottky spectra for selected runs

(see Sec. 3.5.2). Thus, the difference between the world data on the Σ^0 total cross sections and current result at 1.826 GeV cannot be due to a mistake in the beam momentum calibration.

The K^+p correlation data collected at 1.775 and 1.826 GeV could be used to extract differential observables for the $pp \rightarrow K^+p\Lambda$ and $pp \rightarrow K^+p\Sigma^0$ reactions.

Chapter 5

Conclusions

The results of the experiment presented in the thesis contribute to the knowledge about three lightest hyperon production channels in the close-to-threshold region.

The total cross section of the $pp \rightarrow K^+p\Lambda$ and $pp \rightarrow K^+p\Sigma^0$ reactions has been determined using K^+p correlation spectra. The Λ and Σ^0 total cross sections reconstructed using ANKE are in agreement with the world data, except for $\sigma(\Sigma^0)$ at 1.826 GeV, which deviates significantly from the results of other experiments [16, 26] because of technical problems during data taking.

The total cross section of the $pp \rightarrow K^+n\Sigma^+$ reaction has been determined using $K^+\pi^+$ coincidences since, below the $K^+n\Lambda\pi^0$ threshold, there is no other source of such correlations. The Σ^+ total production cross sections extracted at 1.826 and 1.958 GeV are factors of one hundred smaller than the values reported in Ref. [48]. The total cross section for Σ^+ channel, measured in the experiment described in the thesis, follow a phase space behaviour.

The total cross sections extracted at all the energies were cross checked using inclusive K^+ double differential cross sections. The measured K^+ differential spectra are in agreement with model calculations normalised to the total cross sections extracted from the experimental data.

Further investigations of light hyperon production is possible using differential observables, which can be extracted from the presented data.

Chapter 6

Outlook

Up to now very little is known about the differential observables in the $pp \rightarrow K^+p\Lambda$ and $pp \rightarrow K^+p\Sigma^0$ reactions. It is not clear if the strongly anisotropic angular spectra, measured with the COSY-TOF detector and presented in a form of PhD theses, will ever be published (see Sec. A). However, the effects of these high partial waves were not included in the analysis in Ref. [6] which led to the discussion about role of different resonances in Λ production. The parameters of all the possible hyperon-nucleon final state interactions ($p\Lambda$ and $N\Sigma$) are not yet fixed by the experimental data. However, they can serve as an important test of the $SU(3)$ symmetry [4] and have a significant influence on the development of hypernuclear physics. The experimental data analysed within this thesis can be used to attack these questions.

The present data can be used for the extraction of differential observables for the Λ and Σ^0 reaction channels. Data on the K^+p correlations collected at 1.775 and 1.826 GeV without delayed veto can be used for the evaluation of Λ differential observables, including angular spectra. Question about the Λ polarisation can also be addressed.

Different projections of the Dalitz plots of the $pp \rightarrow K^+p\Sigma^0$ reaction can be studied, searching for the influence of various resonances and final state interaction, using the delayed veto data collected and already analysed within this thesis. There is no other experimental facility which can perform such investigation except ANKE.

The contradiction between the two D_{NN} measurements, performed by DISTO [39] and COSY-TOF [42], can only be resolved by a third experiment. The D_{NN} measurements can give direct access to the production mechanism of the $pp \rightarrow K^+p\Lambda$ reaction. Very few polarised observable have been published up to now, but additional theoretical investigation is needed to select the important ones to study.

Data on hyperon production in proton-neutron collisions close to threshold simply do not exist. Thus, any measurements with a neutron target will have a big influence on the theoretical models.

Appendix A

Summary of measurements at different experimental facilities

In this Appendix the parameters of the angular spectra measured with COSY-TOF spectrometer and presented mostly in a form of PhD theses are collected [27, 33, 6, 79, 34, 35, 36, 37, 38, 80]. For the phenomenological models included in the analysis of the ANKE data, only the proton angular distributions have been used, though the angular spectra of other particles also suggest clear anisotropy. However, the $d\sigma/d\Omega(\vartheta)$ measured by TOF for a given particle was integrated over the angular and momentum distributions of all the other particles. Thus, it is not an independent variable that can be used for the model since, for example, the implementation of angular spectra of the proton into the model slightly changes the angular spectra of the K^+ and Λ within ANKE restricted angular acceptance.

Angular spectra measured with the COSY-TOF spectrometer at 2.75 GeV/ c are compared to their parametrisation [33] in Fig. A.1. The energy dependence of the proton parameters of angular spectra is presented in Fig. A.2. It is hard to estimate the errors of these parameters since there is currently

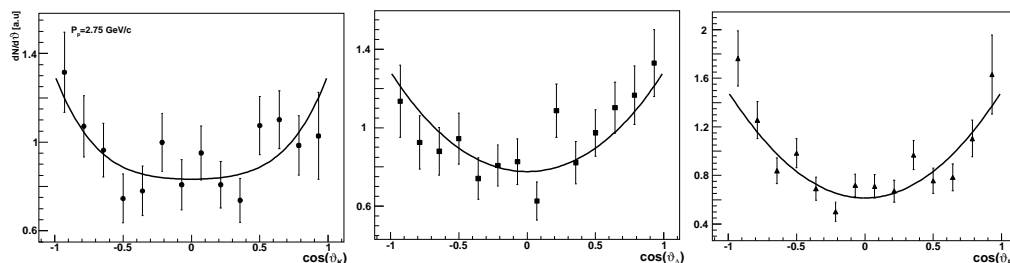


Figure A.1: The angular spectra measured with COSY-TOF spectrometer at 2.75 GeV/ c [33].

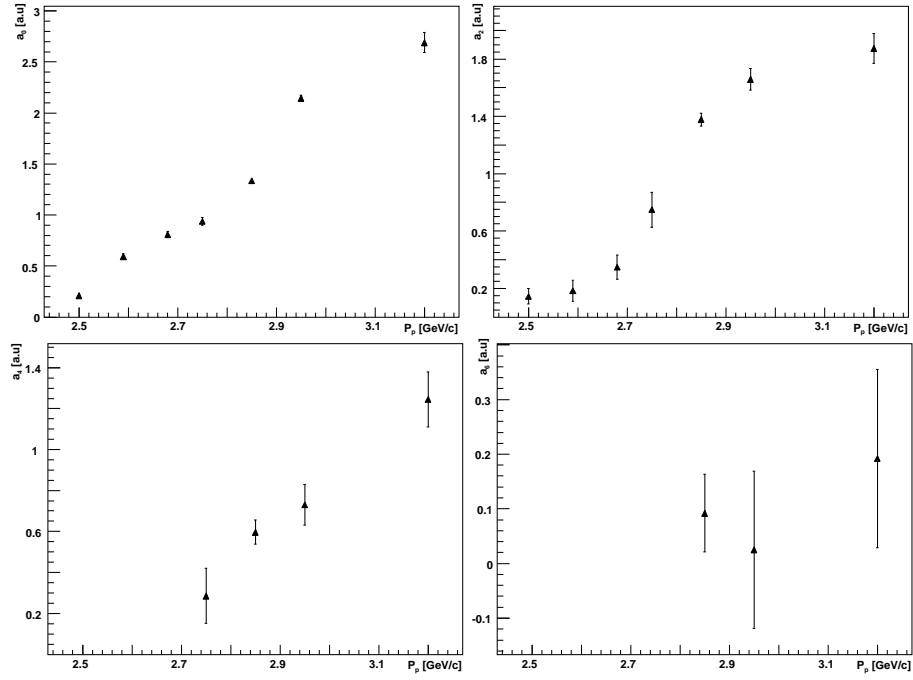


Figure A.2: Energy dependence of the parameters of the partial wave analysis for the proton angular spectra measured with the COSY-TOF spectrometer.

no dynamical model that predicts the form of the energy dependence of the angular spectra. The linear approximation used in our analysis is just a naive approach to the currently available data.

particle	a_0	a_2	a_2/a_0
K^+	0.206 ± 0.020	0.000 ± 0.016	
Λ	0.211 ± 0.020	0.064 ± 0.053	0.30 ± 0.25
p	0.207 ± 0.021	0.144 ± 0.053	0.70 ± 0.26

Table A.1: Partial wave analysis of the differential angular distributions in CM system for the $pp \rightarrow K^+p\Lambda$ reaction at 2.50 GeV/c [33](page 85).

particle	a_0	a_2	a_2/a_0
K^+	0.636 ± 0.027	0.417 ± 0.075	0.66 ± 0.05
Λ	0.617 ± 0.022	0.175 ± 0.055	0.28 ± 0.04
p	0.594 ± 0.026	0.183 ± 0.073	0.31 ± 0.05

Table A.2: Partial wave analysis of the differential angular cross sections in CM system for the $pp \rightarrow K^+p\Lambda$ reaction at 2.59 GeV/c [79](page 74).

particle	a_0	a_2	a_2/a_0
K^+	0.813 ± 0.030	0.413 ± 0.086	0.51 ± 0.06
Λ	0.843 ± 0.026	0.453 ± 0.066	0.54 ± 0.05
p	0.808 ± 0.031	0.348 ± 0.085	0.43 ± 0.06

Table A.3: Partial wave analysis of the differential angular cross sections in CM system for the $pp \rightarrow K^+p\Lambda$ reaction at 2.68 GeV/c [79](page 74).

particle	a_0	a_2	a_4	a_2/a_0	a_4/a_0
K^+	0.945 ± 0.036	0.282 ± 0.096	0.077 ± 0.124	0.30 ± 0.10	0.08 ± 0.13
Λ	0.941 ± 0.035	0.336 ± 0.093	0.009 ± 0.119	0.36 ± 0.10	0.01 ± 0.13
p	0.938 ± 0.039	0.749 ± 0.122	0.286 ± 0.133	0.80 ± 0.13	0.31 ± 0.14

Table A.4: Partial wave analysis of the differential angular cross sections in CM system for the $pp \rightarrow K^+p\Lambda$ reaction at 2.75 GeV/c [33](page 86).

particle	a_0	a_2	a_4	a_6
K^+	1.303 ± 0.022	0.484 ± 0.065	0.144 ± 0.079	
Λ	1.283 ± 0.018	0.941 ± 0.046	0.260 ± 0.062	0.173 ± 0.075
p	1.335 ± 0.017	1.379 ± 0.045	0.597 ± 0.059	0.092 ± 0.071

particle	a_2/a_0	a_4/a_0	a_6/a_0
K^+	0.37 ± 0.05	0.11 ± 0.06	
Λ	0.73 ± 0.04	0.20 ± 0.05	0.13 ± 0.06
p	1.03 ± 0.04	0.45 ± 0.04	0.07 ± 0.05

Table A.5: Partial wave analysis of the differential angular cross sections in CM system for the $pp \rightarrow K^+p\Lambda$ reaction at 2.85 GeV/c [34](page 85).

particle	a_0	a_2	a_4	a_6
K^+	2.201 ± 0.036	0.226 ± 0.103	0.044 ± 0.128	
p	2.183 ± 0.030	1.402 ± 0.077	0.218 ± 0.103	0.031 ± 0.125
Λ	2.144 ± 0.028	1.659 ± 0.076	0.731 ± 0.098	0.025 ± 0.144

particle	a_2/a_0	a_4/a_0	a_6/a_0
K^+	0.102 ± 0.047	0.019 ± 0.055	
Λ	0.642 ± 0.036	0.099 ± 0.047	0.014 ± 0.056
p	0.733 ± 0.037	0.341 ± 0.046	0.012 ± 0.069

Table A.6: Partial wave analysis of the differential angular cross sections in CM system for the $pp \rightarrow K^+p\Lambda$ reaction at 2.95 GeV/c [35](page 85).

particle	a_0	a_2	a_4	a_6
K^+	2.723 ± 0.047	0.182 ± 0.127	0.185 ± 0.169	
Λ	2.602 ± 0.038	1.878 ± 0.097	0.579 ± 0.129	0.355 ± 0.156
p	2.688 ± 0.098	1.875 ± 0.105	1.245 ± 0.135	0.192 ± 0.163

particle	a_2/a_0	a_4/a_0	a_6/a_0
K^+	0.067 ± 0.047	0.068 ± 0.062	
Λ	0.722 ± 0.038	0.233 ± 0.049	0.136 ± 0.059
p	0.698 ± 0.047	0.463 ± 0.053	0.071 ± 0.060

Table A.7: Partial wave analysis of the differential angular cross sections in CM system for the $pp \rightarrow K^+p\Lambda$ reaction at 3.20 GeV/c [35](page 91–92).

particle	a_0	a_2	a_4
K^0	0.414 ± 0.041	0.274 ± 0.122	0.120 ± 0.148
Σ^+	0.438 ± 0.050	0.547 ± 0.156	0.133 ± 0.163
p	0.398 ± 0.038	0.124 ± 0.096	0.013 ± 0.147

Table A.8: Partial wave analysis of the differential angular cross sections in CM system for the $pp \rightarrow K^0p\Sigma^+$ reaction at 2.95 GeV/c [36](page 91). Note, that angular distributions at 2.85 GeV/c are also presented in this thesis on page 90.

particle	a_0	a_2	a_4
K^0	0.402 ± 0.042	0.290 ± 0.118	0.143 ± 0.157
Σ^+	0.477 ± 0.053	0.690 ± 0.166	0.311 ± 0.172
p	0.462 ± 0.047	0.291 ± 0.136	0.234 ± 0.174

Table A.9: Partial wave analysis of the differential angular cross sections in CM system for the $pp \rightarrow K^0p\Sigma^+$ reaction at 3.2 GeV/c [36](page 91).

particle	a_0	a_2	a_0/a_2	σ_{tot}
	μb			nb
$\varepsilon = 75.8 \text{ MeV}$				
K^+	357.8 ± 12.9	552.0 ± 23.6	0.15 ± 0.07	7518 ± 324
p	336.6 ± 11.6	205.9 ± 22.9	0.62 ± 0.07	7182 ± 424
Λ	369.8 ± 12.4	201.3 ± 28.0	0.55 ± 0.08	7330 ± 284
$\varepsilon = 79.8 \text{ MeV}$				
K^+	428.6 ± 14.7	112.8 ± 28.1	0.26 ± 0.07	9179 ± 418
p	396.4 ± 13.0	298.4 ± 25.7	0.75 ± 0.06	8653 ± 326
Λ	447.6 ± 14.6	283.4 ± 35.0	0.63 ± 0.08	9242 ± 357
$\varepsilon = 81.8 \text{ MeV}$				
K^+	397.6 ± 11.8	42.1 ± 21.1	0.11 ± 0.05	8169 ± 282
p	348.9 ± 9.9	225.8 ± 18.9	0.65 ± 0.05	7939 ± 256
Λ	406.6 ± 11.3	215.1 ± 26.9	0.53 ± 0.07	8174 ± 277
$\varepsilon = 83.8 \text{ MeV}$				
K^+	490.4 ± 17.5	136.2 ± 32.5	0.28 ± 0.07	10240 ± 446
p	445.1 ± 15.5	307.2 ± 30.1	0.69 ± 0.07	9958 ± 393
Λ	528.5 ± 18.0	325.6 ± 41.8	0.62 ± 0.08	10400 ± 341
$\varepsilon = 84.5 \text{ MeV}$				
K^+	433.1 ± 16.0	169.2 ± 31.4	0.39 ± 0.07	8731 ± 379
p	373.7 ± 13.8	306.2 ± 27.4	0.82 ± 0.07	8811 ± 359
Λ	472.3 ± 16.6	317.1 ± 39.0	0.67 ± 0.08	9889 ± 438
$\varepsilon = 87.5 \text{ MeV}$				
K^+	418.3 ± 12.3	135.0 ± 23.5	0.33 ± 0.06	8497 ± 304
p	375.6 ± 10.8	273.7 ± 21.3	0.73 ± 0.06	8251 ± 269
Λ	456.0 ± 12.9	263.0 ± 29.6	0.58 ± 0.06	9408 ± 350
$\varepsilon = 89.9 \text{ MeV}$				
K^+	442.2 ± 14.6	109.0 ± 27.5	0.25 ± 0.06	8888 ± 109
p	396.6 ± 12.6	319.9 ± 25.6	0.81 ± 0.07	8575 ± 313
Λ	472.1 ± 14.9	306.4 ± 36.3	0.65 ± 0.08	9910 ± 400

Table A.10: Partial wave analysis of the differential angular cross sections in CM system for the $pp \rightarrow K^+p\Lambda$ reaction measured at COSY11 facility at different energies [81](page 66).

p (GeV/c)	$\sigma(pp \rightarrow K^+\Lambda p)$ (μb)	$\sigma(pp \rightarrow K^+\Sigma^0 p)$ (μb)	$\sigma(pp \rightarrow K^+\Sigma^+ n)$ (μb)	$\sigma(pp \rightarrow K^0\Sigma^+ p)$ (μb)
2.50	$2.7 \pm 0.3 \pm 0.3^\dagger$ [27, 33]			
2.59	$7.4 \pm 0.5 \pm 0.7^\dagger$ [6, 79]			
2.68	$8.6 \pm 0.6 \pm 0.9^\dagger$ [6, 79]			
2.75	$12.0 \pm 0.4 \pm 1.2^\dagger$ [27, 33]	1.0 ± 0.5 [27, 33]		
2.85	$16.5 \pm 0.4 \pm 0.8$ [34] $16.5 \pm 0.4 \pm 1.7^\dagger$ [6]	$1.6 \pm 0.3 \pm 0.1$ [34]	$12.7 \pm 2.3^*$ [37]	$7.8 \pm 1.6 \pm 2.0$ [36]
2.95	$23.9 \pm 0.8 \pm 1.0$ [35]	$4.8 \pm 0.4 \pm 0.2$ [35]	$4.2_{-1.8}^{+2.0}$ [37]	$12.7 \pm 1.3 \pm 1.0$ [36] 3.2 ± 0.6 [37]
3.059				$7.0 \pm 0.2 \pm 1.0$ [80]
3.20	$28.4 \pm 1.1 \pm 1.1$ [35]	$9.2 \pm 1.0 \pm 0.4$ [35]		$27.2 \pm 2.5 \pm 1.0$ [36] 6.7 ± 1.3 [37]

Table A.11: TOF measurements of the total cross sections for hyperon production in proton–proton collisions. † This error corresponds to the 10% luminosity uncertainty. $*$ This is the value given subsequently in the thesis of Karsch [37]. The original number quoted by Schönmeier was $\sigma(pp \rightarrow K^+\Sigma^+ n) = (11.5 \pm 2.4 \pm 1.8) \mu\text{b}$ [38].

Bibliography

- [1] L. Leprince-Ringuet and M. Lh eritier, *Compt. Rend.* **219** (1944) 618.
- [2] M. Gell-Mann, *Nuovo Cim. Supp.* **4** (1956) 848; K. Nishijima, *Prog. Theor. Phys. (Kyoto)* **13** (1955) 285.
- [3] G.D. Rochester and C.C. Butler, *Nature* 160 (1947) 855.
- [4] C.B. Dover and H. Feshbach, *Ann. Phys. (N.Y.)* 198 (1990) 321.
- [5] W. Chinowski et. al, *Phys. Rev.* 165 (1968) 1466.
- [6] S. Abd El-Samad et al., *Phys. Lett. B* 632 (2006) 27;
W. K. Eyrich, *Prog. Part. Nucl. Phys.* 50 (2003) 547.
- [7] N.K. Abrosimov et al., *Sov. Phys. JETP* 67 (11) (1988).
- [8] D. Miskowec et al., *Phys. Rev. Lett.* 72 (1994) 3650.
- [9] A. Badala et al., *Phys. Rev. Lett.* 80 (1998) 4863.
- [10] M. Debowski et al., *Z. Phys. A* 356 (1996) 313.
- [11] M. B scher et al., *Eur. Phys. J. A* 22 (2004) 301.
- [12] V. Koptev et al., *Eur. Phys. J. A* 17 (2003) 235.
- [13] W. Scheinast et al., *Phys. Rev. Lett.* 96 (2006) 072301.
- [14] X. Lopez et al., *Phys. Rev. C* 75 (2007) 011901.
- [15] R. Siebert et al., *Nucl. Phys. A* 567 (1994) 819.
- [16] S. Sewerin et al., *Phys. Rev. Lett.* 83 (1999) 682.
- [17] R.I. Louttit et al., *Phys. Rev.* 123 (1961) 1465.
- [18] A.C. Melissionos et al., *Phys. Rev.* 14 (1965) 604.

- [19] J.T. Reed et al., Phys. Rev. 168 (1968) 1495.
- [20] W.J. Hogan et al., Phys. Rev. 166 (1968) 1472.
- [21] A. Gasparyan et al., Phys. Rev. C 69 (2004) 034006.
- [22] A. Sibirtsev, J. Haidenbauer, H.-W. Hammer and U.-G. Meißner, Eur. Phys. J. A 32 (2007) 229, FZJ-IKP(TH)-2007-07.
- [23] A. Baldino, V. Flaminio, W.G. Moorhead and D.R.O. Morison, Total Cross Sections of High Energy Particles, Vol. 12 of Landolt-Börnstein, Numerical Data and Function Relationships in Science and Technology, edited by H. Schopper (Springer-Verlag, Berlin, 1988).
- [24] W. Fickinger et al., Phys. Rev. 125 (1962) 2082.
- [25] J.T. Balewski et al., Phys. Lett. B 388 (1996) 859.
- [26] P. Kowina et al., Eur. Phys. J. A. 22 (2004) 293.
- [27] R. Bilger *et al.*, Phys. Lett. B **420** (1998) 217.
- [28] Yu. Valdau et al., Phys. Lett. B 652 (2007) 245.
- [29] A. Sibirtsev, J. Haidenbauer, H.-W. Hammer and S. Krewald, Eur. Phys. J. A 27 (2006) 269.
- [30] G. Alexander et al., Phys. Rev. 173 (1968) 1452.
- [31] A. Sibirtsev, J. Haidenbauer, H.-W. Hammer and U.-G. Meißner, Eur. Phys. J. A 29 (2006) 363.
- [32] M. Abdel-Bary et al., COSY Proposal #178, 2007; available from: http://www.fz-juelich.de/ikp/publications/List_of_all_COSY-Proposals.shtml.
- [33] A. Metzger, PhD thesis, University of Erlangen–Nürnberg (1998).
- [34] M. Fritsch, PhD thesis, University of Erlangen–Nürnberg (2002).
- [35] W. Schroeder, PhD thesis, University of Erlangen–Nürnberg (2003).
- [36] M. Wagner, PhD thesis, University of Erlangen–Nürnberg (2002).
- [37] L. Karsch, PhD thesis, University of Dresden (2005).
- [38] P. Schönmeier, PhD thesis, University of Dresden (2003).

- [39] F. Balestra, Phys. Rev. Lett. 83 (1999) 1534.
- [40] F. Balestra, Nucl. Phys. B. (Proc. Suppl.) 93 (2001) 58.
- [41] J.M. Laget, Phys. Lett. B. 259 (1991) 24.
- [42] C. Pizolotto, PhD thesis, University of Erlangen–Nürnberg (2007).
- [43] A. Sibirtsev et al., nucl-th/0004022 (2000)
- [44] A. M. Gasparian et al., Phys. Lett. B 480 (2000) 273.
- [45] R. Shyam, G. Penner and U. Mosel, Phys. Rev. C 63 (2001) 022202(R).
- [46] K. Tsushima, A. Sibirtsev, A.W. Thomas , Phys. Rev. C 59 (2000) 369.
- [47] C. Amsler et al., Phys. Lett. B 667 (2008) 1.
- [48] T. Rożek et al., Phys. Lett. B 643 (2006) 251.
- [49] J.J. Xie, B.S. Zou, Phys. Lett. B 649 (2007) 405.
- [50] C. Xu, L. Xi-Guo, W. Qing-Wu, Chin. Phys. Lett. B 25 (2008) 888.
- [51] Yu. Valdau et al., COSY proposal #171 (2006);
<http://www.fz-juelich.de/ikp/anke/en/proposals.shtml>.
- [52] T. Rożek , PhD thesis, University of Silesia in Katowice (2005), Jül-4184,
ISSN 0944-2952.
- [53] M. Abdel-Bary et al., Phys. Lett. B 595 (2004) 127.
- [54] J.J. Xie, B.S. Zou, L. Bo-Chao, Chin. Phys. Lett. 22 (2005) 2215.
- [55] I. Zychor et al., Phys. Rev. Lett. 96 (2006) 0123002.
- [56] I. Zychor et al., Phys. Lett. B 660 (2008) 167.
- [57] A. Sibirtsev and W. Cassing, nucl-th/9802019v2 (1998).
- [58] R. Machleidt, K. Holinde and Ch. Elster, Phys. Rep. 149 (1987) 1.
- [59] R. Maier, Nucl. Instr. Methods A 390 (1997) 1.
- [60] S. Barsov et al., Nucl. Instr. Methods A 462 (2001) 364.
- [61] A. Khoukaz et al., Eur. Phys. J. D 5 (1999) 275.

- [62] K. Grigoryev et al., Nucl. Instr. Methods A 599 (2009) 130.
- [63] V. Koptev et al., Phys. Rev. Lett. 87 (2001) 022301.
- [64] A. Kacharava, F. Rathmann, C. Wilkin, COSY Proposal #152, 2005; nucl-ex/0511028.
- [65] S. Barsov et al., Eur. Phys. J. A 21 (2004) 521.
- [66] S. Dymov et al., Particles and Nuclei, Letters 2 (2004) 40
- [67] Y. Maeda et al., Phys. Rev. C 77 (2008) 015204.
- [68] Yu. Valdau, Forschungszentrum Jülich Annual Report 2007; http://www.fz-juelich.de/ikp/anke/en/Annual_Report_07.shtml.
- [69] N.K. Abrosimov et al., Sov. Phys. JETP 67 (11) (1988).
- [70] S.N. Dymov, Nucl. Instr. Meth. A 440 (2000) 431.
- [71] H.J. Stein et al., Rev. of Scient. Instr. 72 (2001) 2003.
- [72] M. Büscher et al., Nucl. Instr. Methods A 481 (2002) 378.
- [73] R.A. Arndt et al., Phys. Rev. C 62 (2000) 034005; solution SP05 (0-3 GeV) from <http://gwdac.phys.gwu.edu>.
- [74] H.J. Stein et al., Phys. Rev. ST-AB, 11 (2008) 052801.
- [75] NIST, The National Institute of Standards and Technology, <http://physics.nist.gov/>.
- [76] H.J. Stein, private communication.
- [77] S. Agostinelli et al., Nucl. Instr. Methods A 506 (2003) 250; <http://geant4.web.cern.ch/geant4/>.
- [78] A. Mussgiller, Forschungszentrum Jülich Annual Report 2004; http://www.fz-juelich.de/ikp/anke/en/Annual_Report_04.shtml.
- [79] D. Hesselbarth, PhD thesis, University of Bonn (2000).
- [80] M. Abdel-Bary *et al.*, Phys. Lett. B **649** 2007 252.
- [81] S. Sewerin, PhD thesis, Rheinische Friedrich-Wilhelms-Universität Bonn (2000); Jül-3733, ISSN 0944-2952.

Lebenslauf

Name: Yury Valdau
geboren am: 20.06.1980
geboren in: Sosnowy Bor (Rußland)

Anschrift: Buchenweg 29
52428 Jülich

Familienstand: verheiratet

Staatsangehörigkeit: russisch

Schulbildung:
09.1987–05.1990 Grundschule in Sosnowy Bor (Rußland)
09.1990–05.1997 Allgemeine Mittelschule N3 in Sosnowy Bor (Rußland)

Studium:
09.1997–06.2001 Bakalaureus der Physik an der Staatlichen Polytechnischen
Universität in St. Petersburg
09.2001–06.2003 Magister der Physik an der Staatlichen Polytechnischen
Universität in St. Petersburg

Berufstätigkeit:
seit 09.2003 Ausländischer Mitarbeiter am Forschungszentrum Jülich

Acknowledgements

The experiment presented in this thesis was possible only thanks to the joined effort of friends and colleagues from the ANKE collaboration. I would like to thank all of you for your help during the experiment and in daily life.

I owe my gratitude to Prof. Dr. Hans Ströher for giving me opportunity to work at the Institute für Kernphysik in Forschungszentrum Jülich and being my supervisor.

I would like to express my thanks to Dr. Vladimir Koptev for the countless discussions, permanent support and inspiration.

Many thanks to Dr. Mikhail Nekipelov and Dr. Sergey Dymov for their help in all aspects of data analysis and software handling. Special thanks to Misha, who was the first one who read through the complete thesis.

I am obliged to Prof. Dr. Colin Wilkin who always suffers translating my english to English and finds time to explain physics to lazy youngsters.

Thanks to Dr. Alexander Sibirtsev for a lot of discussions.

Special thanks to the COSY crew, for the very efficient beam preparation which allows us to get more data.

I would like to say a big thank you to my family and my parents - everything I have achieved is your achievement.

Finally, I am indebted to my wife Olga and my son Roman who inspire me every day of my life...

Erklärung

Ich versichere, dass die von mir vorgelegte Dissertation selbständig angefertigt, die benutzten Quellen und Hilfsmittel vollständig angegeben und die Stellen der Arbeit - einschließlich Tabellen, Karten und Abbildungen -, die anderen Werken im Wortlaut oder dem Sinn nach entnommen sind, in jedem Einzelfall als Entlehnung kenntlich gemacht habe; dass diese Dissertation noch keiner anderen Fakultät oder Universität zur Prüfung vorgelegen hat; dass sie - abgesehen von unten angegebenen Teilpublikationen - noch nicht veröffentlicht worden ist sowie, dass ich eine solche Veröffentlichung vor Abschluss des Promotionsverfahrens nicht vornehmen werde. Die Bestimmungen der Promotionsordnung sind mir bekannt. Die von mir vorgelegte Dissertation ist von Herrn Prof. Dr. Ströher betreut worden.

Yury Valdau